Validation of X-band radar-derived current measurements at the Sand Engine

The relation between spatial scale of wave dispersion analysis and accuracy

A. J. Weijenborg

Technische Universiteit Delft

TU Delft Delft University of Technology

Challenge the future

VALIDATION OF X-BAND RADAR-DERIVED CURRENT MEASUREMENTS AT THE SAND ENGINE

THE RELATION BETWEEN SPATIAL SCALE OF WAVE DISPERSION ANALYSIS AND ACCURACY

by

A. J. Weijenborg

in partial fulfillment of the requirements for the degree of

Master of Science
in Civil Engineering

at the Delft University of Technology,
to be defended publicly on October 27th, 2015 at 10:00 AM.

Student number:	4326970	
Thesis committee:	Prof. dr. ir. A. Reniers,	TU Delft (Chairman)
	Dr. ir. M. Tissier,	TU Delft
	Ir. R. Hoekstra,	TU Delft, Deltares
	Ir. J. Friedman,	Deltares
	Ir. C. Swinkels,	Deltares

This thesis is confidential and cannot be made public until October 31, 2016.

TU Delft Delft University of Technology

Department of Hydraulic Engineering
Faculty of CiTG, TU Delft
Stevinweg 1
Delft, The Netherlands
www.citg.tudelft.nl

Unit of Hydraulic Engineering
Deltares
Boussinesqweg 1
Delft, The Netherlands
www.deltares.nl

ABSTRACT

Monitoring of coastal hydrodynamics over a relatively large spatial extent and a long temporal period is essential to assess the impact of coastline interventions on several functions. An example of a recent coastline intervention is the Sand Engine, a pilot project for optimization of (future) coastline maintenance. This innovative pilot project is therefore subject to an intensive research and monitoring program that allows for development and validation of new measurement techniques. Continuous series of spatial hydrodynamics measured by remote sensing instruments have the potential to complement the temporally and spatially limited measurements of in-situ instruments.

In this thesis, the accuracy of hydrodynamics measured with a land-based X-band radar at the Sand Engine is examined. The mapping of the sea surface by an X-band radar results in wave dispersion patterns in the radar domain over time. This allows for the extraction of spatial maps of the hydrodynamic parameters d and $\vec{U}$ by spectral (Fourier) analysis of wave dispersion patterns on a limited spatial scale (*computational cube size*). Previous research has shown that the spatial and temporal scales of wave dispersion analysis are critical factors for the accuracy of remotely-sensed currents. The recently developed open-source XMFit algorithm (Friedman (2014)) is used to extract X-band radar currents.

It is not exactly known what X-band radar derived currents exactly represent. In addition, there is no agreement whether a radar measures Eulerian or Lagrangian currents. Therefore, the objective is to *find the relation between spatial scale of wave dispersion analysis and X-band radar current measurement accuracy at the Sand Engine* by *performing point- and spatial validation of currents obtained by analysis of wave dispersion on different spatial scales.* The Sand Engine study site was selected due to availability of both Eulerian ADCP measurements and Lagrangian drifter measurements.

The relation between measurement accuracy and computational cube size was found to be hyperbolic for both the point and spatial validation, which is connected to the hyperbolic relation between cube size and spectral resolution dk. An additional factor responsible for the low accuracy of XMFit for smaller cubes is a low number of spectral components available for fitting the linear dispersion relation to radar-derived spectral energy.

In-situ current estimates are consistently overestimated by XMFit for grid points within the first 500 m from the coastline. Non-linear wave effects cause anomalies in the image spectrum compared to the definition of a useful spectrum. These anomalies do not follow linear theory on which the method is based and therefore have a negative effect on the current estimate of XMFit.

In the point validation at two ADCP locations, XMFit current estimates were compared to pseudo-Lagrangian ADCP currents. The pseudo-Lagrangian ADCP currents are obtained by correcting Eulerian ADCP measurements for the surface Stokes drift. A direct comparison of XMFit to the Stokes drift-corrected ADCP measurements sets proves that the correlation in cross-shore direction is high. This supports that X-band radar currents are Lagrangian.

The spatial validation by drifter measurements is performed for another temporal period. The accuracy is significantly lower then during the point validation period: a significant offset in current direction between drifter and radar measurements is observed. A sensitivity analysis showed that, for this period in time, malfunctioning of the spectral filter to remove aliased spectral energy causes this offset. It was proven that no offset in direction is observed when optimal spectral filtering parameters are selected.

This research revealed that accurate radar current measurements are predominantly based on a (correctly filtered) image spectrum with high spectral resolution. It is emphasized that full confidence in the XMFit current retrieval method should be obtained first for simple cases with low complexity. Only then X-band radar currents are sufficiently understood and studies to more complex flow patterns are feasible.

CONTENTS

LIST OF FIGURES

GLOSSARY

List of symbols:

a	wave amplitude [m]
c	wave phase speed [m/s]
c_0	intrinsic phase speed [m/s]
d	local water depth[m]
dk_x	wave number resolution ($\frac{2\pi}{L_x}$) [1/m]
dk_y	wave number resolution ($\frac{2\pi}{L_y}$)[1/m]
$d\omega$	frequency resolution [1/s]
E_{lim}	minimum spectral energy threshold
f_n	Nyquist frequency $\frac{1}{2\Delta t}$, [Hz]
g	gravitational constant [m/s^2]
H	wave height [m]
k	wave number, $k = \frac{2\pi}{\lambda}$ [rad/m]
$\tilde{k}$	wave number of spectral wave components found by FFT [rad/m]
$\bar{k}$	average wave number of all waves in the computational cube [rad/m]
L_x	length of the computational cube in x-direction [m]
L_y	length of the computational cube in y-direction [m]
N_i	number of pixels per horizontal direction in computational cube[-]
N_w	number of images in computational cube[-]
Q	objective function being minimized in least squares algorithm [-]
t	moment in time [s]
T	wave period [s]
u_s	Stokes drift [m/s]
$\bar{u_s}$	mean Stokes drift [m/s]
$\vec{U_e}$	vector representing velocity of encounter estimated by depth inversion algorithm [U_x, U_y], [m/s]
U_n	component of velocity of encounter in wave propagation direction [m/s]
x	position in x-direction[m]
y	position in y-direction[m]
z	position in water column, measured from surface, positive upward [m]
α	wave phase [rad]
θ	wave propagation direction (normal to wave crest) [°]
λ	wavelength[m]
ω	radial frequency[rad/s]
$\tilde{\omega}$	radial frequency of spectral wave components found by FFT [rad/s]
$\bar{\omega}$	average wave frequency of all waves in the computational cube [rad/s]
ω_0	intrinsic radial frequency [rad/s]
ω_b	bandwidth (maximum) frequency involved in depth-inversion [rad/s]
ω_s	sampling frequency of the radar [rad/s]
Δt	time interval between two successive radar images/antenna rotation time [s]

$\Delta\omega$	Distance between spectral components and the linear dispersion relation [rad/s]
$E(x,y,t)$	averaged backscatter over a radar image grid cell of a moment in time [m^2]
$F(k_x,k_y,\omega)$	Spectral representation of the computational cube
$I(k_x,k_y,\omega)$	Power spectrum density of the radar image [$\frac{m^2}{Hz}$]

Abbreviations:

ADCP	Acoustic Doppler Current Profiler, instrument that measures the velocity profile over the depth at a single location
FFT	Fast Fourier Transformation, a technique to retrieve spectral representation of an image (series) that is the superposition of waves
HF	High-Frequency radar band, covering the frequency band between 3 and 30 MHz
LS	Least Squares, a fitting method that minimizes the sum of squared differences between a set of points and a formula
R	Correlation coefficient, the covariance of two variables divided by the product of their standard deviations
RMSE	Root Mean Square Error, the root of the mean of the squared differences between individual measurements from two datasets
UTC	Coordinated Universal Time

Definitions:

ADCP-bin	horizontal slice of the water column with thickness Δz for which an ADCP measurement at level z is valid
Capillary waves	centimeter scale waves at the sea surface, whose dynamics are dominated by surface tension
Computational cube	a box limiting the area of radar images used in spectral analysis.
Depth-inversion	fitting a form of the linear dispersion relation to the spectral representation of the imaged sea surface over time in $k-\omega$ space
Wave dispersion	the dependence of phase velocity on frequency or wavelength
Doppler shift	the change of wave frequency due to an ambient current
Ocean surface gravity wave	wave with a wavelength of 1-10 m, whose dynamics are dominated by gravity
Power of image spectrum:	distribution of the spectral energy over the frequencies
Pseudo-Lagrangian:	the combination of Eulerian ADCP measurement with Lagrangian Stokes drift velocity contribution
Sea clutter	backscatter due to echo at the sea surface
Spatial resolution	the spatial extent Δx,Δy of a pixel in the radar image
Stokes drift	residual wave motion in wave propagation direction over a single wave period
Temporal resolution	time between two successive radar images
Time stack	a series of raw radar images of the sea surface in time
X-band radar	radar using the microwave band of the electromagnetic spectrum [8-12 GHz]

PREFACE

This report is a result of my graduation work that has been conducted from November 2014 - October 2015 at Deltares. This thesis is the work with which I finish my MSc. Civil Engineering study at the Delft University of Technology, which I started in September 2013. This topic was an excellent combination of challenging theory on Ocean Waves and Fast Fourier Transforms and my particular interest in modeling. For me it was also very challenging to narrow the broad and relatively unexplored topic down to my own little piece of interest.

I want to thank Deltares for providing me the opportunity and the resources to successfully finish this thesis work. I would like to acknowledge my committee for their support and valuable advices during the thesis work: prof. Ad Reniers, Marion Tissier, Roderik Hoekstra, Cilia Swinkels and Josh Friedman. Thank you for the valuable advices during the meetings. Your guidance throughout the process was very valuable for me to complete the thesis. In particular I want to thank Max Radermacher for the provision of the in-situ data and his help with the processing thereof. I would also like to thank Christiaan Tenthof-van Noorden for the co-operation during the thesis. Our coffee meetings about our shared topic brought me useful insights to better understand depth-inversion. Next, I want to thank my fellow students at Deltares. Thanks for all the nice moments and fun we had during the coffee breaks and the lunch. You have been a good support to relax during the long working days.

Furthermore I want to thank my family and my flat mates, since they keep supporting me under all circumstances.

A. J. Weijenborg
Delft, October 2015

1

INTRODUCTION

Shaping the boundary between the sea and the land is the main objective in Coastal Engineering projects. The appearance of the coastline can have various forms, for example sea dikes, a sandy beach or a breakwater protecting a port from wave agitation. The coastal zone is also an attractive location for housing, recreation and industrial functions, which all demand a certain quality and appearance of the coastline. Most often, this is associated with interventions in the coastal zone. Insight in coastal processes is essential to assess their feasibility and effectiveness. The monitoring of coastal hydrodynamics is therefore a useful method to assess the impact of coastline interventions on several functions.

The Sand Engine (Stive et al. (2013)) is an example of a recent coastline intervention (2011) along the south-western Dutch coast. The Sand Engine is a mega-nourishment at the Delfland coast (figure 1.1). This part of the Dutch coastline did not met the enhanced safety requirements during the quality examination in 2006 and therefore became part of the flood protection program of Rijkswaterstaat. The Sand Engine is a pilot to gain experience with a new nourishment approach in which the volume of the nourishment is scaled up drastically. The main idea in the design is that the nourishment will serve as an engine of sand: the surplus of sediment should be redistributed along the coast by natural forcing in the coming 20 years. This should avoid expensive recurrent maintenance nourishments. The pilot project aims to combine inland long-term safety from flooding with additional space for nature and recreational functions. Monitoring of the coastal hydrodynamics is crucial to assess the impact of this innovative project on the requirements for the large variety of coastal functions it was meant for. Therefore, the Sand Engine is subject to an extensive monitoring campaign.

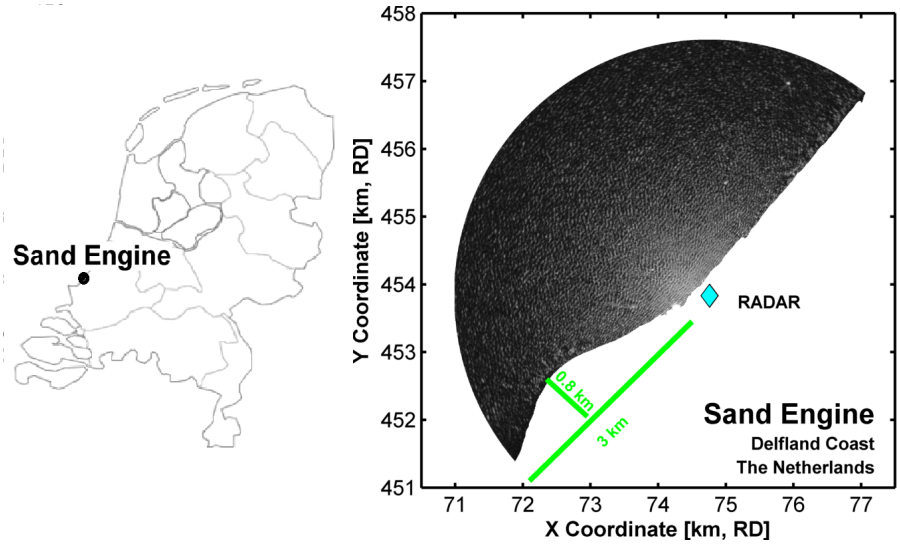

Figure 1.1: Sand Engine: a large scale nourishment along the Delfland coast

The response of coastal hydrodynamics to the construction of the large-scale nourishment is expected to be rather complex, since the Sand Engine nourishment is located in the near-shore area. The coastal processes in a near-shore environment cover a wide range of spatial scales and temporal variation (Wengrove et al. (2013)). In general, monitoring of coastal hydrodynamics heavily depends on measurements from instruments that are deployed in-situ. Examples are wave buoys, pressure sensors and echo sounding from vessels to measure bathymetry. Current measurements are commonly retrieved from drifters, fixed ADCP or vessel surveys. These in-situ instruments require installation, retrieval and replacement to enable data transfer and maintenance. Relatively high costs for the deployment of the instruments often limit the temporal extent of the measurements. Moreover, these techniques suffer from a limited spatial coverage and often do not measure at the location where data is required. This results in data that requires interpolation or extrapolation in time or space to be valuable for the intended application.

Remote sensing techniques have the ability to overcome the limitations associated with in-situ measurement instruments. Remote-sensing techniques have the advantage to be placed outside the severe oceanic environment, which avoids retrieval and maintenance issues. However, the main advantage is the ability to continuously measure hydrodynamics for a spatial area. This makes this data potentially highly valuable in coastal engineering projects. The use of remotely sensed data in these projects, however, is quite novel. Two remote sensing measurement instruments (Argus, X-band radar) are integrated in the monitoring campaign of the Sand Engine (Wengrove et al. (2013)). The expected complex hydrodynamics and a wide range of available in-situ measurements thereof provide excellent conditions for validation of remotely-sensed measurements. In this thesis work, the focus is on hydrodynamic estimates from the X-band radar at Kijkduin (figure 1.1).

The mapping of the sea surface by an X-band radar (left panel figure 1.2) allows for the extraction of near shore hydrodynamic parameters d and $\vec{U}$ from wave dispersion patterns visible in a series of radar images. An example of a current map is shown in the right panel of figure 1.2. However, to extract the hydrodynamic parameters d and $\vec{U}$, an algorithm is required. Local hydrodynamics derived from X-band radar images are validated for a limited number of algorithms, however the measurement quality is still not undisputed. The X-band radar at Kijkduin is equipped with SeaDarQ software, since tests have shown its applicability along the Dutch coast (Swinkels et al. (2012)). SeaDarQ, like many similar operating algorithms, is a 'closed' commercial product. This makes these algorithms unsuitable for proper academic research on their capability to extract coastal hydrodynamics. The open-source X-Band Matlab Fitting algorithm (XMFit) was developed recently by Friedman (2014) to avoid this problem. According to his validation, XMFit proved to be superior to the SeaDarQ algorithm at the Sand Engine, regarding both depth- and current estimates. However, the conclusions for the current estimates were based on direct comparison with in-situ current data for a single point and a short period in time. Additional investigation into XMFit current extraction capabilities is thus required, both over time and in space. Additional validation helps judging the usability of measured current fields by a radar (figure 1.2).

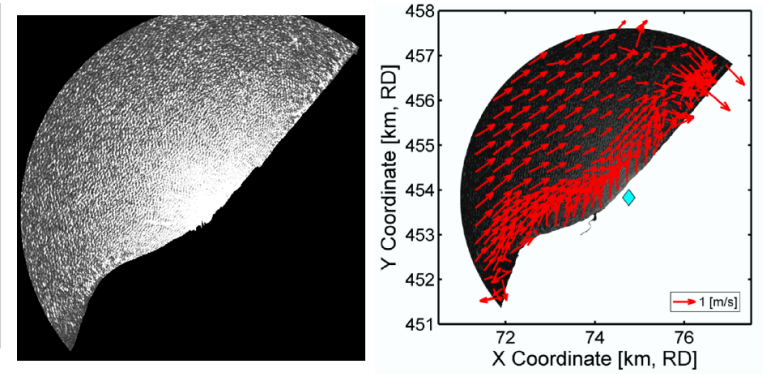

Figure 1.2: Example of radar image of the sea surface and a resolved current field

Therefore, in this thesis the focus is on the validation of X-band radar current measurements, both in time and space. Previous research (Gangeskar (2002);Piotrowski and Dugan (2002)) has shown that the spatial and temporal scale of wave dispersion analysis are critical factors for the accuracy of remotely-sensed currents. Spatial scales of 1000 x 1000 m and a temporal period of 1.5 minutes are commonly used to study flows (Swinkels et al. (2012)). However, the spatial scale is subject to a contradictory requirement: it needs to be both as small as possible and as large as possible at the same time. Selection of the appropriate spatial scale is finding a balance. More in-depth knowledge regarding the relation between the spatial scale and the measurement accuracy is required to support the choice of the optimum spatial scale.

In-situ current measurements that represent the same current as the radar measurement are required for validation. However, this is a problem for radar currents: the definition of accepted "ground-truth" measurements for radar-derived currents is under debate: there is no agreement in literature whether radar current measurements are Eulerian or Lagrangian. Nowadays, radar-derived currents are validated by direct comparison with in-situ data from either Eulerian current profilers or Lagrangian drifters (Ohlmann et al. (2007)). A unique opportunity for X-band radar current validation with both methods arises due to a rich variety of in-situ measurements around the Sand Engine that is available for October 2014. These measurements were made in the context of the Mega Perturbation EXperiment (MegaPEX). MegaPEX is a six weeks field experiment around the Sand Motor. The understanding of the feedback between coastal processes and hydrodynamics, morphology, aeolian transport, dune formation, hydrology and ecology is focus of this large-scale research experiment. MegaPEX resulted in a rich variety of current measurements, from which Eulerian measurements by multiple Acoustic Doppler Current Profilers (ADCP) allow for a time series validation at single locations. In addition, Lagrangian current measurements from multiple drifters are available, which allow for validation of radar current measurements in space.

The aim of this thesis is to *find the relation between spatial scale of wave dispersion analysis and X-band radar current measurement accuracy at the Sand Engine* by *performing point- and spatial validation of currents obtained by analysis of wave dispersion on different spatial scales.*

The following questions are guiding towards the achievement of this goal:

- How do accuracy and spatial scale relate for a single point and a fixed temporal scale?
- How does this relation differ for radar currents along drifter trajectories in the radar domain?

The Sand Engine is located near the outlet of the river Rhine. Exclusively during flood, a fresh-water plume passes trough the radar footprint. This possibly has an impact on the accuracy of radar-derived currents. Therefore, ebb and flood situations are distinguished.

This thesis is outlined as follows. In the next chapter, the necessary background regarding radar imaging and the wave dispersion analysis is provided, followed by a discussion about the function of the spatial scale of this analysis in current retrieval. The chapter is concluded with a section on radar current validation studies and relevant accuracies. Chapter 3 opens with a description of relevant radar parameters and continues with a brief overview of XMFit and the choice for the least-squares fitting method. The validation of radar currents with point (Eulerian) ADCP measurements follows in chapter 4. An adjusted version of the commonly applied point-validation method is presented, followed by the results of the comparison. A spatial validation of radar currents with (Lagrangian) drifter measurements is the subject of chapter 5. First, the dynamic grid approach and drifter data are described. Once more, the chapter concludes with a description of the validation results. In chapter 6, the results of both the point validation and spatial validation are discussed. Particular attention is also paid to the differences between the results for both validation periods. The discussion is followed by the conclusions (chapter 7). Finally, chapter 8 will conclude with the recommendations regarding further development and the testing of the XMFit algorithm.

2

LITERATURE REVIEW

This literature review is focusing the extraction and validation of radar currents. The current retrieval procedure from sea surface imagery is discussed in section 2.1. The influence of the spatial scale of wave dispersion is subsequently elaborated in section 2.2. This chapter concludes with a discussion on the complexity of validating radar-derived currents in section 2.3. Relevant validation studies are reviewed, for which the accuracies may function as benchmark for the accuracy of radar currents obtained in this study.

2.1. CURRENT RETRIEVAL FROM X-BAND RADAR IMAGES

X-band current measurements are based on spectral (Fourier) analysis of wave dispersion patterns in a limited area in the image series. X-band current retrieval is an optimization problem in spectral dimensions: a *depth-inversion* algorithm fits wave dispersion equations to the spectral representation of ocean surface gravity waves whose signatures are visible in the radar images of the sea surface. The wave dispersion equation has current $\vec{U}$ and local water depth d as unknowns, thus allowing for a simultaneous estimation of both parameters. This section starts with a description of the responsible imaging mechanisms to understand how the spectral components should be interpreted. It is followed by a detailed description of the current retrieval process itself.

2.1.1. X-BAND RADAR IMAGING

Current extraction from X-band radar images is accomplished by using the echo of radar waves from the sea surface, also referred to as *sea clutter*. Sea clutter is visible on radar images due to interaction between emitted radar microwaves and centimeter scale capillary waves at the sea surface. Specular reflection and Bragg scattering (Young et al. (1985)) are the two possible interactions between emitted radar waves and capillary waves. The angle of incidence with respect to the sea surface normal determines which mechanism is dominant. Marine X-band radar is characterized by a low antenna height and therefore has a large angle to the sea surface normal. Bragg scattering is the dominant mechanism for this configuration (Valenzuala (2012)). Bragg scattering is defined as the reflection of radar-transmitted microwaves by capillary waves with a wavelength half of the length of the transmitted radar wave (Paduan and Graber (1997)). The electromagnetic energy emitted by X-band radar is characterized by wavelengths of approximately 3 cm and frequencies of 8-12 GHz. Thus, centimeter scale capillary waves serve as Bragg resonating waves.

The wave dispersion equations being fit in a depth-inversion algorithm describe the dispersion of ocean surface gravity waves that have wavelengths λ of $10-100m$. However, capillary waves are responsible for radar imaging. Nevertheless, the modulation of the centimeter scale Bragg-scattering process by ocean surface gravity waves is visible in the X-band radar images. The signatures of these modulation(s) in the radar images are used to derive the spectral representation of the ocean surface gravity waves. Three effects cause the modulation of the X-band radar signal (Borge et al. (2004)).

1. Shadowing, a mechanism in which relatively high surface waves prevent energy to reach a certain part of the sea surface by blocking the microwave radar energy (fig 2.1)

2. Hydrodynamic or orbital modulation, defined as modulation of ripple energy by interaction with longer (surface) gravity waves. Hydrodynamic modulation appears as a change in backscattered power across the phase of the long wave (Thompson et al. (1991)).

3. Tilt modulation, which is modulation of energy resulting from changes of effective incidence angle along the slope of long (surface) gravity waves

Shadowing is the dominant mechanism for small incidence angles of X-band radar energy with respect to the sea surface (Seemann et al. (1997)). The angle of incidence then approximates the average slope of the ocean waves or is even smaller. Figure 2.1 shows the shadowing mechanism for a single regular sine wave. The radar antenna transmits X-band radar waves at grazing angles of incidence, shown by the solid black lines in figure 2.1. The wave height of relatively high wave crests prevents the radar waves with grazing incidence to reach certain parts of the sea surface. These areas are indicated in gray. This results in zero backscatter of radar wave energy for the shadowed part of the sea surface (lower plot). The lower plot shows a binary signal, 0 indicating zero backscatter and 1 represents detection of reflection(s) from the sea surface. The part of the sea surface that is not shadowed reflects radar energy back to the radar, resulting in a one in the lower plot. This plot shows the periodicity of the binary signal of the backscattered radar energy. Shadowed areas occur at regular intervals λ in space. This periodicity in the signal reveals the wavelength λ of ocean surface gravity waves, which is the sum of the lengths of the shadowed area and the reflecting area of the wave (lower plot figure 2.1).

Sufficient roughness of the sea surface is required to obtain a usable radar image for depth-inversion. The roughness of the sea surface is important since the shadow mask is more pronounced for steeper waves. In various studies, met-ocean limits for wind and wave conditions are suggested in relation to image quality. Examples are a minimum wind speed of 2-3 m/s (Bell et al. (2012);Swinkels et al. (2012)) and a minimum wave height of 1 m (Bell et al. (2012)). Friedman (2014) discussed met-ocean conditions in relation to depth-inversion and found good agreement of for wave heights > 1 m and wind speeds > 12 m. However, all studies mentioned here do consider a limited period in time. In addition, the quality of the radar image depends on the distance to the radar installation. The return of radar energy decreases with increasing distance to the radar. The incidence angle of the radar energy is the most important parameter that determines the usable range of the X-band radar images. This is illustrated in figure 2.2. The incidence angles of 1 ° and 10 ° form the boundaries of the better working area, for which X-band radar energy return is useful (Maa and Ha (2005)).

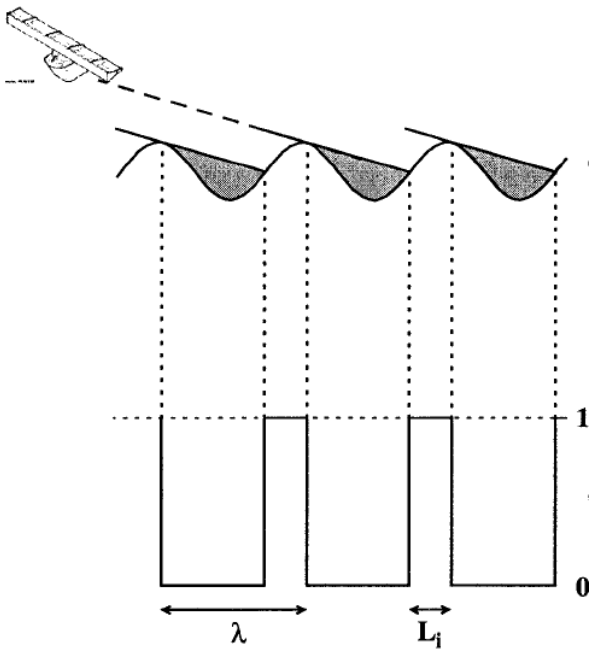

Figure 2.1: Repetitive shadow mask with wavelength λ in an X-band radar image in case of grazing incidence of the radar energy. After: Seemann et al. (1997).

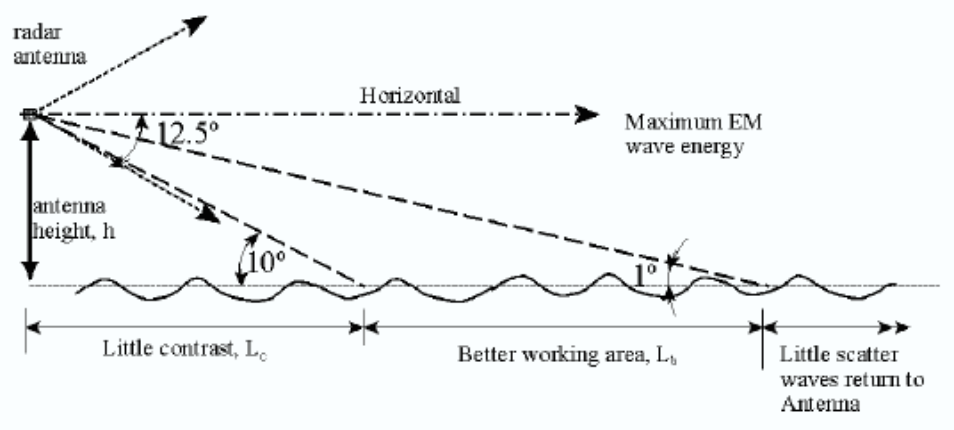

Figure 2.2: Illustration of the useful area for X-band sea surface imaging. After: Maa and Ha (2005).

The spreading of X-band radar waves usually is around 25 degrees, from which the part above the horizontal does not contribute to imaging of the sea surface. The attenuation of electromagnetic radar energy with range is usually described by an exponential function. More background regarding radar specifics can be found in Borge et al. (2004) and Young et al. (1985).

In addition, rain directly influences the imaging of sea clutter in a negative way. Ward et al. (2006) account via a loss factor for propagation loss of electromagnetic energy due to interaction with rain droplets. Moreover, electromagnetic energy above the horizontal (figure 2.2) may directly interact with rain droplets, resulting in a mixture of rain clutter and sea clutter in the radar image (Appleyard et al. (1997)). Rain thus introduces noise that is undesirable for current retrieval.

2.1.2. DEPTH-INVERSION

Depth-inversion implies the fit of a wave dispersion equation to the spectral representation of ocean gravity waves. The extraction of wavelength λ of a 1D ocean gravity wave from a shadow mask of the sea surface was illustrated in the previous section. The wavelength allows for calculation of wavenumber k. Depth-inversion requires a full 3D *image spectrum*: the spectral representation of a 2D wave field propagating in time. However, the same principle is used: the image spectrum is derived from a 2D shadow mask of the sea surface. Consider the shadow mask of a single 2D radar image as the superposition of a large number of harmonic wave components. The relation between spectral parameters k, ω and the shadow mask of the sea surface $E(x, y, t)$ may be described as follows (Holthuijsen (2009)):

$$E(x,y,t) = \sum_{i=1}^{M}\sum_{j=1}^{N}\sum_{l=1}^{P}(\underline{a_{i,j,l}}cos(\omega_i t - k_j x cos\theta_l - k_j y sin\theta_l + \underline{\alpha_{i,j,l}})) \tag{2.1}$$

$a_{i,j,l}$ represents the amplitude of an individual wave component, α the wave phase of an individual wave and θ the direction of wave propagation (normal to the wave crest of each individual component).

Fast Fourier Transformation (FFT) is a technique that converts signals from the time-space domain into the spectral domain $\vec{k}, \omega$. The basic concept is that a shadow mask image may be represented by equation 2.1. The FFT technique is used to transform the images of the sea-surface shadow mask over time into the image spectrum. A Cartesian grid is required for an FFT. Therefore polar radar images are transformed to a Cartesian grid. From this Cartesian grid, a data box (hereafter referred to as *computational cube*) is extracted from the radar images. The computational cube (right panel figure 2.3) represents a sub area of the radar image (red box in figure 2.3) for a number of N images. The dimensions of the computational cube are given by the *cube size*, which is expressed in a number of pixels N_i in X and Y-direction and the *stack size* that is expressed in the number of images N_ω. The computational cube size is the spatial scale over which wave dispersion patterns are analyzed. The computational cube is 3D Fourier Transformed to its spectral representation F(k_x, k_y, ω) (Young et al. (1985)) to enable current retrieval.

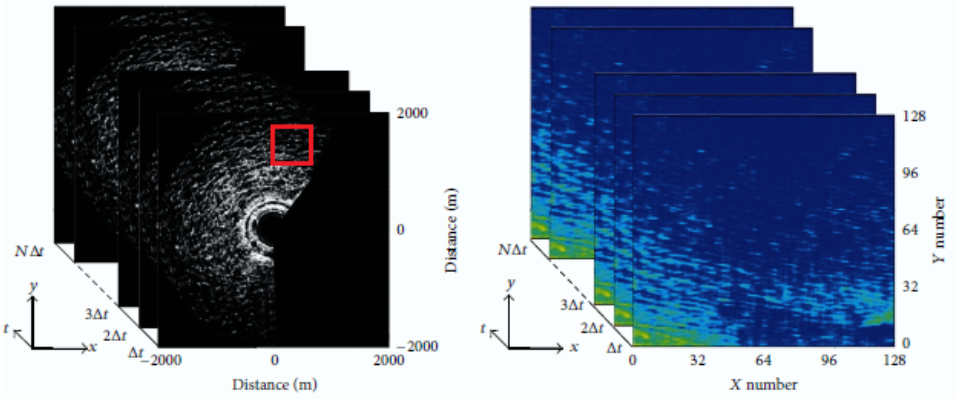

Figure 2.3: The extraction of a computational cube from a series of radar images. After: Liu et al. (2014).

It is inherent to spectral analysis that wave behavior is assumed to be homogeneous within the computational cube, both in time- and spatial dimension. In most cases this assumption holds, however in case of high horizontal current shear or a strongly varying bathymetry this may cause problems (Bell et al. (2012)). Under these conditions, there are two different wave propagating regimes present in the image series, which will introduce a spectrum in which the individual spectra of both wave propagating regimes are merged.

Next, a depth-inversion algorithm is deployed to fit wave dispersion equations with unknowns $\vec{U}$ and d to the spectral representation of the ocean waves. The expression with which dispersion of ocean surface gravity waves is described depends on the presence of a current:

- In the absence of a current, waves will follow the intrinsic linear dispersion relation

$$\omega_0 = \sqrt{g|k|tanh(|k|d)} \tag{2.2}$$

  in which k represents the wave number of the gravity wave, g the gravitational acceleration and d the local water depth. The (intrinsic) phase speed in still water c_0 is calculated with $c_0 = \frac{\omega_0}{k}$.

- Waves that experience a current will have a modified phase speed and as a result they are subject to a shift in frequency in a Eulerian measurement. This frequency shift is referred to as Doppler shift. The phase speed is determined by vectorial summation of the phase speed and the velocity of encounter.

$$\vec{c} = \vec{c_0} + \vec{U_e} \tag{2.3}$$

  $\vec{U_e}$ represents the current responsible for the Doppler shift, which is termed velocity of encounter (Senet et al. (2001)). The velocity of encounter is equal to the in-situ current in case of a uniform current over depth. The shift in wave frequency is described by including a term describing the Doppler shift in the linear dispersion relation (Holthuijsen (2009)):

$$\omega = \omega_0 + kU_n \tag{2.4}$$

  The Doppler shift is given by kU_n, in which k represents the wave number of the ocean gravity wave and U_n the velocity component in wave propagation direction.

The depth-inversion technique is limited to **linear** ocean surface gravity waves, since the linear dispersion relation is based on linear waves. The application of the linear wave theory is limited by the following inherent limitations (Holthuijsen (2009)):

1. The water body is considered as an ideal fluid, which implies an incompressible fluid with constant density
2. The water body is a continuous fluid, which means that no voids are present
3. The water particles are subject to a single external forcing

4. The wave amplitude is small with respect to local water depth ($\frac{a}{d} << 1$)

The linear dispersion relation describes a shell in spectral space (figure 2.4). The linear dispersion relation may thus also be referred to as *dispersion shell*. In case of a current, spectral data is shifted from a situation without current (intrinsic). The effect of a current on the spectral data and the linear dispersion relation is shown in figure 2.5. The figure shows a 2D slice of a 3D wave spectrum. The black solid line shows the intrinsic dispersion relationship, according to equation 2.2. A situation with a current to the right is considered. Spectral data of ocean gravity waves in absence of a current have an orange/yellow color. In case the current aligns with the wave propagation direction (positive values of k), the radial frequency ω increases by kU_n and spectral data shifts upward to the blue positions right from the ω axis. For currents opposite to the wave propagation direction, the radial frequency ω decreases and the spectral data will be shifted downward to the blue positions left from the ω axis. The Doppler-shifted dispersion relation (equation 2.4) relates k and ω in case of a current and is indicated with the gray line in figure 2.5. Note that the shape of the shell changes in case of a current: it is directly dependent on the current $\vec{U}_e$. The radar-derived current is thus derived from the Doppler shift of the spectral components in the image spectrum compared to a situation without currents.

Current retrieval from X-band radar images is therefore essentially an optimization problem (Liu et al. (2014)). By curve fitting of the Doppler-shifted linear dispersion relation to the image spectrum, the most likely values for the unknowns depth d and current $\vec{U}$ are found. The common method is to fit the dispersion shell to the full image spectrum, thus resulting in a single estimate of the most likely depth and current.

2.1.3. SPECTRAL SIGNAL PROCESSING

The depth-inversion algorithm uses the weighted least-squares principle to fit the dispersion shell to image spectra. In this context, the least squares (LS) method aims at minimizing the squared difference between the spectral coordinates of the image spectrum and the dispersion shell. This comes down to minimizing the objective function

$$Q = \sum_{\omega=0}^{\omega_M} \sum_{\tilde{k_x}=-\tilde{k_x}}^{\tilde{k_{xN}}} \sum_{\tilde{k_y}=-\tilde{k_y}}^{\tilde{k_{yN}}} (\Delta\omega)^2 I(\tilde{k_x}, \tilde{k_y}, \omega) \tag{2.5}$$

where Q is an arbitrary variable being minimized, I the spectral power that serves as weight of each data point in the fit and $\Delta\omega$ is given by

$$\Delta\omega = \tilde{\omega} - \sqrt{g|\vec{k}|tanh(|\vec{k}|d)} - k_x U_x - k_y U_y \tag{2.6}$$

In equations 2.5 and 2.6, $\tilde{\omega}$ and $\tilde{k}$ are the radial frequency and wavenumber of an individual spectral component in the image spectrum. g is the gravitational constant. The current components are subsequently determined by solving (Gangeskar (2002)):

$$\begin{bmatrix} U_x \\ U_y \end{bmatrix} = \begin{bmatrix} \sum_{i=1}^{N} Ik_{x,i}^2 & \sum_{i=1}^{N} Ik_{x,i}k_{y,i} \\ \sum_{i=1}^{N} Ik_{x,i}k_{y,i} & \sum_{i=1}^{N} Ik_{y,i}^2 \end{bmatrix}^{-1} * \begin{bmatrix} \sum_{i=1}^{N} Ik_{x,i}\Delta\omega \\ \sum_{i=1}^{N} Ik_{y,i}\Delta\omega \end{bmatrix} \tag{2.7}$$

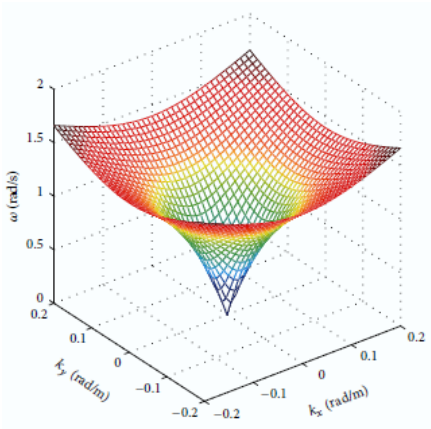

Figure 2.4: The linear dispersion relation describes a dispersion shell in spectral space. After: Liu et al. (2014).

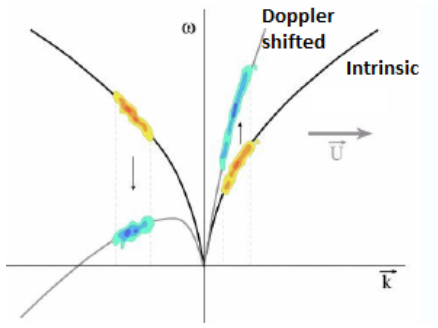

Figure 2.5: Doppler shift in the radian frequency in case of an ambient current U for a slice of a 3D image spectrum. After: Hessner and Bell (2009).

XMFit offers two solvers (non-linear *regression* and trust-reflective *optimization*) for simultaneous current and depth retrieval. Both solvers deploy a least squares algorithm that solves the current with the method described here. Friedman (2014) showed that the minor differences in mathematical approximation of U cause negligible difference in the current estimates.

The raw image spectra need to be filtered before the depth-inversion algorithm is deployed. The data points in a raw X-band image spectrum can be divided into three classes (Liu et al. (2014)):

- Spectral energy of waves that follow the fundamental linear dispersion relation (equation 2.4).
- Spectral energy of nonlinearities that are due to shadowing as a non-linear imaging process (Seemann et al. (1997)). This spectral components are also referred to as higher order wave phenomena.
- Spectral energy obtained due to the aliasing phenomenon and background noise

The spectral data following the fundamental dispersion mode are exclusively desired for curve fitting, since we do fit the fundamental linear dispersion relation to exactly these data points in the image spectrum. The other spectral components are more complex since they do not follow the linear dispersion relation and therefore will introduce errors in the current estimate. Senet et al. (2001) made significant progress by developing methods to properly include the energy of aliased and nonlinear wave components in the fit. However it is not proven that algorithms that include those components in the fit perform significantly better. Therefore, the focus is on the origin of those complex spectral components and how to remove them from the spectrum.

Spectral nonlinearities
Spectral nonlinearities occur due to non-linear imaging of the sea state by a marine radar and weak nonlinearity of the ocean waves themselves. The dominant source for spectral nonlinearities is the non-linearity of the radar imaging function, which is related to the shadowing imaging mechanism (Senet et al. (1997);Senet et al. (2001)). Figure 2.6 illustrates the result of this nonlinear imaging for two spectral wave components (F1 and F2) for a k,ω-slice of the image spectrum. The components F1 and F2 do follow the fundamental dispersion relation (equation 2.4) that is indicated by the solid line. The sum and difference peak can be found by vectorial summation or subtraction of F1 with F2 respectively. In addition, higher harmonic wave components (H1, H2) do occur to the nonlinearities $H1 = 2F1$ and $H2 = 2F2$ respectively. Higher harmonics are characterized by a low spectral energy content. Therefore a high-pass spectral energy filter with a spectral energy threshold E_{lim} is applied (Senet et al. (2001);Liu et al. (2014)).

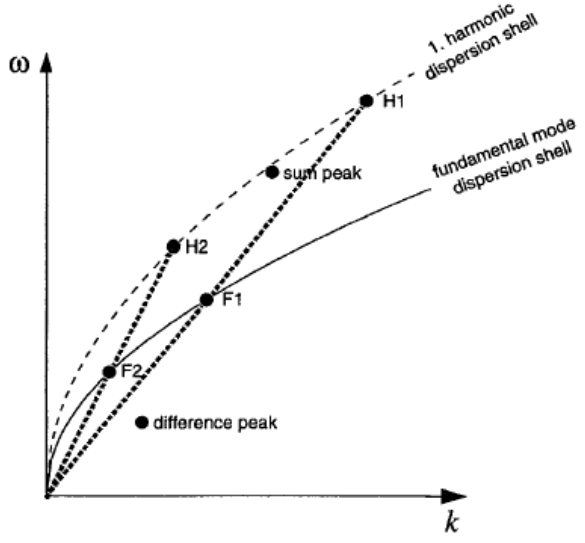

Figure 2.6: Non-linear imaging results in spectral non-linearities H1,H2, sum and difference peak that do not follow the linear dispersion relation. After: Seemann et al. (1997).

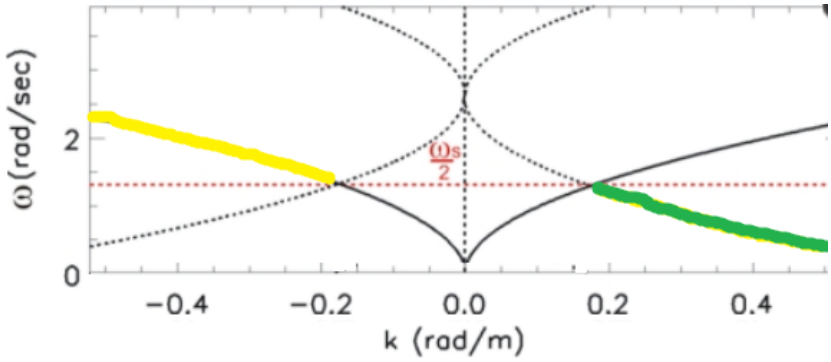

Figure 2.7: Spectral energy from frequencies exceeding the Nyquist frequency $\frac{\omega_s}{2}$ is 'folded' onto a replica of the dispersion relationship and appears as aliased energy in the spectrum. Adapted and modified after: Serafino et al. (2011).

Energy of aliased wave components

Aliasing of wave energy occurs in case of a high spatial resolution of the radar image and a low temporal resolution. Due to the relatively slow rotation time of the radar, waves may be under-sampled (Senet et al. (2001);Serafino et al. (2011)). Under-sampled means the wave is sampled less then twice each wave period and as a consequence the Nyquist frequency $f_n = \frac{1}{2\Delta t}$ is exceeded. The sampling frequency ω_s is given by

$$\omega_s = \frac{2\pi}{\Delta t} \tag{2.8}$$

in which Δt represents the antenna rotation time. In order to have the constructed wave image spectrum unaffected by aliasing, the following should hold (Serafino et al. (2011)):

$$\omega_s \leq 2\omega_b \tag{2.9}$$

in which ω_b represents the bandwidth (maximum) frequency involved in the analysis. However, if this condition is violated, energy associated with frequencies higher then the Nyquist frequency appears as energy at lower wave frequencies (Holthuijsen (2009);Serafino et al. (2011)), which is illustrated in figure 2.7. Spectral wave energy on the fundamental mode dispersion relation (solid black line) with frequencies exceeding the Nyquist frequency $\frac{\omega_s}{2}$ are shown in yellow. These points are 'folded' in the spectrum and appear as aliased spectral energy (green) on a replica of the dispersion relation (dotted line). These replicas have the same shape as the fundamental mode dispersion relation (solid black line) however they are mirrored in the red dotted line that represents the Nyquist frequency. For more details regarding the aliasing phenomenon and the effects on current estimates, see Serafino et al. (2011). Aliased dispersion shells are characterized by increasing shell width for decreasing ω (figure 2.7) and a relatively low energy content with respect to the spectral coordinates of the fundamental mode. The high-pass spectral energy filter mentioned is therefore used to filter aliased energy as well.

Spectral noise

Raw image spectra contain background noise. This may result from rain clutter, reflections from deployed measurement instruments or vessels, etc... Background noise is more prominent when spectral resolution decreases (Piotrowski and Dugan (2002)). The high-pass spectral energy filter is applied to filter noise as well, since noise in general has a relatively low spectral energy content.

2.2. THE ROLE OF SPATIAL SCALE OF WAVE DISPERSION ANALYSIS

X-band radar current estimates are directly derived from spectral (Fourier) analysis of the computational cube (data box). The computational cube is directly linked to the spectral information in the radar image: the sizes of the cube determine which area is Fourier Transformed for analysis of wave dispersion patterns.

Increasing computational cubes imply analysis over a larger spatial and temporal scales. A logical result of the larger scales is an increase in the number of spectral components. A larger number of spectral regression components increases the accuracy of a least-squares algorithm. To enable determination of the full current vector, an image spectrum with significant directional spread is required, as it generally does under natural sea states (Lund et al. (2012)). This spread is also more pronounced for larger cube sizes since an increased number of spectral components is available for regression for bigger cube sizes.

In addition, the spectral resolution is directly linked to the size of the computational cube that is Fourier Transformed. The spectral resolutions dk_x, dk_y are inversely proportional to the lengths of the sides of the analysis area (L_x, L_y) and the frequency resolution $d\omega$ is inversely proportional to the timescale corresponding to the stack size: $N\Delta t$ (Liu et al. (2014)). The spectral resolution directly influences the allocation of spectrum power to spectral coordinates (equation 2.10, Liu et al. (2014)):

$$I(k_x, k_y, \omega) = \frac{1}{L_x L_y N \Delta t} |F(k_x, k_y, \omega)|^2 \tag{2.10}$$

In this equation, $I(k_x, k_y, \omega)$ represents the power density of each point in the image spectrum, L_x and L_y the sides of the rectangular analysis area, $N\Delta t$ the time scale corresponding to the stack size, and F the Fourier transformed computational cube. Since the focus in the research is exclusively on the computational cube size, this description is continued for the cube size. The inverse relation between spectral resolution and cube size shows that for increased cube sizes, spectral resolution is higher. Theoretically, a higher spectral resolution would lead to a thinner dispersion surface, which in theory could be matched more accurately (Piotrowski and Dugan (2002)). A more accurate match of data and dispersion shell provides improved precision of the values of the unknowns $\vec{U_e}$ and d. Smaller cubes may lead to reduced precision in the positioning of the dispersion shell, simply due to a lower spectral resolution.

Gangeskar (2002) theoretically related poor spectral resolution to low accuracies of current estimates obtained with small computational cubes. Piotrowski and Dugan (2002) examined how accuracy of currents derived from airborne optical imagery depends on cube (box) size. Their study compared currents derived from airborne optical imagery with ADCP current data for three time stacks with a duration of 2 minutes. Cube sizes of 128 m, 192 m, 256 m, 384 m and 512 m were examined. The cube sizes are smaller since optical imagery has a much higher resolution then X-band images. The results show that current accuracy increases (decrease of RMSE) with increasing cube size (diamond dots left axis figure 2.8).

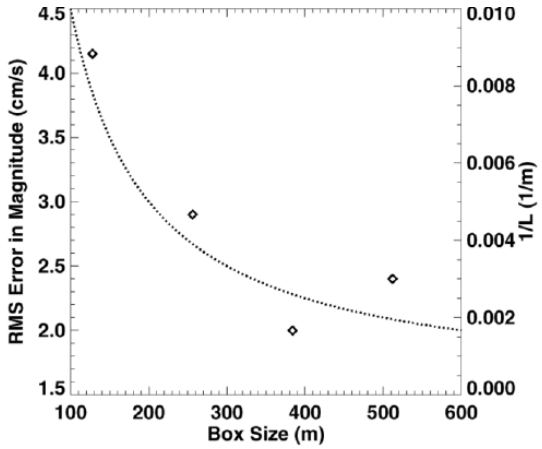

Figure 2.8: Relation between cube (box) size and RMSE for currents retrieved from airborne optical images. After: Piotrowski and Dugan (2002).

The relation between accuracy and cube size follows a pattern that reveals the same trend as the line that indicates the increase in resolution with increasing cube size (dotted line on right axis figure 2.8). Although the duration of the study is extremely short, figure 2.8 shows that spectral resolution and therefore accuracy is sensitive to the cube size.

On the other hand, small cube sizes are required to avoid the loss of small scale flow information due to spatial averaging over extensive horizontal areas. Thus, the selection of the cube size (spatial scale of wave dispersion analysis) is a fine balance between two contradictory requirements. There is no conflict for the stack size: bigger stack sizes are always preferred due to higher frequency resolution and a larger number of spectral components.

2.3. VALIDATION OF RADAR CURRENT MEASUREMENTS

Validation is comparing side-by-side measurements made with both a new and old instrument with known (and accepted) accuracy. In such a case it is important that both instruments measure the same physical quantity (Chapman and Graber (1997)). Validation of radar-derived currents is not straightforward, since a more elaborated interpretation of the current is required to find proper ground-truth validation data. It is well known that remotely sensed currents are near-surface currents. Young et al. (1985) describes the radar current to be a superposition of tidal currents, ocean circulations by the density field, current driven by wind stress in the upper layer of the ocean (Ekman layer) and wave-induced currents in the upper meters of the water column. The latter category includes, but is not limited to the effects of Stokes drift and the nonlinear wave-wave interactions (Young et al. (1985)).

The exact contribution of the wave-induced Stokes drift is still a major unknown in the theory on radar-derived currents. The research for the microwave X-band is limited to the study of Thompson et al. (1991). They proved the presence of a mean surface drift current in Doppler-spectra constructed from microwave Ku-band ($\lambda = 0.02m$) radar measurements. However, the physical mechanism that explains the presence of Stokes drift was not investigated, leaving Stokes drift as a major unknown in X-band radar current retrieval.

This issue is discussed more extensively for the High-Frequency (HF) band of the spectrum. This may be relevant for X-band radar currents as well, since HF and X-band follow the same physical laws and use the spectral representation of the same waves to fit the dispersion shell (Lund et al. (2015)). However, literature is inconsistent which part of the Stokes drift is included. Some studies (Graber et al. (1997);Laws (2001)) assume that full Stokes drift is included. Ardhuin et al. (2009) argue that HF radar currents include only parts of the Stokes drift and they compared their measurements with a filtered Stokes drift, derived by Broche et al. (1983). However, some authors argue (i.e. Rohrs et al. (2015)) that there is no effect of Stokes drift at all. They state that radar derived currents are Eulerian since radar backscatter is received from fixed regions in space, with which they implicitly state that the observation point does not follow motion of particles (Rohrs et al. (2015)). Authors arguing that radar currents are Lagrangian base their theory on the fact that waves are advected by their own mean drift velocity, which is incompatible with linear theory. They motivate the Stokes drift contribution to HF radar currents as a non-linear correction to the phase velocity (Rohrs et al. (2015)).

This ongoing discussion illustrates that an unambiguous definition of the physical quantity that a radar measures is not yet established. Therefore, no uniform validation procedure for radar-derived currents is set. The ignorance about the Stokes drift in radar images led to two commonly applied validation instruments for radar currents: a set of deployed drifters or moored ADCP/Current profilers. Even after the choice of an instrument (Eulerian/Lagrangian), validation is complicated since the measurements of both ADCP and drifters show considerable differences with the physical quantity that a radar measures.

Aspect/Instrument	Radar	Drifter	ADCP and moored current profilers
Instrument accuracy	Frequency resolution dependent	Slip (1-2 cm/s) from water they follow	2-5% of flow magnitude
Vertical scale of measurement	Integrated from surface to valid depth	Integrated over drag elements	Specific bins or depths
Horizontal scale of measurement	Average over extensive areas	Limited tracks in space following motion	Point
Stokes drift included	Not well-established	Yes	No

Nonetheless, drifters have been selected since the integrated value over a near-surface layer comes close to the nature of the radar measurement. Chapman and Graber (1997) provide the argument for the use of ADCP current data for validation of radar estimates of tidal currents. Tidal currents have low temporal and

spatial frequencies. This implies uniform tidal currents and wave dispersion over an extensive horizontal area. The average over this relatively large area may then be comparable to a point measurement, since a point measurement can be considered as a representative sampling point.

X-band radar-derived currents have been exclusively validated with measurements of a deployed ADCP. In studies that consider ADCP current measurements as ground truth, the issue of bin choice is relevant. It is common practice to select the upper bin available, aiming to approximate surface as close as possible. However, an argument often heard to avoid the use of the upper bin is that this bin is highly influenced by reflections from the free surface. This results from the fact that reflections from hard surfaces or the sea surface are much stronger than reflections from scatterers in the water column. Therefore other authors take measurements of the second available bin from the surface of the ADCP as ground truth. In a minority of the studies, comparison to depth-averaged ADCP currents is made.

Friedman (2014) validated tidal currents for a period of 10 days in relatively shallow water (<10 m) near the Sand Engine. The X-band radar near the Sand Engine operates with an antenna height of 17.45 m above the surface. The research shows a Root Mean Square Error of 0.17 m/s in a direct comparison of radar currents and Eulerian ADCP current measurements by the shallowest bin. The performance of the commercially available SeaDarQ algorithm was added as benchmark and showed a significantly higher RMSE of 0.28 m/s. In the same study, the results were split into ebb and flood currents which showed that ebb currents were slightly better estimated (RMSE 0.12 m/s) then flood currents (RMSE 0.19 m/s). van Gils (2014) validated the SeaDarQ algorithm for a two week period for the same ADCP location as Friedman (2014). In her study a RMSE of 0.187 m/s was found in a direct comparison between the radar-derived current and the in-situ 3.5 m depth-averaged surface current. Her research confirmed the preliminary research of Swinkels et al. (2012) to the accuracy of SeaDarQ. They obtained an RMSE of 0.2 m/s (radar vs. Delft3D hindcast) for current series of 2 days at the Amelander inlet.

In contrast to HF radar measurements, most X-band current extraction algorithms are commercially closed products and therefore purely scientific validation studies that quantitatively assess their current extraction capabilities are scarce. The only validation of X-band current estimates with the WaMoS II system was performed by Hessner and Nieto Borge (2012) for a 6-day period at Point Lonsdale near Melbourne. No quantitative evidence of the accuracy of WaMoS II currents with respect to a bottom-mounted upward looking ADCP (d = 20 m) was given in their work. However, a visual inspection of the correlation shows serious disagreements at several moments in time (figure 2.9).

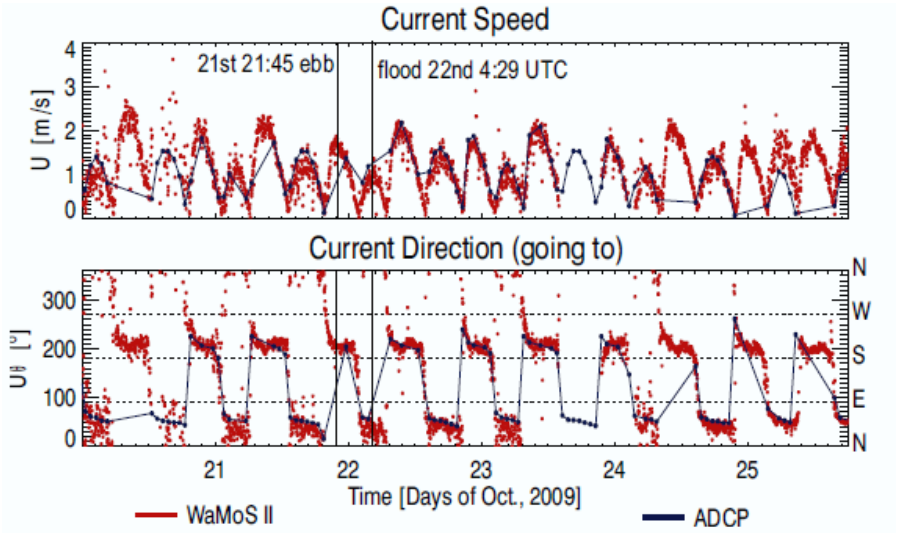

Figure 2.9: Results of validation of WaMoS II-currents with in-situ ADCP measurements

In absence of additional up-to-date X-band current validation studies two relevant validations for HF currents are mentioned here to provide a more complete overview of the possible accuracy of radar measurements nowadays. Robinson and Wyatt (2011) validated HF-radar currents with data of two ADCP for a

period of two years in Liverpool Bay. They showed solid evidence that hourly averaged HF-radar currents may be characterized by an RMSE of 0.1-0.3 m/s. The study of Rohrs et al. (2015) directly contributes to the discussion about the relevance of Stokes drift in radar current measurements. HF radar current measurements were compared to both drifter measurements (9 day period) and vertically integrated ADCP measurements (20 days). For both instruments, Eulerian, Lagrangian and a non-linear corrected Eulerian current were calculated. It was found that the drifter validation results showed higher RMSE values (0.16-0.19 m/s) compared to the ADCP validation results (0.08-0.1 m/s). It is worth noting that results of two different drifter types are processed in one general figure for the accuracy. The validation results for both instruments showed that the RMSE was lowest for purely Eulerian currents, while Lagrangian currents showed the lowest correlation. However, the method and circumstances under which this research was performed may raise questions about the general validity. The results are compared for radial currents in the direction of the radar. Therefore, on many instances in time only a fraction of the wave-induced Stokes drift is included. In addition, the magnitude of the Stokes drift is small since a deep water case (H_s = 2-4 m, d = 60-85 m) is considered and it is known that the effect of Stokes drift is small in deep water.

Exclusively HF radar derived current estimates have been validated with current measurements of drifters. In addition to the study of Rohrs et al. (2015), two studies are discussed here. The study of Stewart and Joy (1974) compared currents in a deep water situation to individual tracks of six drifters. The agreement for only one specific frequency was examined with current data from six individual drifters that were drogued at the effective depth of the radar-derived current for the considered frequency. Two periods of 1-2 hours were validated. After accounting for radar uncertainty, the agreement between 20 min-averaged measurements was close to a few centimeters per second. Although the study has an extremely short duration, it is confirmed that a drifter drogued at the right depth is a fundamentally right instrument to serve as ground truth for radar comparison.

Recent studies that select drifter current measurements as in-situ ground truth to validate radar-derived currents emphasize that drifter and radar measurements should be compared on the same spatial and temporal scale. The drifter ground truth is then formed by temporally and spatially averaged measurements of multiple drifters in a fixed area in space (Ohlmann et al. (2007);Lipa et al. (2009)). An experimental setup was developed by Ohlmann et al. (2007) to work out this approach. The experimental setup is shown in figure 2.10. The figure shows that the experiment is designed to compare radar and in-situ currents on a fixed grid cell. During the entire study period, drifters are repetitively replaced in the fixed square study area as soon as they drift out. The end positions are marked with a cross. In order to compare radar and in-situ drifter currents on the same spatial scale, the cube size (spatial scale of the radar derived current) was chosen equal to the fixed grid cell. Hourly averages for radar and in-situ currents were obtained for deployment sessions of 3.5-7.5 h duration on 7 non-successive days. An average difference of 6.5 cm/s was found. However, the question is whether this figure for the accuracy is representative for the method, since only a very limited number of time stacks are involved in the analysis.

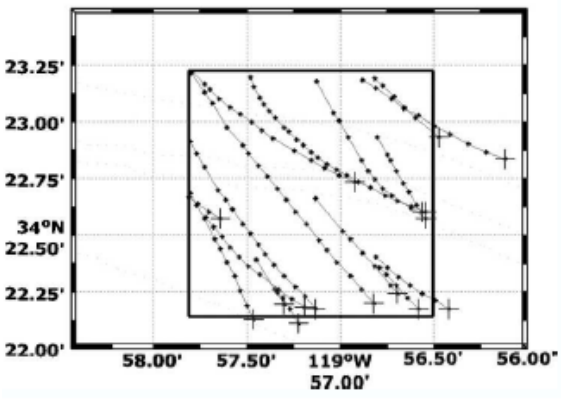

Figure 2.10: Drifter measurement setup for validation of radar-derived currents. After: Ohlmann et al. (2007).

3

SAND ENGINE X-BAND RADAR MEASUREMENTS

The complexity of selecting proper in-situ ground truth data for radar current validation was addressed in the previous chapter. In this chapter, the hardware and software used to retrieve radar currents are described. First, characteristics of the X-band radar at the Sand Engine and its data are provided in section 3.1. Section 3.2 continues with a detailed description of XMFit, the depth-inversion algorithm used to estimate near-surface currents in this study. Finally, section 3.3 motivates the selection of the solver chosen to estimate the currents in this thesis work.

3.1. X-BAND RADAR DATA

The image series of a single land-based X-band radar at Kijkduin (X 74757.6m RD, Y 453830.5m RD) are analyzed to retrieve the radar currents. The radar (hardware) is located approximately 3 km north of the Sand Engine. The aim of this radar is to monitor the current patterns and bathymetry at the Sand Engine. The land-based radar operates with an antenna height of 17.45 m +NAP, a wavelength of approximately 3 cm and has 21 r.p.m., corresponding to a rotation time of 2.85 s.

The radar is equipped with the commercial SeaDarQ software with which polar images of the sea surface are obtained. The SeaDarQ software assigns UTC time stamps to the images. The polar radar images are transformed to a Cartesian grid. A raw Cartesian radar image consists of 2048 x 2048 pixels. With a pixel size of 3.75 m, this results in an effective output range of 3837 m which is sufficient to study flow characteristics at the Sand Engine. To retrieve current information, stacks of 128 radar images are selected from the continuous series of images. The extraction of stacks of 128 images leads to a 6.1 minutes interval between two successive image series. This stack size is selected since it best corresponds to the 5-min averaged in-situ ADCP data.

3.2. XMFIT ALGORITHM DESCRIPTION

XMFit is an open source X-band depth-inversion algorithm, implemented in a MATLAB environment. The description of the algorithm is solely based on the work of Friedman (2014). The internal work flow of the XMFit algorithm is depicted in figure 3.1. This section will be devoted to describe the elements in figure 3.1 in more detail. The building blocks shown in the figure will form the framework of the description.

XMFit completes the procedure shown in the red box for a single time stack of radar images. XMFit loops through the procedure in the red box in case of multiple time stacks selected. First the output grid is constructed. The output grid is defined as the set of points located within the radar domain for which XMFit will provide estimations of d and $\vec{U}_e$ (upper panel spatial settings). The output of XMFit are maps of depth and current estimates (panels rightmost). The procedure shown in the red box is executed per output grid point. The grid point forms the center X_c, Y_c of the computational cube that is Fourier transformed (lower panel 'spatial settings'). The spatial dimensions of the computational cube are given by a number of pixels N_i in both x- and y-direction. The temporal dimension of the computational cube is given by the number of images in the time stack N_w.

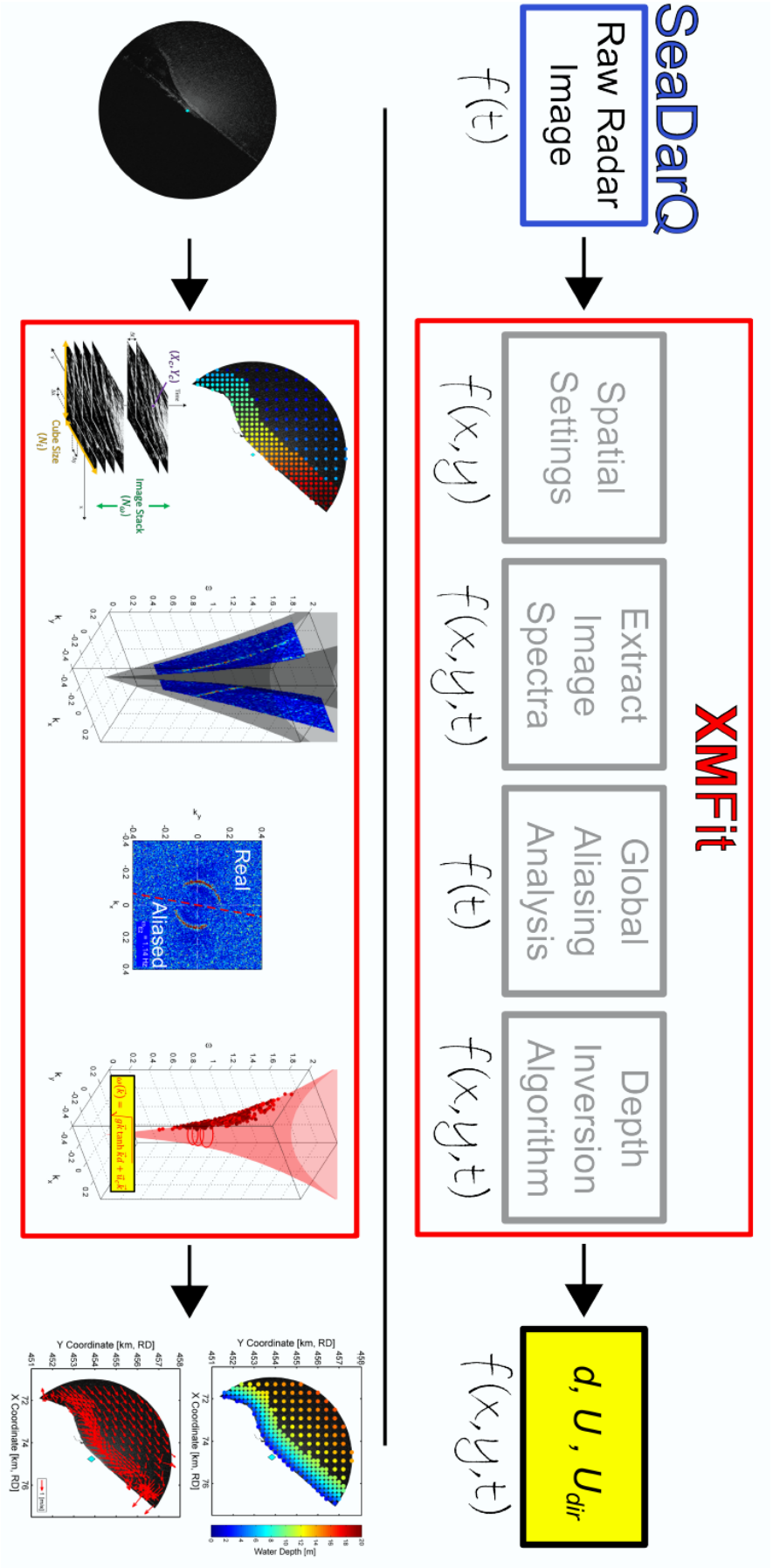

Figure 3.1: XMFit Model architecture. After Friedman (2014).

A 3D FFT analysis (section 2.1.2) is applied to obtain the raw image spectrum $F(\tilde{k_x}, \tilde{k_y}, \tilde{\omega})$ and the power spectrum density $I(\tilde{k_x}, \tilde{k_y}, \tilde{\omega})$. The two parameters N_i and N_ω determine the spectral resolution (dk, dω) of the image spectrum. Spectral energy of aliased wave components is removed from the image spectrum by a wave directional filter. This filter is illustrated in figure 3.2. The mean wave direction is extracted from the 'aliasing cube', which is a special computational cube that is exclusively used for finding the mean wave direction. The size of the aliasing cube covers the majority of the radar domain in order to obtain a reliable estimation for the mean wave direction (red arrow). The line orthogonal to the mean wave direction is calculated (red dotted line). This line represents a propagating wave crest coming from the mean wave direction. This line is placed 1:1 atop of the image spectrum to devide the spectrum in two parts. The points in the image spectrum for a given frequency level are attributed to two clusters (see Friedman (2014) for more details) representing 'real' and 'aliased' energy respectively (figure 3.1). The spectral components that represent 'aliased' energy are removed by deleting that part of the spectrum (right panel figure 3.2).

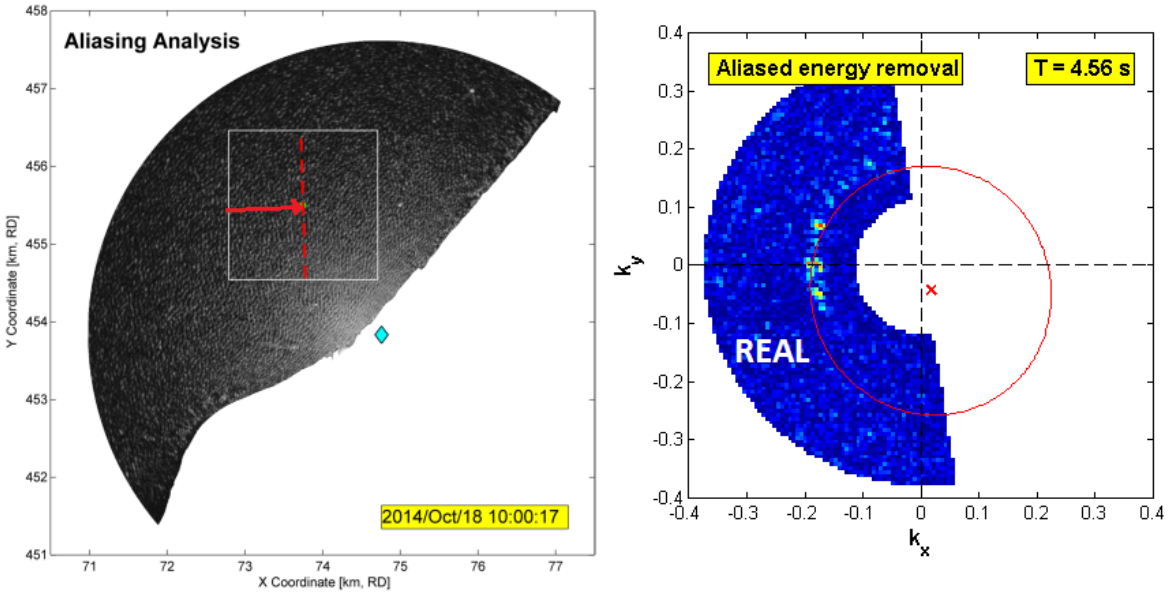

Figure 3.2: Aliased spectral energy is removed by cutting of half of the spectrum, based on the Global Aliasing mean wave direction.

Wide dispersion and frequency filtering is applied to remove spectral components that are unrealistic for the study site. Spectral components that fall outside the user defined physical lower and upper limits for k and ω are removed. The limits for k are dictated by the depth limits 1.5 m and 30 m, while the limits for ω are dictated by the realistic wave periods that may occur at the Sand Engine: 3-12 s. These filtering operations result in the cutoffs within the image spectra, resulting in two planes (figure 3.1). The filtered image spectrum is loaded into the actual depth-inversion algorithm or 'solver'. In XMFit, nonlinear regression and least squares optimization are available. Both fit the Doppler shifted-linear dispersion relation (equation (2.4)). Additional solving options are built in, which fit a different equation (see below) but solve according to the nonlinear regression principles:

- Higher order wave theory: a dispersion relation based on **non-linear ocean gravity waves**, referred to as Stokes waves (Holthuijsen (2009)):

$$\omega = \sqrt{g|k|tanh(|k|d) * \left(\left(1 + \left(\frac{H}{2}\right)^2 * \frac{8 + cosh(4|k|d) - 2(tanh(|k|d)^2)}{8 * (sinh(|k|d))^4}\right)\right)} + \vec{k}\vec{U}_e \tag{3.1}$$

- Intrinsic: linear dispersion relation in absence of current (equation (2.2))
- AssimD: Linear dispersion relation (equation (2.4)) in which the known in-situ depth d is substituted
- AssimU: Linear dispersion relation (equation (2.4)) in which the known in-situ $\vec{U}$ is substituted
- Emperical: empirical form of the linear dispersion relationship

The final filtering step is inside the depth-inversion procedure. A spectral energy threshold E_{lim} is applied that functions as high-pass filter for the spectral signal. This spectral energy threshold is applied to separate noise and higher harmonics from spectral energy from ocean waves following the linear dispersion relation. The value for E_{lim} is selected adaptively by XMFit as follows (Friedman (2014)):

- A value for E_{lim} is selected
- Noise is filtered out by applying the spectral energy threshold to the spectral data.
- Wave dispersion equations are being fit to the filtered image spectrum, resulting in estimates of $\vec{U}_e$ and d. Root Mean Square Error for the fit is calculated.
- Procedure is repeated for multiple values of the spectral-energy threshold.
- Optimum spectral-energy threshold E_{lim} is selected based on lowest RMSE for the fit. The associated estimates of $\vec{U}_e$ and d are selected as output of XMFit for the output grid point under consideration.

3.3. SELECTION OF CURRENT RETRIEVAL SOLVER

The assimilated depth solver in XMFit is used to obtain the current estimates throughout this thesis work. By selecting the assimilated depth solver, the analysis is exclusively on the current estimates. The influences of the depth in the fitting procedure is eliminated, since the known in-situ depth is substituted in the linear dispersion relation. The in-situ depth is extracted from the combination of monthly bathymetric jet-ski surveys and the average value for Hook of Holland and Scheveningen water levels.

4

POINT VALIDATION

The aim of this thesis work is to validate radar-derived currents obtained by analyzing wave dispersion in computational cubes with various spatial scales. This chapter provides the answer to the subquestion *How do accuracy and spatial scale of wave dispersion analysis relate for a single point and a fixed temporal scale?* Point validation is relevant to obtain a detailed understanding of the tidal current extraction capabilities of X-band radar under various (environmental) conditions in time. In addition, results of the Eulerian point validation may provide a significant contribution to the discussion on Stokes drift in radar-currents.

Radar currents measured with cube sizes of 240 m, 480 m, 960 m and 1920 m are compared with in-situ ADCP current measurements at two locations. This chapter starts with providing an overview of the in-situ current and wave data in section 4.1. It is followed by a detailed description of the validation approach in section 4.2. Section 4.3 presents the results of the validation of the radar-currents.

4.1. IN-SITU ADCP AND WAVE MEASUREMENTS

X-band radar current measurements are compared to in-situ current measurements of two Acoustic Doppler Current Profilers (ADCP) near the Sand Engine. The locations of both ADCP are shown in figure 4.1. In the following, both instruments are marked as ADCP E and ADCP F respectively. Both ADCP instruments were deployed in the context of the MegaPEX campaign: a six weeks field experiment in the fall of 2014. The measurements from October 20^{th}, 2014 to October 27^{th}, 2014 were selected for point validation of radar currents. This period was selected since it includes both storm conditions and normal tidal flow. Figure 4.2 shows that the shear in the current profiles as measured by the ADCP is minimal. Currents have a relatively uniform magnitude over depth. This is directly linked to the fact that both instruments are measuring in relatively shallow water (figure 4.1). The ADCP measurements of the upper bin may thus be interpreted as the "mean" tidal flow.

Both ADCP instruments were upward looking and bottom mounted. Bin extent is set to 0.5 m. ADCP E (X 73854 m RD, Y 454000 m RD) was programmed for 12 bins, starting from -3.78 m NAP to +1.72 m NAP, resulting in a 'visible' range from -4 m NAP to + 2 m NAP. ADCP F (X 74832 m RD, Y 455334 m RD) was set up for 16 bins, starting from -5.87 m NAP to +1.73 m NAP. The current profile that is in the visible range for ADCP F is located between - 6 m NAP and + 2 m NAP. However, the upper 1-1.5m of the water column is not profiled by both ADCP (figure 4.2). This means that velocity contributions from (near-) surface processes are not included in the ADCP measurements. However, the radar current measurements cover particularly the near-surface layer of the water column.

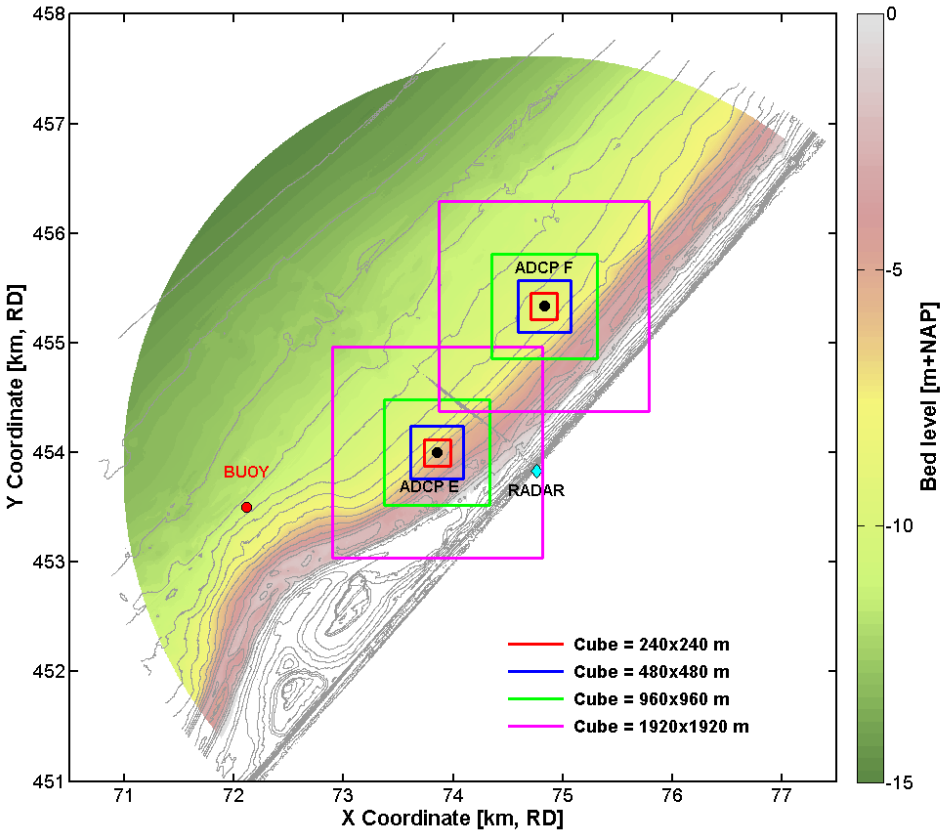

Figure 4.1: Locations of ADCP and wave buoy in relation to Sand Engine bathymetry, depth contours every 0.5 m.

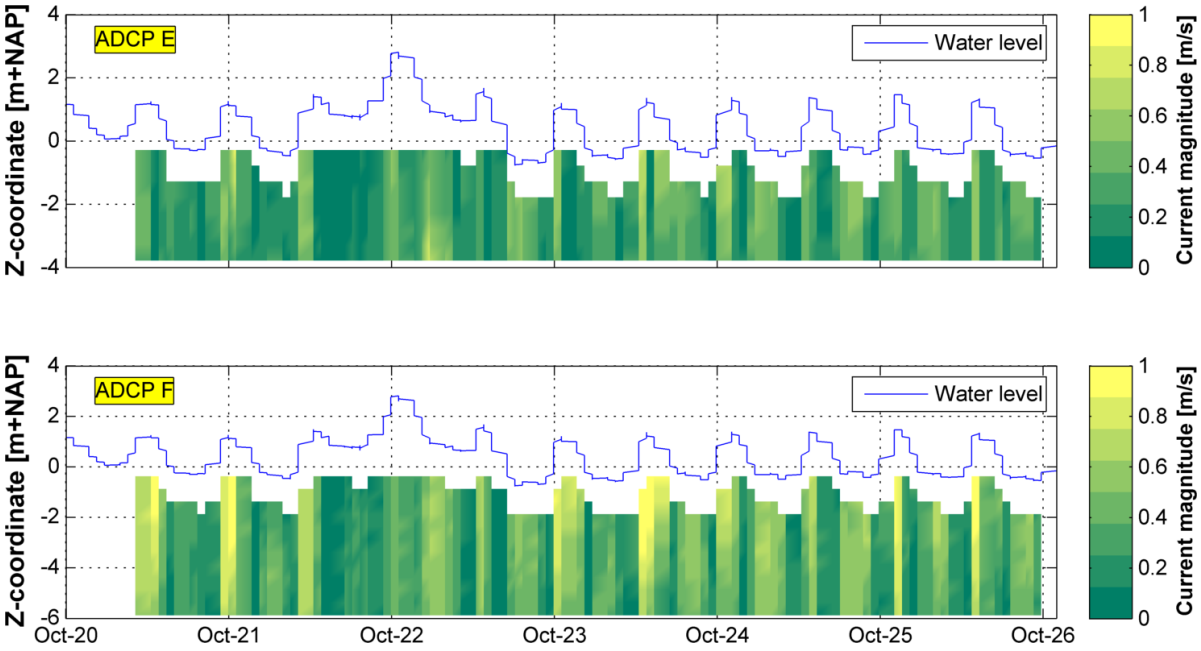

Figure 4.2: Current magnitude distribution over depth for ADCP E and F

The accuracy of the ADCP is ± 2-5% of the velocity magnitude. The ADCP measurements have been averaged over 5-minute intervals. The ADCP measures in local time zone UTC+1. Series have been converted from UTC+1 to UTC time zone to allow for comparison in the same time frame as the radar data.

Data from a directional wave buoy is used as benchmark to investigate if XMFit fits on the correct spectral energy. Significant wave height, peak period and peak wave direction have been extracted from a deployed TRIAXIS^{TM} Directional Wave Buoy (X: 72113 m RD, Y: 453502 m RD), which is approximately 1 km from the coastline (figure 4.1). The wave buoy data is measured in UTC+1 and is therefore converted from UTC+1 to UTC. Wave characteristics are averaged over 20 minutes. Wave height measurements are measured with an error of approximately 0.5 %. For the wave period this error is 1%, while the wave direction has an error of approximately 3%.

The record of the significant wave height (upper panel figure 4.3) shows a distinct peak in the wave height from October 21st 12:00 - October 22nd 18:00. Wave heights above 2 m are indicated as storm conditions. The start and end of the storm is marked with red lines in figure 4.3. The maximum value of the significant wave height during the storm approximates 5 m, which is associated with wave periods that have a maximum of approximately 10-12 s (bottom panel). The wave direction during the study period is from west to northwest (270-320°N). It is remarked that the wave direction represents the direction from which the waves arrive. Coverage of wave record is not complete for the study period, two limited periods without data do exist in the record. However, this does not limit the analysis since the time series are sufficiently long for the intended analysis.

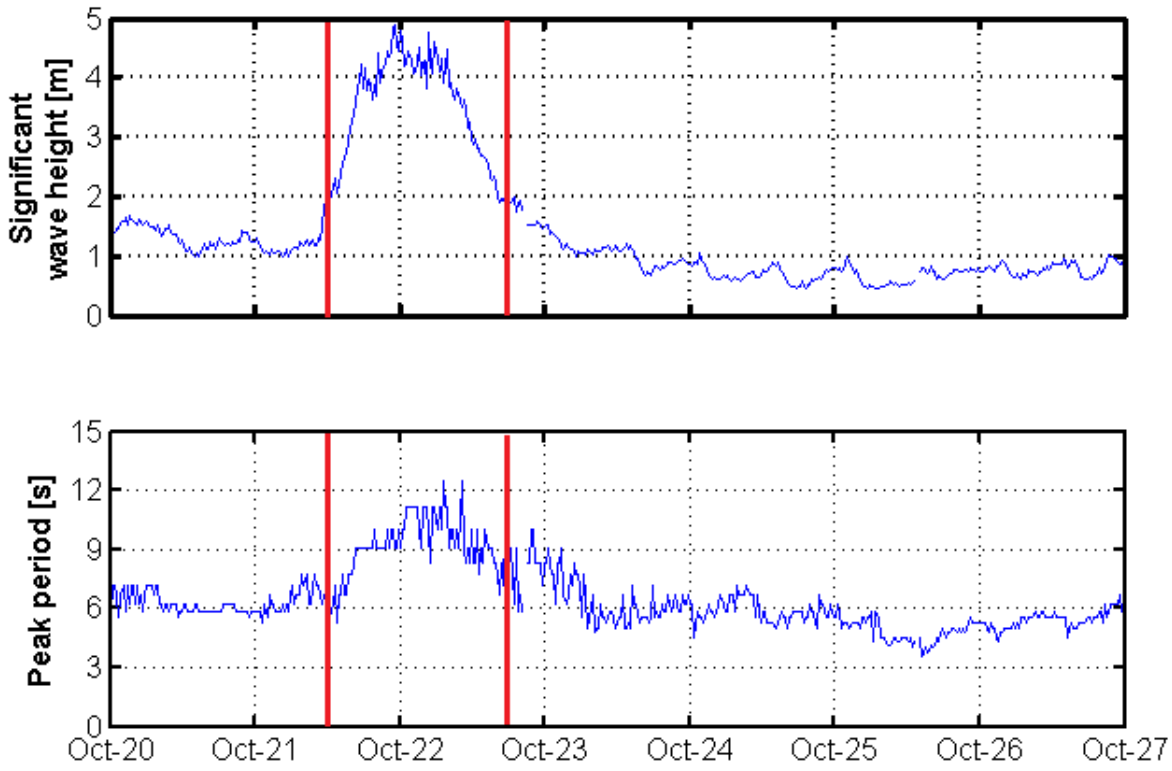

Figure 4.3: Wave buoy record of the significant wave height and peak period

4.2. APPROACH

Radar-derived currents are (near-) surface currents. Intuitively, the measurements of the shallowest bin of the ADCP are selected as ground truth for radar current validation. However, figure 4.2 showed that this bin is located 1 - 1.5 m below the water surface, which indicates that hydrodynamic processes in the upper layer are missed by the instrument. In shallow water, the non-linear Stokes drift is the main hydrodynamic process in the upper layer of the ocean. Water particles that experience Stokes drift do not follow closed (circular) orbits

prescribed by the linear theory. Instead, they experience residual motion in wave propagation direction over one wave period. This residual motion implies a net onshore directed mass transport. A net mass transport means that particles experience a net Stokes drift velocity in the wave propagation direction. The magnitude of the Stokes drift velocity for an individual wave (hereafter referred to as: Stokes drift) is given by the well-known formula for Stokes drift in the near-shore:

$$u_s(k,z) = \omega k a^2 \frac{cosh(2k(d+z))}{2(sinh(kd))^2} \tag{4.1}$$

u_s represents the Stokes drift, k the wave number, z the depth-coordinate measured from the surface, ω the wave frequency, a the wave amplitude and d the local water depth. The formula shows that Stokes drift is non-linear in wave amplitude a. The non-linear effect becomes stronger for higher waves in shallow water. Figure 4.3 already indicated that the significant wave height was > 2 m during 20 % of the study period. Moreover, the Stokes drift velocity is important when the considered time scale is large compared to the time scale of the wave motion. This is applicable when considering radar currents (time scale of minutes) with wave motion on a timescale of seconds. Both arguments give a strong indication that Stokes drift may provide the additional information to fill up the lack of measurements for the upper 1-1.5 m of the water column.

Besides, the Stokes drift velocity is a crucial aspect since it is a process that is only measured in a Lagrangian frame of reference that follows a water particle in space and time. If the Stokes drift velocity is used to fill up the lack of velocity measurements for the upper 1-1.5 m of the water column, it is thereby implicitly assumed that radar-derived currents are Lagrangian. The Stokes drift is not measured in Eulerian ADCP measurements at a fixed position in space. This directly links to the discussion in literature about which part of the Stokes drift is included in radar-derived currents (section 2.3). The work of Thompson et al. (1991) showed the presence of Stokes drift in microwave radar measurements. This finding justifies the inclusion of the Stokes drift velocity in the ground truth measurements from theoretical point of view. The studies stating that (HF) radar currents are Eulerian did not show solid evidence for an extensive period over time.

Therefore, in this thesis work the Eulerian ADCP measurements are not used directly as ground truth. Instead, the Eulerian ADCP measurements are corrected for the Stokes drift. By correcting Eulerian ADCP currents for the Stokes drift, this thesis work provides knowledge on Stokes drift in X-band radar images directly from observed data. The Stokes drift corrected ADCP measurements are termed pseudo-Lagrangian ADCP currents. They are called pseudo-Lagrangian since the in-situ measurements are Eulerian, but inclusion of the Stokes drift make them 'act' as Lagrangian measurements. The pseudo-Lagrangian ADCP current measurements form the ground truth for direct comparison with X-band radar currents. If the correspondence between pseudo-Lagrangian ADCP and radar current is high, this may strengthen the argument that X-band radar currents are Lagrangian measurements.

The discussion in the previous chapter also touched the ignorance about which part of Stokes drift is included in radar currents (assuming radar currents are Lagrangian). Here the same issue is applicable. In this thesis, it is assumed that it is the **mean surface Stokes drift** based on the fact that radar-currents are derived from scattering elements at the sea surface. It was decided to calculate the average Stokes drift at the surface since the radar-derived current is a weighted averaged current derived from dispersion of multiple waves.

The Stokes drift correction to obtain pseudo-Lagrangian ADCP currents from Eulerian ADCP measurements implies the vectorial summation of the current measured by the shallowest bin of the ADCP and the mean surface Stokes drift. In order to calculate the mean surface Stokes drift velocity, the Stokes drift of every single imaged wave in the computational cube shall be taken into account. Ideally the Stokes drift for each individual wave in the computational cube is calculated and then averaged. However, a directional wave spectrum was not recorded by the buoy. Only the significant wave height is available (figure 4.3). Therefore, it was necessary to substitute mean wave parameters to calculate the mean surface Stokes drift (z=0):

$$\bar{u_s}(\bar{k},0) = \bar{\omega}\bar{k}a^2 \frac{cosh(2\bar{k}d}{2(sinh(\bar{k}d))^2} \tag{4.2}$$

$\bar{\omega}$ and $\bar{k}$ are the average wave frequency and wave number calculated from the image spectrum and a the wave amplitude corresponding to the significant wave height measured by the wave buoy. Finally, it is assumed that the contribution of the mean surface Stokes drift to the current is directed in the *peak wave*

direction of the wave field. The peak wave direction is also extracted from a directional wave buoy, deployed near the tip of the Sand Engine (reference is made to figure 4.1). It is logical to expect that waves in the near-shore are affected by wave refraction. However, wave refraction does not have a big influence on the Stokes drift magnitude and direction at both ADCP locations. This may be concluded since the wave buoy and both ADCP are all located in an area where the depth contours are already parallel to the shoreline (figure 4.1). Therefore it is justified to take the wave amplitude a and peak wave direction **at the buoy location** as representative for both ADCP locations.

4.3. RESULTS

In this section, the validation results for two single points in the radar domain are presented. A current is a vectorial quantity. A vector may be described by a magnitude and direction or is decomposed in its components. In this thesis, the results will be shown in either the magnitude-direction or the alongshore/cross-shore representation of the vector. Both representations are explained in figure 4.4 for a positive alongshore current of 1 m/s. The left panel shows the magnitude-direction representation. The length of the current vector indicates the magnitude of the current. The direction is given by the angle between current vector and north arrow. This angle is 45 ° for the current considered here. The right panel shows the alongshore/cross-shore representation. A positive alongshore current of 1 m/s is considered here. Therefore, only the alongshore component is observed in the figure. Note that positive alongshore currents are directed northeast (coincide with flood currents) and positive cross-shore current are onshore directed.

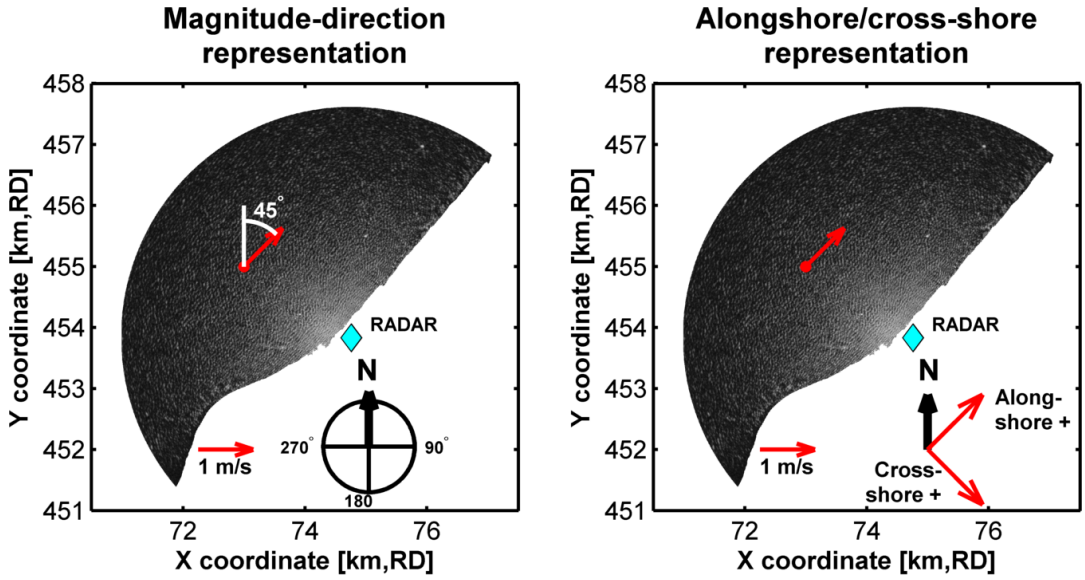

Figure 4.4: Conventions used for current representations, illustrated for a positive alongshore current of 1 m/s.

4.3.1. HIGHEST ACCURACY-CASE

Here, the results of a direct comparison of XMFit current estimates and pseudo-Lagrangian ADCP currents are presented for two locations. A cube size of 960 m is chosen for this comparison since this cube size results in most accurate current estimates by the radar. The direct comparison will then directly reveal on which moments in time radar estimates need improvement. Figures 4.5 and 4.6 illustrate the correspondence between radar current and pseudo-Lagrangian ADCP current time series for ADCP E and F respectively.

The agreement with the ADCP measurements is characterized by a RMSE of around 0.2 m/s at both locations. Differences in direction between XMFit and ADCP do occur exclusively during slack tide, where the ADCP direction in general turns clockwise and the XMFit current direction in general turns counterclockwise (lower panels figures 4.5 and 4.6). However, these differences do not significantly influence the accuracy of the current estimate, since the current magnitude during slack tide has a value near zero (upper panels figures 4.5 and 4.6). Tidal currents during non-storm conditions have good visual agreement, but at several moments in time the maximum ebb- and flood currents are overestimated (ADCP E) or underestimated (ADCP F) respectively.

It is evident that for both ADCP locations the correlation between in-situ and radar current magnitudes is significantly lower during the storm period (between blue lines) where $H_s > 2$ m. In the remainder of this section, the quality of fit during both storm and non-storm conditions is examined separately.

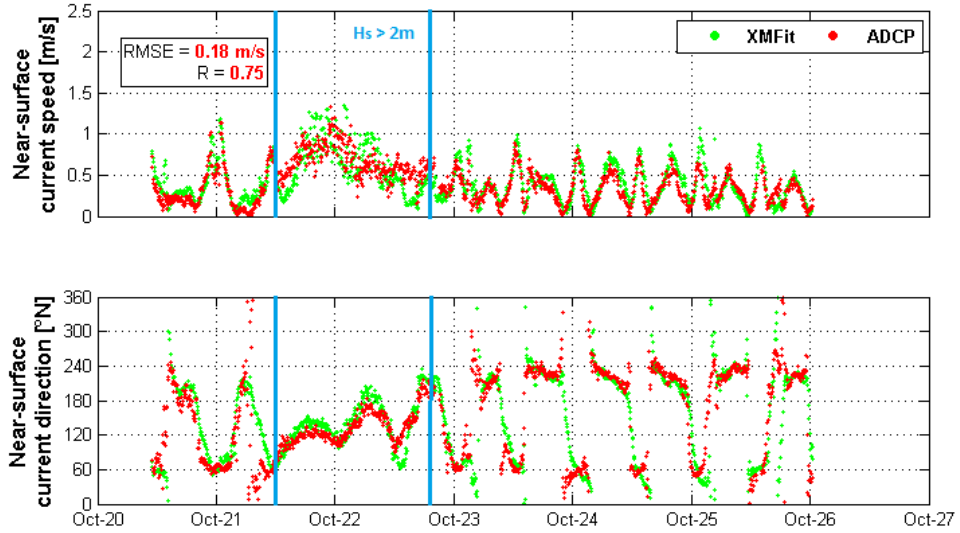

Figure 4.5: Direct time series comparison between XMFit and in-situ current data of ADCP E

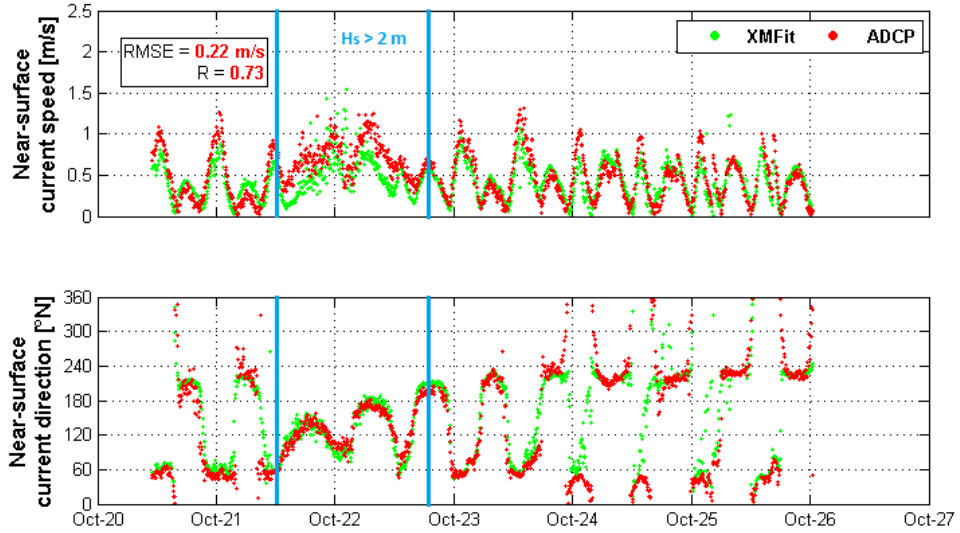

Figure 4.6: Direct time series comparison between XMFit and in-situ current data of ADCP F

Tidal movement

The visual correspondence between the radar-derived current and in-situ data is good during non-storm conditions. Here the tidal recognition capabilities of XMFit during calmer conditions is examined quantitatively. XMFit and ADCP current measurements during non-storm conditions have been separated into flood and ebb currents. Figure 4.7 shows that flood currents are estimated accurately by XMFit at ADCP E. The current data has a relatively small and uniform spread (RMSE 0.16 m/s). The spread is smaller for ebb currents (RMSE 0.12 m/s). A slight tendency to overestimate ebb currents is observed.

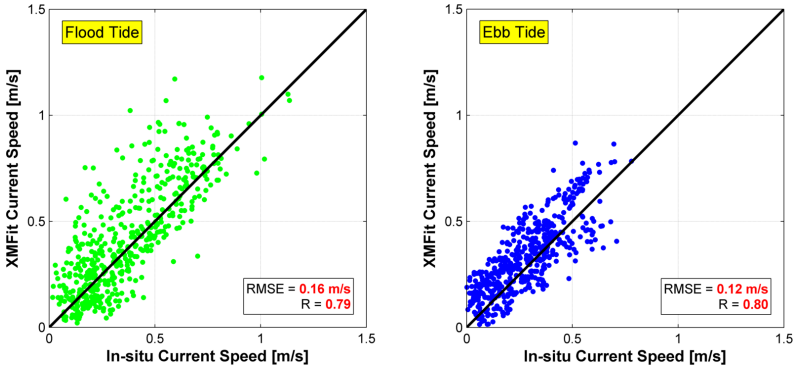

Figure 4.7: Direct scatter comparison of flood and ebb currents during non-storm conditions, ADCP E

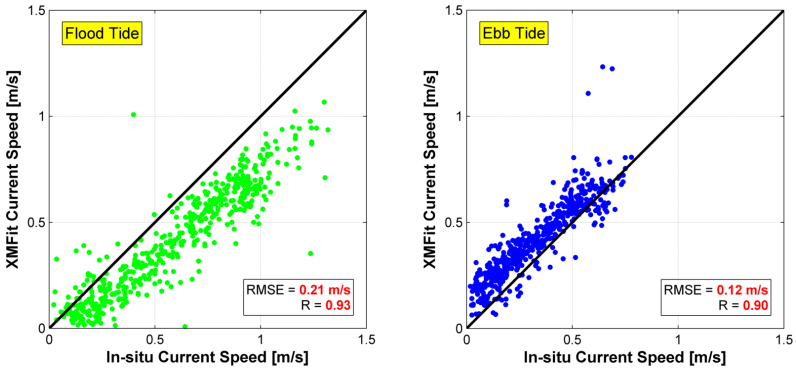

Figure 4.8: Direct scatter comparison of flood and ebb currents during non-storm conditions, ADCP F

The scatter plots for the location ADCP F (left panel 4.8) show that flood currents are consistently underestimated by XMFit. However, the pattern is oriented almost parallel to the line of perfect agreement, which may indicate bias. The XMFit current estimates for the location of ADCP F have a high accuracy during ebb tide (right panel). The ebb currents are estimated with the same accuracy as for ADCP E, however for ADCP F a clear and consistent overestimation of ebb currents is observed.

Storm conditions

The current direction during the storm conditions showed an onshore directed flow (between 60° and 200°). It is thus expected that the main difference in the current magnitude during the storm stems from the cross-shore component. Current estimates of XMFit and measured in-situ currents during the storm period have been decomposed in their alongshore and cross-shore components.

The radar alongshore current at the ADCP has an accuracy (RMSE 0.23 m/s) that is comparable to the accuracy for flood currents under normal tidal conditions (left panel figure 4.9). As expected, the alongshore component is relatively small during the storm. The right panel of the figure shows that the magnitude of the cross-shore component during the storm is much higher. Compared to the scatter plot of the alongshore currents, the RMSE is considerably higher for cross-shore current components. The majority of the data points is located below the line of perfect agreement, which indicates that XMFit has a tendency to underestimate the cross-shore magnitude at ADCP E.

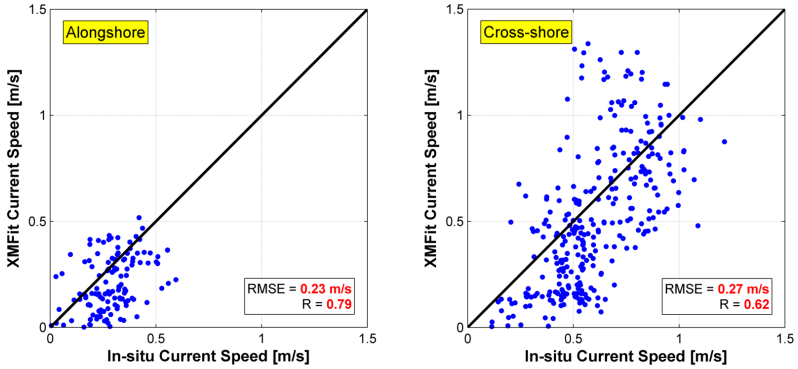

Figure 4.9: Direct scatter comparison of XMFit and in-situ current measurements during storm conditions at location of ADCP E

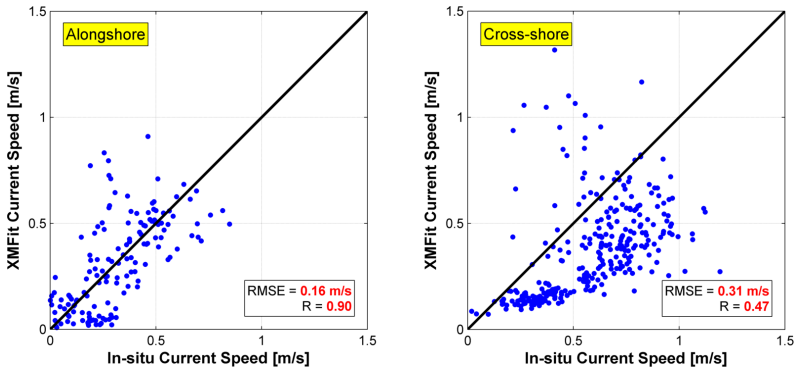

Figure 4.10: Direct scatter comparison of XMFit and in-situ current measurements during storm conditions at location of ADCP F

The accuracy of the alongshore current component at ADCP F (RMSE 0.16 m/s) is comparable to the accuracy of normal tidal flood currents. The magnitude of the alongshore component is relatively small during the storm. The right panel of figure 4.10 shows the scatter plot for the cross-shore current for the location of ADCP F. This scatter plot confirms the observations found for the location of ADCP E. Again, the data shows low agreement (RMSE 0.3 m/s). It is also evident that cross-shore currents are underestimated in this case.

4.3.2. XMFIT SPECTRAL ENERGY SELECTION

In the previous section it was shown that XMFit is able to extract the tidal flow with reasonable accuracy. The accuracy was found to be significantly lower during storm conditions. This section investigates the correspondence between wave parameters determined by XMFit and the deployed directional wave buoy **at the location of the wave buoy**. The comparison of wave parameters is added as benchmark since it is a good metric to check if XMFit is fitting the correct spectral energy. A good correspondence between XMFit and in-situ wave parameters indicates confidence in XMFit methodology for this period in time. The selection of the correct spectral energy by XMFit is reflected in good correspondence between XMFit and wave buoy peak periods. The peak period from XMFit is calculated from the top energy ω-slice of the spectrum. A good correspondence in peak wave direction indicates that the spectral energy cutoff is selected properly by XMFit.

Figure 4.11 shows comparison of the peak period (upper panel) and peak wave direction (bottom panel). The peak period estimated by XMFit during storm conditions does not show close agreement with the wave buoy measurement. The peak period is extremely sensitive to the wave field in time and therefore some variation is inherent to the peak period metric (observe wave buoy record). However, the variation in XMFit peak period signal is unexpectedly high during the storm. Estimations of XMFit for successive time steps may show differences up to 2-3s. This relatively high variation indicates that XMFit may has difficulties in fitting the right spectral energy during the storm period. However the general trend follows the wave buoy record. During **non-storm** conditions, XMFit consistently underestimates the peak period (upper panel figure 4.11). The variation in Tp under calmer conditions is comparable to the variation in the wave buoy record.

During storm conditions, the peak wave direction of XMFit does align relatively well with the in-situ wave buoy measurements. The line of the wave buoy measurements is located approximately in the center of the point cloud during the storm. During **non-storm conditions** it is observed that XMFit constantly estimates that the peak wave direction is 270 °, while the wave buoy measures a peak wave direction corresponding to approximately north-northwest.

The results of the wave buoy comparison showed that the agreement in wave direction is relatively good, thus indicating a proper selection of the spectral energy cutoff. The high variation in Tp during the storm is most probably caused by rain and fog that was observed in the radar images. Furthermore, the series for the peak period showed that XMFit tends to slightly underestimate the peak period during **non-storm** conditions. It is expected that this is due to a dominant role of short waves (period T = 3-6 s) in the fitting procedure of XMFit. This is further discussed in section 6.3.2.

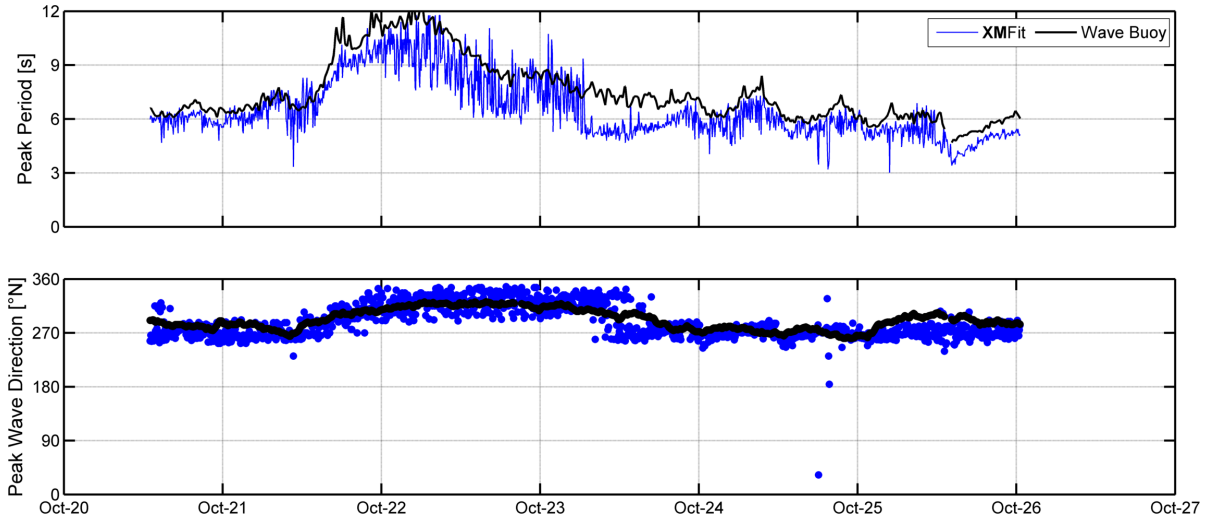

Figure 4.11: Direct comparison of peak period and peak wave direction estimated by XMFit and measured by wave buoy

4.3.3. THE INFLUENCE OF SPATIAL SCALE OF WAVE DISPERSION ANALYSIS

The validation of radar current time series obtained with a cube size of 960 m showed that XMFit was able to accurately extract flood and ebb currents during non-storm conditions. Here it is examined if the same applies for radar currents extracted with cube sizes of 240 m, 480 m and 1920 m under flood and ebb conditions respectively.

Figure 4.12 shows that the relation between cube size and accuracy of ebb currents has the form of a hyperbolic function with a horizontal asymptote of 0.16 m/s. The relation for flood currents at ADCP F may also be approximated by a hyperbola with an asymptote of 0.2 m/s. However, the relation for flood currents at ADCP E has the form of a parabola with a minimum at 480 m or 960 m. The accuracies that are shown are calculated with data exclusively during **non-storm** conditions.

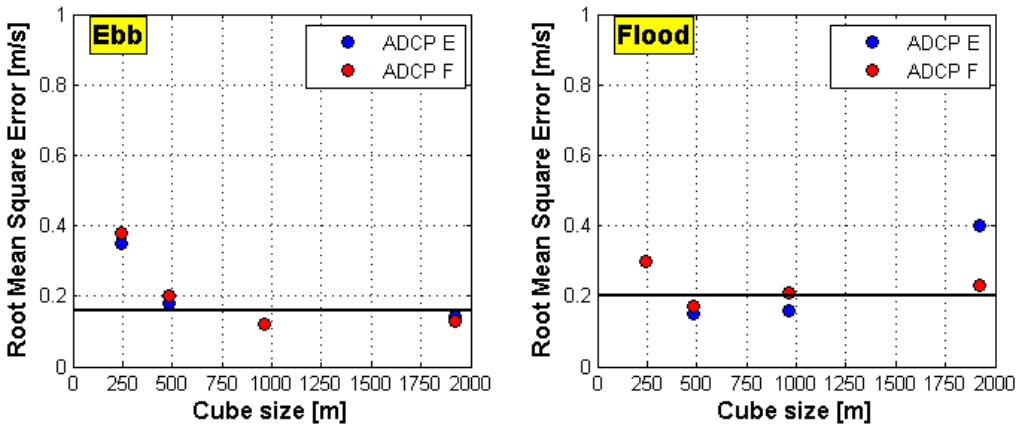

Figure 4.12: Relation between Root Mean Square Error and XMFit cube size during non-storm conditions

A significantly lower accuracy of radar currents is obtained by using a cube size of 240 m. Furthermore, the RMSE at the location of ADCP E for a cube size of 1920 m is remarkable. To explain the origin of the higher RMSE, the XMFit current time series obtained with cube sizes of 240 m, 480 m and 1920 m are compared to the series obtained with a cube size of 960 m. The time series for the four cube sizes considered here are visualized in figures 4.13 and 4.14 for ADCP E and F respectively.

The XMFit current time series obtained with cube sizes of 240 m, 480 m and 1920 m roughly follow the same pattern over time. It is immediately observed why a cube size of 240 m results in inaccurate estimates. The current magnitude for normal tidal flow is consistently higher for a cube size of 240 m compared to the results obtained with a cube size of 960 m. This is illustrated by a (1) in both figures.

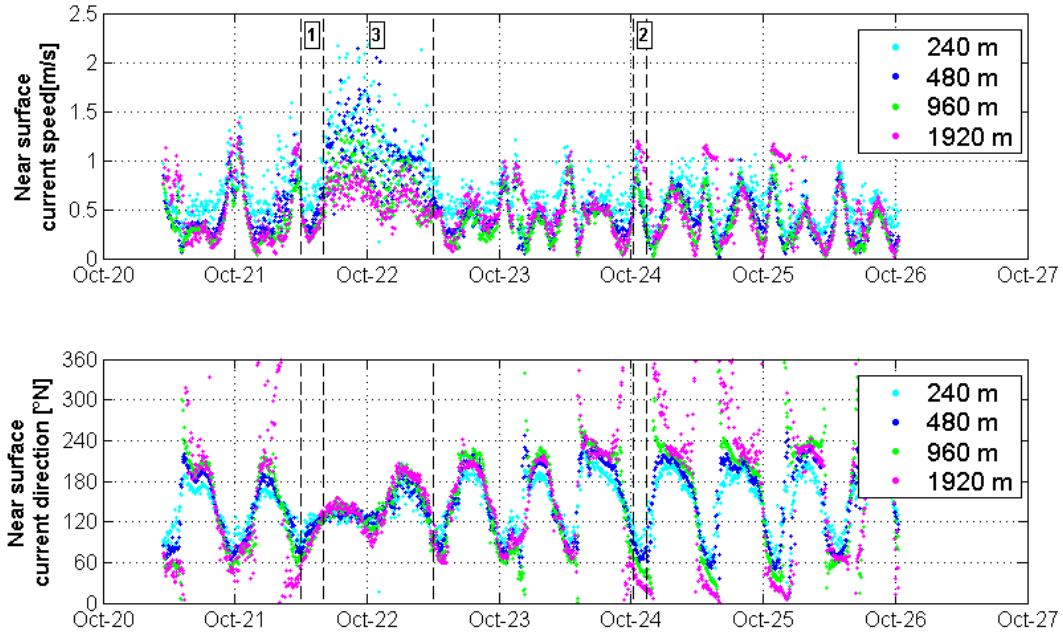

Figure 4.13: XMFit current estimates at location of ADCP E for cube sizes of 240, 480, 960 and 1920 m.

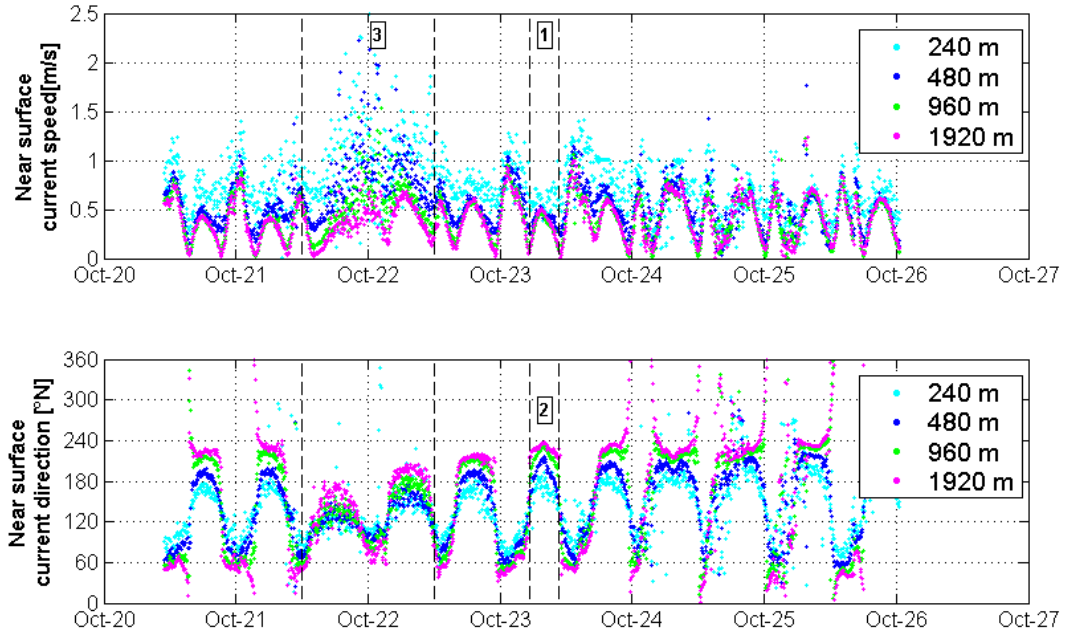

Figure 4.14: XMFit current estimates at location of ADCP F for cube sizes of 240, 480, 960 and 1920 m.

Figure 4.13 also explains why the flood current estimates of XMFit with a cube size of 1920 m are less accurate: sudden 'spikes' in magnitude occur, indicated by a (2). The (2) in the bottom plots of both figures indicate that the current direction is extremely sensitive to the cube size, both during (maximum) ebb and flood currents.

Finally, it is observed that for cube sizes of 960 m and 1920 m, the scatter in current magnitude is considerably smaller as for a cube size of 240 m and 480 m which is indicated by a (3) in both figures. However, since the ADCP signal during the storm showed also considerable scatter (figures 4.5 and 4.6), it is evident that the current estimates for all cube sizes are relatively inaccurate for this period.

However, the relation as shown in figure 4.12 is specified by only four points (with irregular intervals) which is insufficient to give detailed information on the properties of the relation. To obtain that information, the accuracy of XMFit time series for four intermediate cube sizes is tested. The accuracy values for these intermediate cube sizes are added to the relation (figure 4.15).

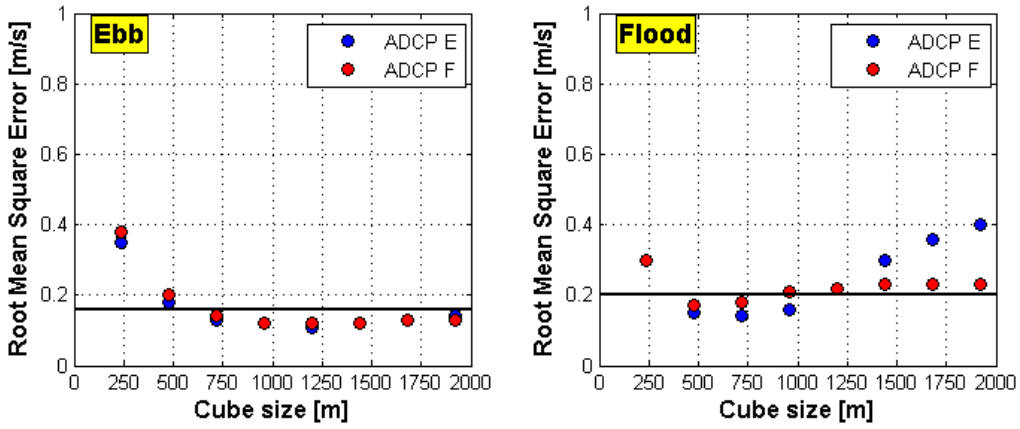

Figure 4.15: Refined relation between Root Mean Square Error and XMFit cube size during non-storm conditions

The added points to the relation confirm that the relation between accuracy and cube sizes for ebb currents indeed follows a curve that is close to a hyperbola with an asymptote for an RMSE of 0.16 m/s. This relation is fairly equal for the locations of both ADCP. For flood currents the relation differs between both ADCP. The extra cube sizes confirm that for ADCP F, the accuracy of XMFit follows an asymptote of 0.2 m/s. At ADCP E, the parabola is now better defined and it is observed that the cube size that gives most accurate currents has a size of 720 m. The increase in RMSE is visible from a cube size of 1460 m, for which the spikes become visible in the current time series.

4.3.4. CONCLUSIONS

In this chapter it was observed that for a cube size of 960 m, XMFit is able to extract tidal flow currents with expected accuracy (0.15-0.2 m/s). There are weak indications that flood currents are underestimated and ebb currents are overestimated. The relation between cube size and measurement accuracy of normal tidal currents was found to be approximated by a hyperbola for both ebb and flood currents. Significant deviations were observed for a cube size of 240 m, which is expected to be linked to little data and a coarse spectral resolution. This is subject of discussion in section 6.1.2 and 6.2.2. These spikes for the flood currents at the location of ADCP E are observed in combination with image spectra that do not have the form of a dispersion shell. Since ADCP E is in the complex near-shore area, those distorted spectra are believed to be directly linked to non-uniform properties of wave propagation, depth and currents within area covered by the computational cube. This is discussed in more detail in section 6.2.1.

The correspondence between results of XMFit and in-situ current measurements showed to be significantly lower during storm conditions. The scatter plots showed that this is mainly due to differences in cross-shore direction. It is hypothesized that this is caused by a combination of two factors. The first one is the addition of the average Stokes drift of the complete wave field, which is only a very rough approximation of the actually occurring Stokes drift. A calculation of the Stokes drift contribution for each individual wave component may yield a lot more accurate results. The second factor may be rain and fog that was observed on raw radar images during a short time intervals within the storm period. Rain and fog have a direct negative influence on the usability of the radar image (chapter 2).

The results found in this section are valid for two single locations in the radar domain. In the next chapter the analysis is extended to output grid points at various locations in space. XMFit current estimates for the same cube sizes will be compared with in-situ drifter current measurements at locations along drifter trajectories for both ebb and flood currents. It can then be assessed if the results found in this section are generally applicable or location dependent.

5

SPATIAL VALIDATION

The point validation showed that the relation between cube size and RMSE may be approximated by a hyperbola, where the results of cubes > 240 m follow an asymptote. In this chapter, a spatial validation along drifter trajectories is performed to verify if the results of the point validation are general conclusions for the Sand Engine radar domain or only valid for the locations of both ADCP. Consistency between results of (pseudo-Lagrangian) point validation and (Lagrangian) drifter validation will contribute to improved understanding of radar currents being Eulerian or Lagrangian. In addition, the results of a spatial validation do provide more insight in the relation between current accuracy and location in the radar domain. The results from the point validation show high correlation between radar- and pseudo-Lagrangian in-situ currents. It is therefore expected that the accuracies of radar currents compared to Lagrangian drifter measurements is higher. Furthermore, it is expected that non-uniformity of wave propagation, depth and currents in the computational cube has repercussions for the current estimates. This is especially expected for the near shore region, where the application of depth-inversion is questionable from a theoretical point of view. In this spatial validation, the current estimates of XMFit for cube sizes of 240 m, 480 m, 960 m and 1920 m are compared with in-situ drifter current measurements at a dynamic grid that moves along the drifter trajectory.

This chapter starts with the presentation of the selected drifter data for validation of XMFit current estimates. It is followed by a detailed explanation of the dynamic grid approach in section 5.2. Section 5.3 presents the results of the validation.

5.1. DRIFTER MEASUREMENTS

The current obtained with XMFit is compared to in-situ drifter current measurements along drifter trajectories. Again, data from the directional wave buoy (reference is made to section 4.1) is used as metric to assess if the correct spectral data is fitted by XMFit to estimate the current. In this paragraph, only the drifter data is described in more detail.

Current measurements from 15 deployed drifters are used for direct comparison with the radar current. Measurements are collected in the context of the MegaPEX experiment with GPS-tracked surf zone drifters. The drifters are free floating buoys equipped with Locosys GPS GT-31 loggers for which a sampling frequency of 1 Hz has been set. The logger reports position and velocity. Velocities are estimated based on the Doppler shift of the GPS signal. The drifters, designed for measuring surf zone currents, consist of a hollow PVC tube of 0.4 m length with a bottom plate of 0.35 m diameter and four fins that increase the drag of the drifter body. A stabilizing weight is mounted to the bottom plate to ensure stability of the drifter under wave attack and prevents the drifter from surfing on the roller of breaking waves (Zeelenberg (2015)). On top of the PVC tube, a watertight Otterbox is placed to provide housing for the GPS logger and other electronics. The Otterbox is placed horizontal to be able to pick up a sufficiently strong GPS signal during measurements, even under regular tilting (Zeelenberg (2015)). Logged data was stored on a removable memory card and was transferred to a computer after final retrieval.

Reported accuracy of drifter current measurements vary between 1-5 cm/s (Ohlmann et al. (2007)). Spe-

cific accuracy for the drifter measurements during MegaPEX is not recorded. Therefore it is assumed the drifter measurements are as accurate as the general figure indicates. This accuracy is sufficient to be convinced of drifter current measurements being appropriate ground truth to validate near-surface radar currents with. Drifter current measurements were filtered for unrealistic values, for more details see Zeelenberg (2015). Drifter measurements are made in the UTC time zone and thus do not need pre-processing before comparing to XMFit radar currents (chapter 3).

Multiple drifter deployment sessions were performed, from which two sessions are selected: the session on October 17^{th} (14:30 UTC - 16:35 UTC) during ebb currents and October 18^{th} (9:20 UTC - 11:30 UTC) during flood currents. The specific deployment sessions for ebb and flood are selected based on the wide spatial extent of the drifter measurements. Both drifter sessions included the release of 10 -15 drifters. Within each drifter deployment session, drifters were retrieved and released multiple times by jet-ski when floated outside the area of interest or floating ashore. For further details regarding drifter deployment, reference is made to Zeelenberg (2015). The drifter patterns for ebb and flood deployment are shown in the lower panels of figure 5.1. The positions of the drifter in time are color-coded. Blue means the start of the session, while orange or red indicates the end of the drifter deployment session.

The upper panel of the figure shows the drifter deployment within the tidal cycle (measured by ADCP). Positive alongshore velocities mean flood currents in northeast direction (section 4.3). The drifters released during the ebb deployment of 17-10 measure currents around the moment of maximum ebb velocities. The drifters were consistently positioned relatively close to the shore during this deployment. Three characteristic patterns are distinguished (see lower left panel figure 5.1):

- Alongshore parallel southwest movement during full drifter deployment session
- Clockwise circulation for drifters just south of the tip of the Sand Engine
- Alongshore southeast or northwest movement in the surf zone

The drifters released during the flood deployment session on October 18^{th} measure flood currents in the period between the moment of maximum flood velocities and high water slack (upper panel figure 5.1). There is only a single spatial pattern observed for this deployment session: northeast movement parallel to the coastline. The majority of the released drifters followed a trajectory northeastward for the full duration of the session. A few drifters were repetitively picked up when leaving the surf zone and re-dropped near the tip of the Sand Engine.

5.2. DYNAMIC GRID APPROACH

Remotely-sensed radar-derived near-surface currents have to be compared to in-situ drifter measurements on an equal spatial and temporal scale (Ohlmann et al. (2007)). This implies that drifter data with high temporal and spatial resolution has to be averaged in time and space. The method of Ohlmann et al. (2007) was specifically designed to meet this requirement. Their method implies that drifters are repetitively deployed within a fixed, predefined square in the radar domain for a time period equal to the time scale of the radar current. Besides, this fixed square is used as computational cube to estimate the radar current. This directly allows for comparison on the same temporal and spatial scales.

However, the drifter data used in this study was obtained with the main purpose to study tidal flow separation at the lee side of a nourishment. As a consequence, the replacement of the drifters was not based on the spatial extent of the computational cube: drifter movement is not confined by the boundaries of a fixed grid cell. Instead, drifters traveled freely through the radar domain during their deployment. The fixed grid method used by Ohlmann et al. (2007) is therefore modified into a dynamic grid to still enable a comparison of drifter and X-band current data on the same temporal and spatial scale.

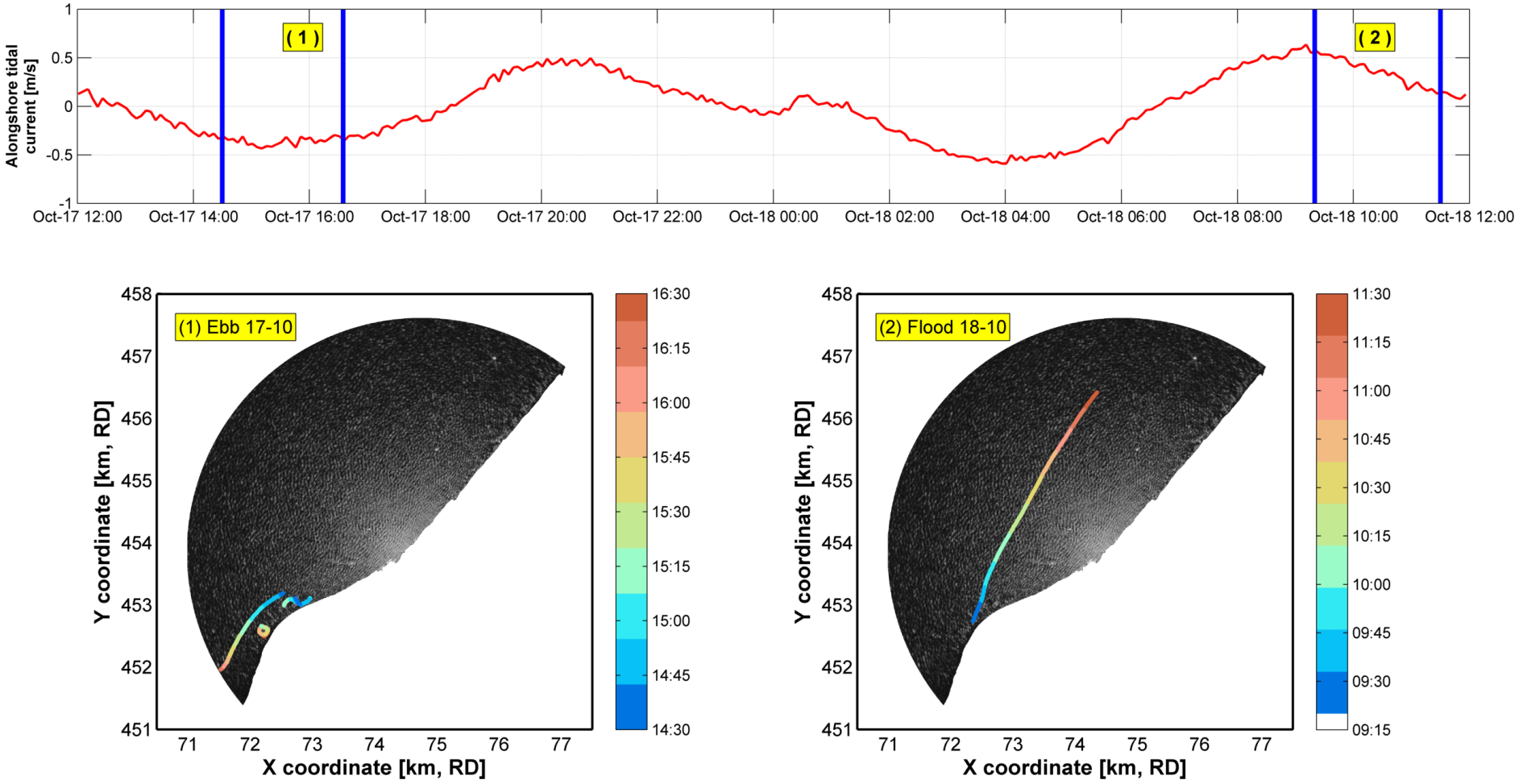

Figure 5.1: Spatial patterns observed in selected ebb and flood drifter deployments

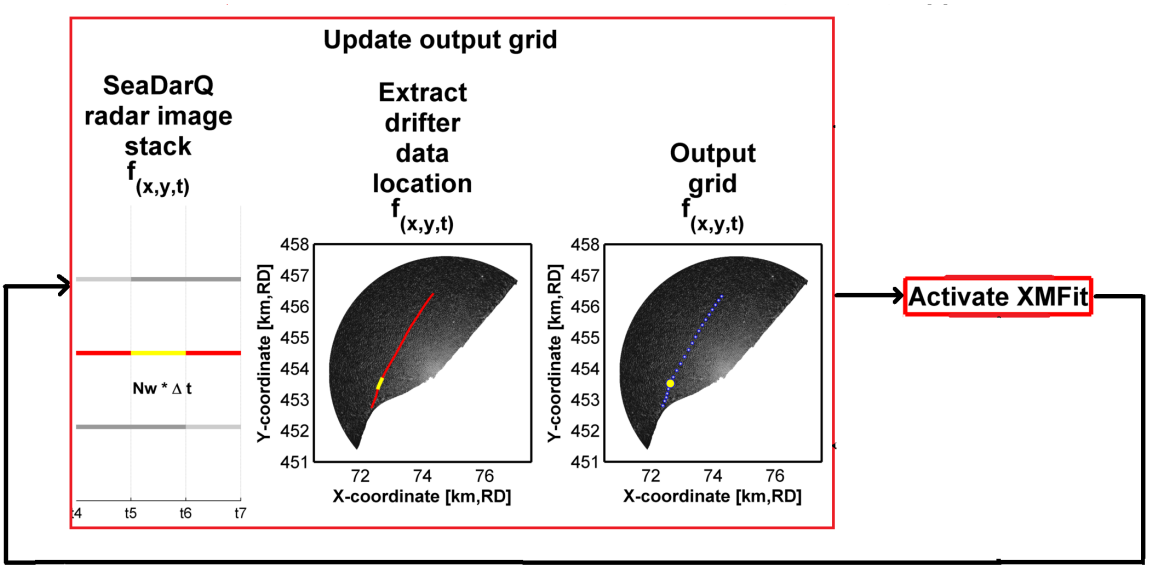

Figure 5.2: Dynamic grid approach: XMFit output grid is updated every time stack by calculating the centroid of the yellow drifter positions

The dynamic grid approach is based on movement of grid points in time along the drifter trajectory. This requires updating the output grid of XMFit every time step (figure 5.2). Consider an image stack with duration $N_\omega \Delta t$, indicated in yellow on the time line. Prior or subsequent image stacks are indicated in red. The positions of the drifter within the time period covered by the image stack $N_\omega \Delta t$ are selected. The locations of the drifter during the selected time period are shown in yellow in the middle plot. The centroid of the yellow drifter positions is the output grid point. This is indicated by the yellow dot in the third subplot. Subsequently, XMFit is activated to estimate the current for the grid point. Then the grid is updated for the next time stack according to the procedure described in the left red box in figure 5.2.

The dynamic grid thus enables a comparison of radar current measurements with in-situ current measurements along drifter trajectories. The next requirement is that both drifter and radar measurements shall represent average(d) measurements over the same temporal and spatial scale. It was decided to select the temporal and spatial scale of the radar current as comparison scales because the radar measurements have the longest timescale (6 min.) of both measurements. Thus, temporal and spatial averaging of high resolution drifter measurements is required. Figure 5.3 illustrates the averaging procedure of drifter measurements for two different cube sizes. The top plot shows that for every time stack t_x, drifter positions in a time interval $N\Delta t$ are selected (yellow). The positions of drifters in prior or successive time intervals are shown in red. The middle and bottom row illustrate the selection of drifter data for two different cube sizes in space.

The time scale of the radar current is normative in selecting drifter data that is spatially averaged. The positions of the drifter in the time interval defined by the radar image stack $N_\omega \Delta t$ are selected, indicated in yellow. The shift of the yellow drifter positions for successive time stacks shows that the resulting grid is dynamic, according to the procedure in figure 5.2. **Yellow drifter positions within the area covered by the computational cube** are spatially averaged and represent ground truth. The plots for a cube size of 240 m show that the cube extent is smaller than the spatial extent of the yellow data. The cube size is the limiting factor in this case which limits the data that is spatially averaged. A cube size of 960 m is bigger than the spatial extent of the yellow data (figure 5.3). In this case, the spatial extent of the drifter data is the limiting factor. In case the cube size is equal to the spatial extent of the selected yellow drifter data (not shown in figure 5.3), spatial scales are equal. Note that the XMFit current is always extracted using the full area in the white box.

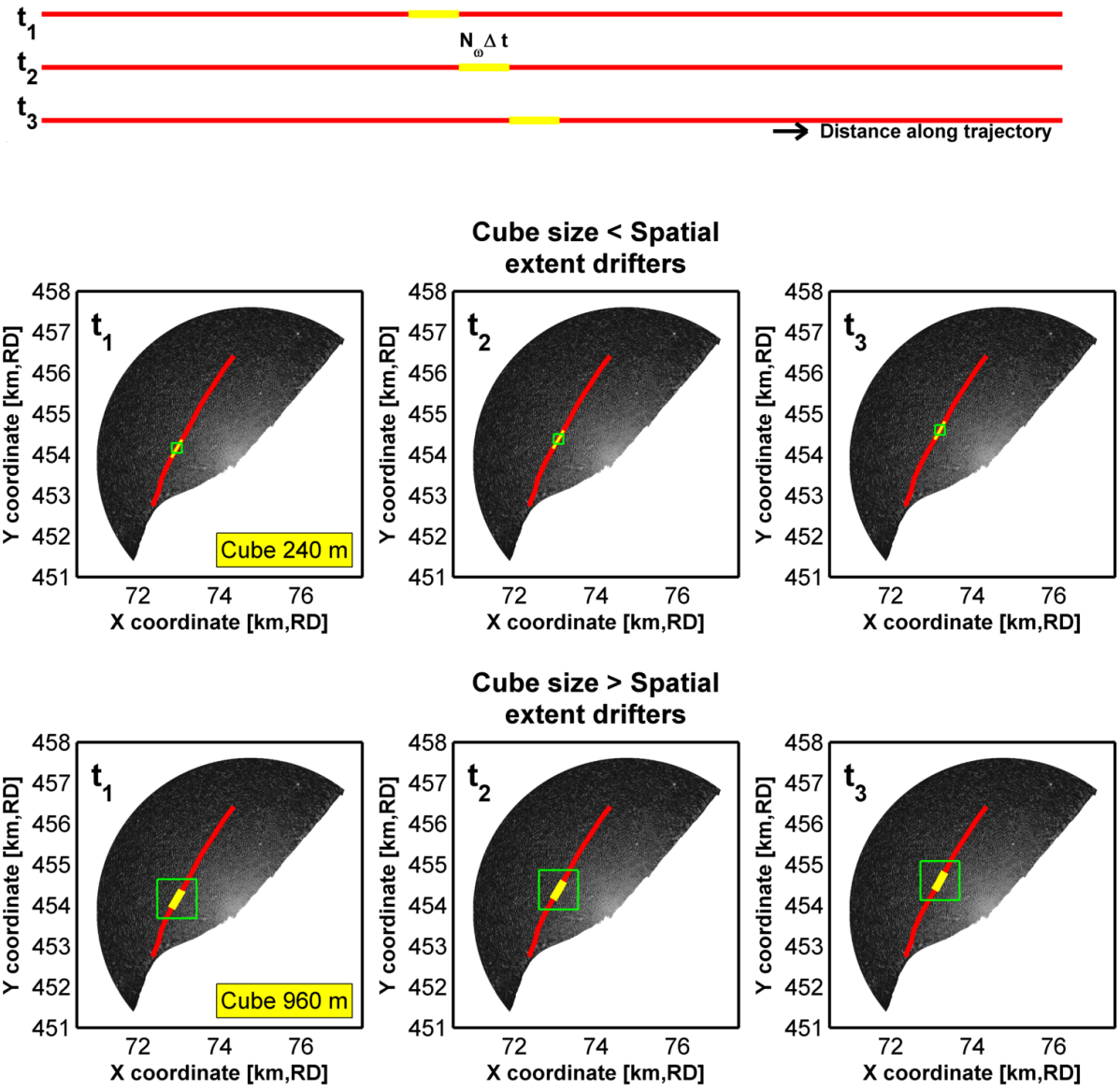

Figure 5.3: Measurements of drifter positions in the area covered by the computational cube are spatially averaged to obtain in-situ ground truth on the same spatial and temporal scale

5.3. RESULTS

The current estimates made by the XMFit algorithm for the selected ebb and flood drifter deployment are presented in this section. It is emphasized that the results are temporally limited to two relatively short periods of approximately 2 hours.

5.3.1. REPRESENTATIVE DRIFTER TRAJECTORY

The performance of XMFit along a representative trajectory is studied first. This allows for a relatively effortless recognition of the overall quality of the fit and spatial/temporal variations.

For the ebb deployment of October 17^{th}, three general drifter movement patterns were observed (section 5.1):

- Alongshore movement outside the surf zone after being released at the tip of the Sand Engine
- Rotating movement in an eddy in the surf zone
- East or west movement in the surf zone, relatively close to the shore

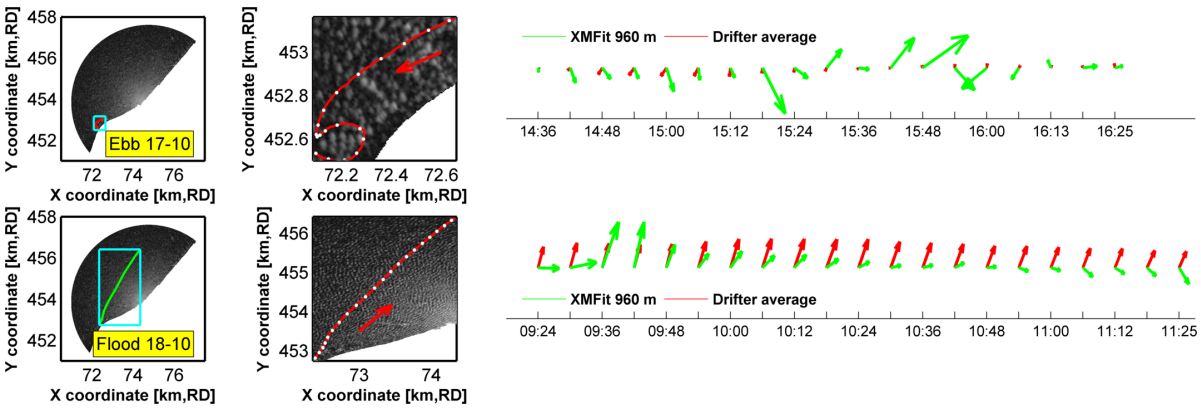

Figure 5.4: Direct comparison of XMFit and drifter currents along a representative ebb and flood drifter track

A trajectory was selected that followed both alongshore and rotating movement (figure 5.4, upper row, second panel). The trajectory starts at the tip of the Sand Engine, where the drifter is released. Its initial movement is southwest alongshore, indicated by the red arrow in the figure. From 15:30 on, the drifter follows the rotating movement in the eddy in the surf zone. Thus, the comparison along this representative track allows for assessment of the quality of XMFit current estimates of both alongshore ebb flow and small scale rotating flow. A representative flood drifter trajectory was selected that followed the characteristic alongshore movement over the full extent of the deployment period. The drifter is released near the tip of the Sand Engine (figure 5.4, bottom row, first and second panel) and steadily moves into northeast direction (indicated by the red arrow).

Similar to the point validation, the accuracy of radar currents is examined for a cube size of 960 m first. The results are shown in figure 5.4 for the ebb (upper panel) and flood drifter deployment (lower panel). Ebb currents are overestimated by XMFit (upper time line). Directional estimates are inaccurate. From 14:36 h - 15:06 h the drifter is moving alongshore. The results show that XMFit gives cross-shore flow instead of alongshore flow. From 15:12 h to the end of its deployment, the drifter follows rotating movement in a near-shore eddy. The temporally and spatially averaged drifter current in the eddy is near zero and reveals clockwise rotation. XMFit indicates large current magnitudes with no agreement in current direction, thus leading to inaccurate current estimates. This results show that XMFit is not able to recognize the alongshore ebb flow and eddy flow in the near-shore area.

The vector comparison for flood currents (bottom time line) shows overestimation of the current magnitude from 9:24:01 - 9:48:11. The current vectors are inconsistent compared to XMFit current estimates at later times. Flood currents are underestimated in XMFit from 9:54:14 until the end of its deployment. An offset in the angle is observed. The value of the offset varies over time and is between 15-90°. For flood currents, there is more consistence between current vectors.

5.3.2. XMFIT SPECTRAL ENERGY SELECTION

This section investigates the correspondence between wave parameters determined by XMFit and the deployed directional wave buoy during both drifter deployments. The comparison of wave parameters estimated by XMFit and measured by the wave buoy is added since it is a good metric to check if XMFit is fitting the correct spectral energy.

Figure 5.5 shows the direct time series comparison of two wave parameters. The upper panels show that the peak period is slightly underestimated by XMFit with 1-1.5 s. This was also observed for the ADCP and was expected to be related to the relative importance of the short waves in the fit. This is discussed more in detail in chapter 6.3.2. An unrealistic high peak period is observed for 15:42:51 h during the ebb deployment which implies that for this time stack the long wave energy is dominant in the fit. The image spectrum for this time indeed confirms a cluster of points at lower frequencies. However, the frequency levels with the second and third highest energy content show that the short waves are still dominant in the fit. Therefore, confidence in XMFit fitting the right energy exists. The incidental peak may possibly be the result of an object in the radar domain that causes increased backscatter at low frequencies.

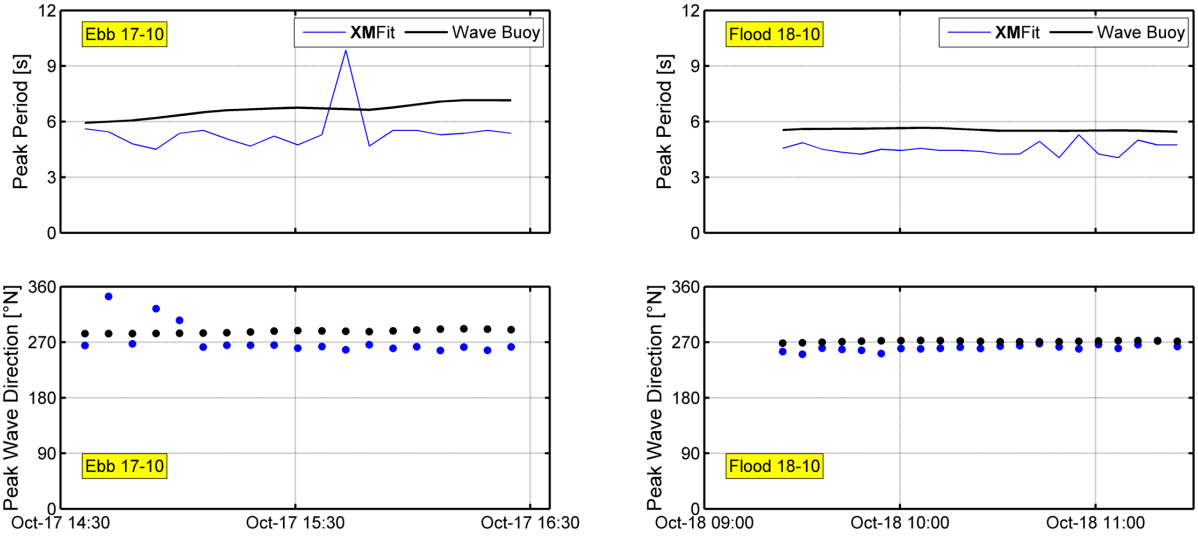

Figure 5.5: Direct comparison of wave parameters estimated by XMFit and the deployed wave buoy

The bottom panels of figure 5.5 indicate fairly good agreement in peak wave direction for both drifter deployments. This indicates proper selection of the spectral energy cutoff that filters noise and aliased spectral energy. The wave buoy comparison shows that the agreement is satisfactory to have confidence in the capabilities of the depth-inversion method to estimate the near-surface currents for these time periods.

5.3.3. THE INFLUENCE OF SPATIAL SCALE OF WAVE DISPERSION ANALYSIS

The validation results for XMFit with a cube size of 960 m showed that XMFit is able to recognize the alongshore drifter movement during flood. However, XMFit fails in recognizing alongshore ebb currents and eddy flow along drifter trajectories that were close to the shore. Here the results obtained with cube sizes of 240 m, 480 m and 1920 m are presented and compared to the results for a cube size of 960 m. First the current estimates along the representative trajectory are studied to recognize possible (spatial) patterns. It is directly followed by the identification of these general spatial patterns by involving all grid points of the deployment.

The ebb current time series along the representative drifter track are shown in figure 5.6. Note once more that the drifters were located in the surf zone and near the edge of the radar domain (upper left panel). The time series show that XMFit is not able to accurately estimate the in-situ current for all computational cube sizes considered here.

The scatter plots (figure 5.7) show that this finding holds for current estimates at grid points along all drifter trajectories of the ebb deployment. Each of the scatter plots contains the data from all grid points during the ebb drifter deployment. The current vectors for all output grid points are decomposed into the alongshore component and cross-shore component.

It is observed that both the alongshore and cross-shore component scatter plots form a vertical line. A vertical line in the scatter plot implies that the drifter velocity is relatively constant (in this case near zero), while XMFit is estimating currents that show a lot of variation. The accuracy of XMFit for the considered ebb currents is low, indicated by a relatively high RMSE-value. This is the case for all considered cube sizes.

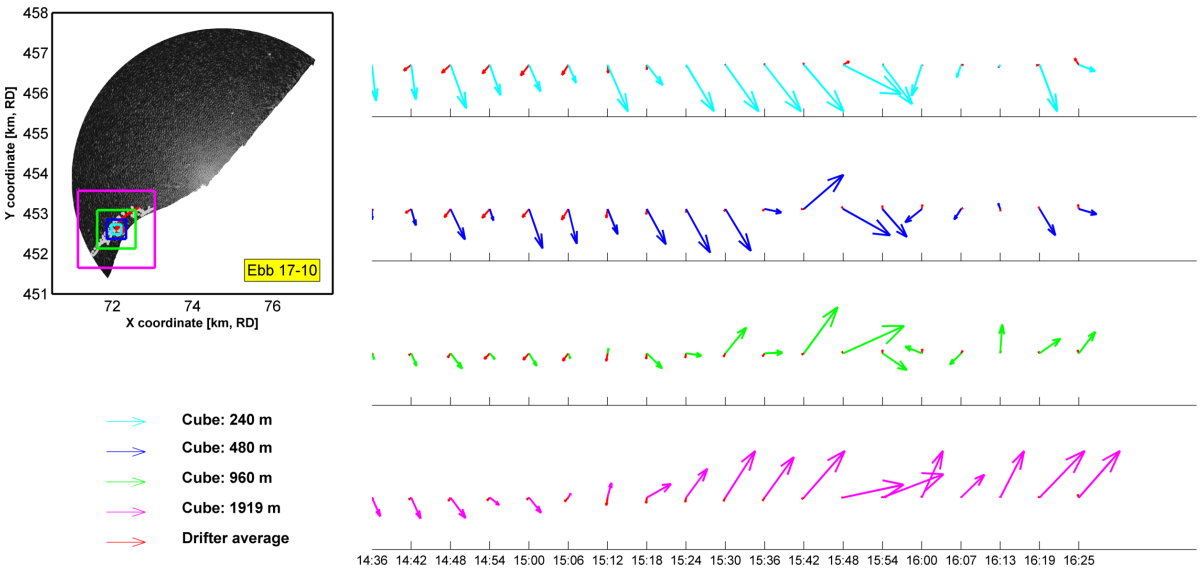

Figure 5.6: XMFit and drifter current series along representative drifter trajectory for the considered ebb deployment

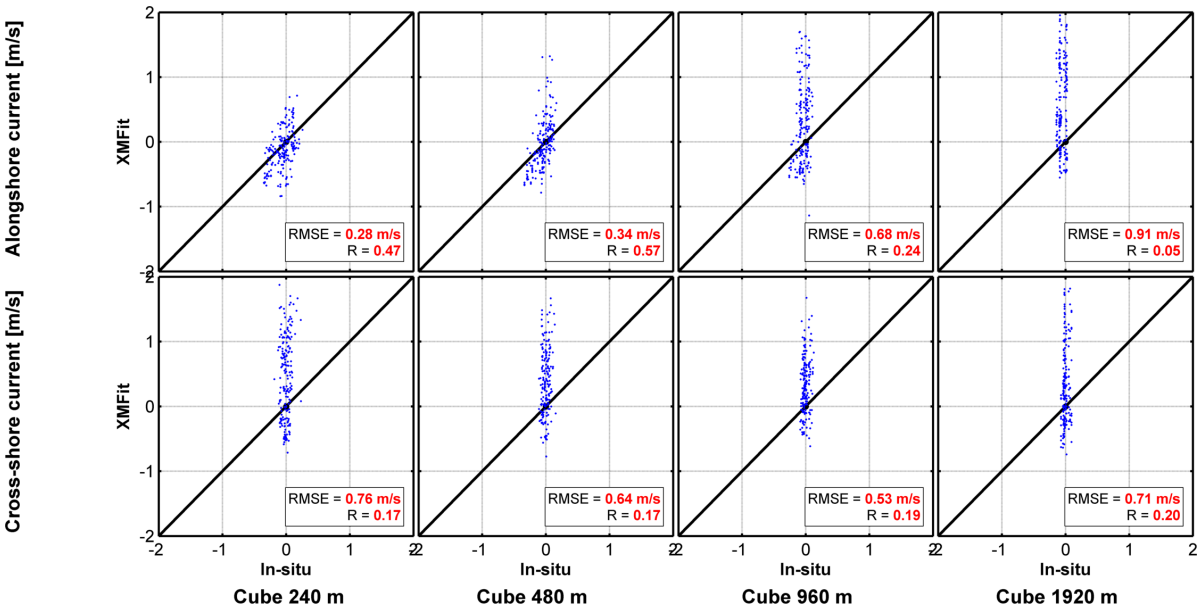

Figure 5.7: Scatter plots for alongshore and cross-shore velocities during ebb drifter deployment

The vector time series along the representative drifter track during the flood deployment is shown in figure 5.8. An irregular current series is obtained when using XMFit with a cube size of 240 m. XMFit current estimates do not align with measured drifter current vectors along the trajectory for this cube size. The figure shows that, similar to a cube size of 960 m, the current estimates of XMFit directly after the release in the surf zone are inaccurate for cube sizes of 480 m and 1920 m as well (A). When the output grid points are sufficiently away from the shore, XMFit results for cube sizes of 480 m, 960 m and 1920 m show up to have a consistently smaller current magnitude and an offset in direction(B). Note that both the magnitude and offset in direction decreases for bigger cubes. In addition, a cube of 480 results in inaccurate current estimates near the end of its deployment time (C). Those findings seem to represent a general spatial pattern and will therefore be considered in more detail.

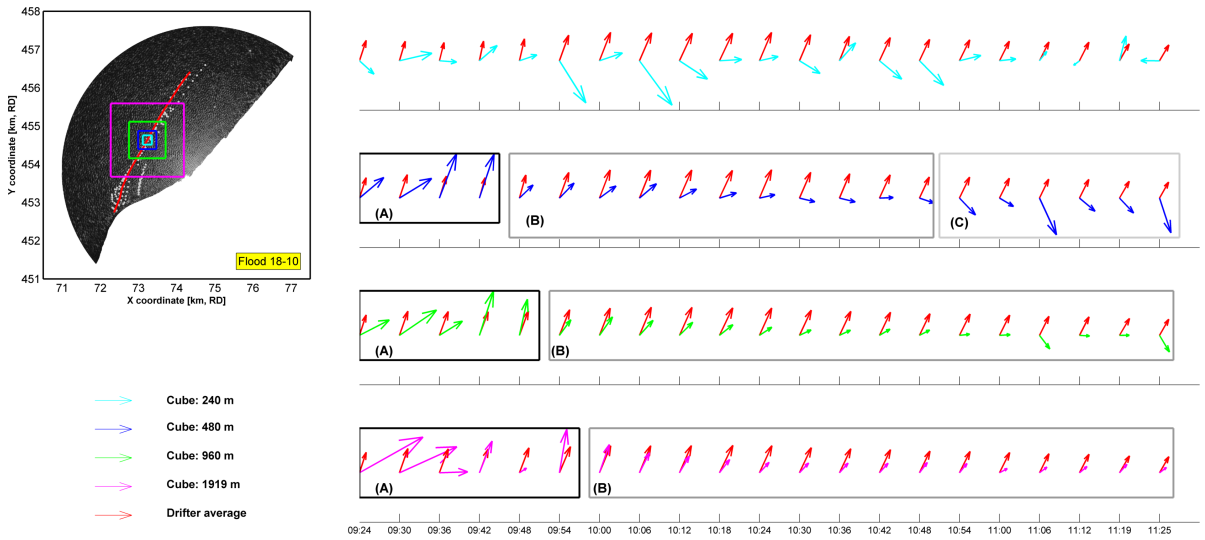

Figure 5.8: XMFit and drifter current series along representative drifter trajectory for the considered flood deployment

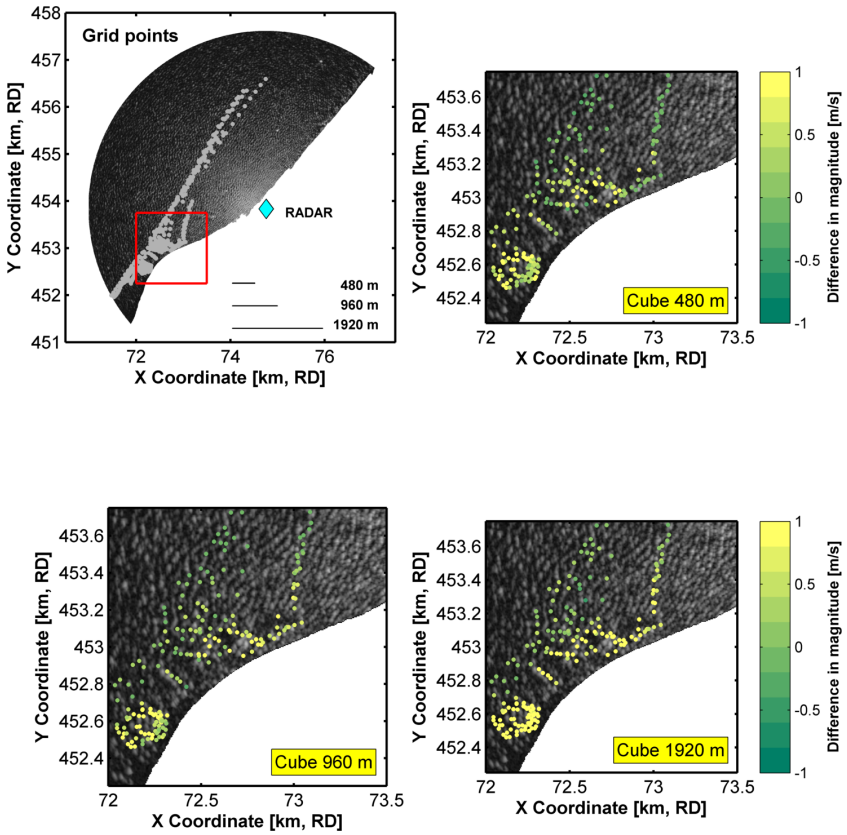

Figure 5.9: Overestimation of in-situ current magnitude by XMFit for grid points within the first 500 m from the coastline

(A) Near shore current estimates

The direct vector comparison of ebb currents along the representative track showed inaccurate results for all cube sizes. This representative track is located very close to the shore. In addition, XMFit estimates of flood currents are inaccurate directly after release (figure 5.8). This might confirm the hypothesis that the quality of XMFit current estimates in the surf zone is poor due to non-linear wave effects caused by non-uniform bathymetry, small scale complex flows or wave transformation (refraction, shoaling). Figure 5.9 illustrates the results for all grid points in the near shore. Grid points from both the ebb and flood drifter deployment are included. The upper left plot shows all grid points (gray) for both ebb and flood drifter deployment sessions. The current estimates in the area in the red box are inspected more closely. The upper right and both bottom panels show the difference in magnitude between radar current and drifter-averaged currents. Yellow means overestimation while green means (slight) underestimation. From figure 5.9 it is evident that currents in the first 500 m from the coastline are estimated with significant less accuracy.

(B) Underestimation and offset

The second pattern that is observed in figure 5.8 is the consistent underestimation of the magnitude and an offset in direction. Direct current time series comparison along the representative track showed that these two phenomena were present in XMFit results for cube sizes of 480 m, 960 m and 1920 m. Both current magnitude and offset in direction showed up to decrease with increasing cube size.

Figure 5.10 considers the XMFit results in the center of the radar domain, where these patterns are typically observed. The red box marks the area for which the grid point results are magnified in the other panels. Note that this box exclusively covers the flood measurements outside the near shore. The bottom left panel of the figure shows that the (slight) underestimation in current magnitude is a general pattern. The panels at the right of the figure show the difference in direction for the grid points in the red box for cube sizes of 480 m, 960 m and 1920 m respectively. Red and orange indicate a small deviation in angle, while green, blue and purple indicate a high deviation in angle. The offset in direction is also a general pattern, an effect that tends to decrease with increasing cube size.

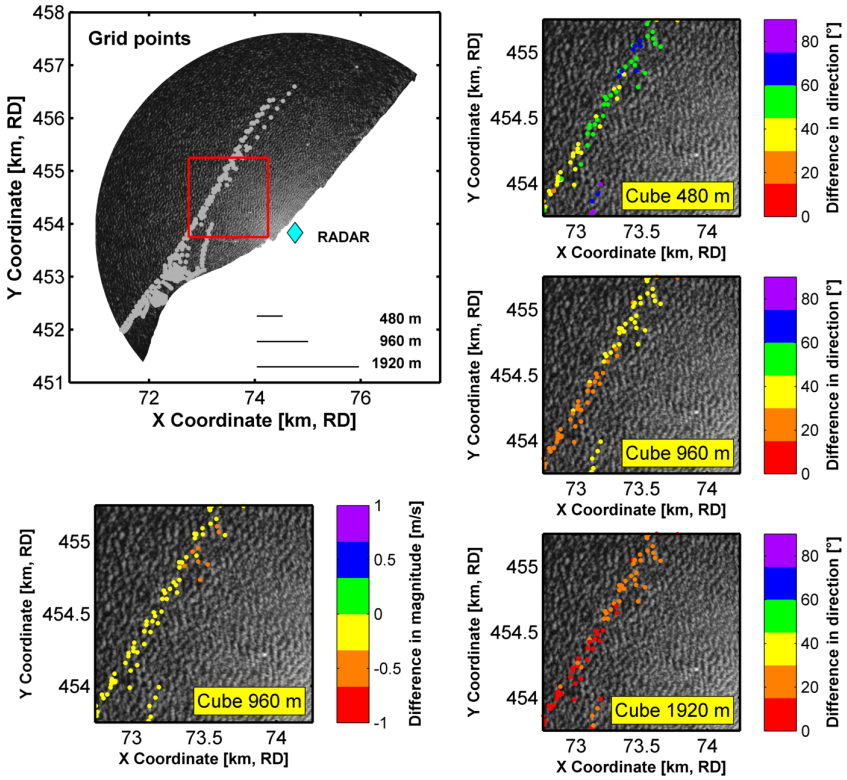

Figure 5.10: Underestimation of current magnitude and offset in current direction for grid points outside the surf zone

(C) Inconsistent currents near edge of domain

Finally, it was observed in the vector comparison along the representative trajectory that a cube size of 480 m resulted in irregular current estimates near the end of its deployment. The behavior is not in line with the current vectors in the center of the radar domain. Figure 5.11 shows the difference in magnitude between drifter-averaged and XMFit currents for the grid points near the edge of the domain. Again, the upper right and bottom panels are a zoom-in of the grid points in the red box (upper left panel). For cube sizes of 960 m and 1920 m, a consistent pattern of slight underestimation of in-situ current magnitudes by XMFit is observed. The results for a cube size of 480 m reveal relatively high variation in the results. A mixed pattern of slight underestimation and slight overestimation is observed. For cube sizes of 960 m and 1920 m this effect is almost non-existing. It is hypothesized that this effect is caused by the filtering process in XMFit. This is discussed more extensively in chapter 6.3.

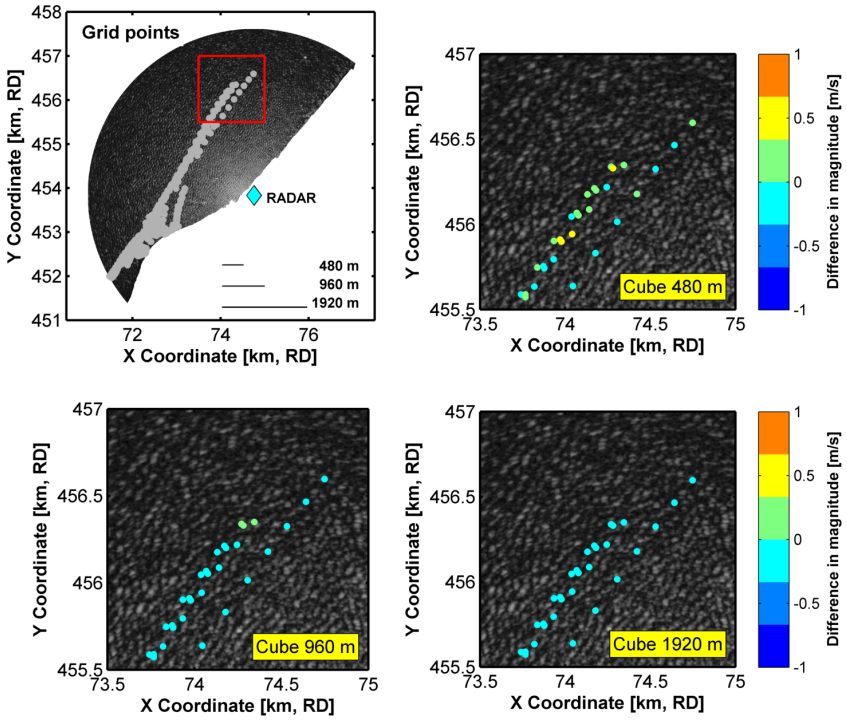

Figure 5.11: Inconsistencies in current estimates for a cube of 480 m near the edge of the radar domain

Figure 5.9 thus confirmed that XMFit overestimates in-situ currents at grid points within the first 500 m from the shore. Those have low accuracy, which is comparable to the RMSE values for the ebb deployment. In the following, the grid points in the first 500 m from the coastline are excluded from the analysis since they do not reflect how well XMFit is able to extract alongshore movement under flood conditions.

The scatter plots for the flood deployment are shown in figure 5.12. The in-situ flood current does more or less align with the alongshore direction. Current data for all output grid points outside the surf zone are decomposed into their alongshore- and cross-shore component. The results along the representative track showed that a cube size of 240 m resulted in irregular and inaccurate current estimates. This is confirmed in the scatter plots by big spread in alongshore direction and a vertical stripe in cross-shore direction. When the points form a vertical line, it means that XMFit is giving a lot of variation in current estimates, while the in-situ drifter velocities are fairly constant. A vertical stripe thus implies that XMFit has difficulties to identify this constant velocity. In addition, figures 5.8 and 5.12 revealed the underestimation and offset in direction for cube sizes of 480 m, 960 m and 1920 m. The alongshore component for those cube sizes is consistently underestimated (upper row of figures). The decreasing offset in direction for bigger cubes is directly observed in the scatter plot since the data in the scatter plots of the cross-shore current is moving toward the origin (compare second to fourth plot of bottom row). Zero cross-shore flow is what is expected in case of purely alongshore flow. The fitting statistics indicate that for increasing cube size, both alongshore and cross-shore flow is estimated more accurately.

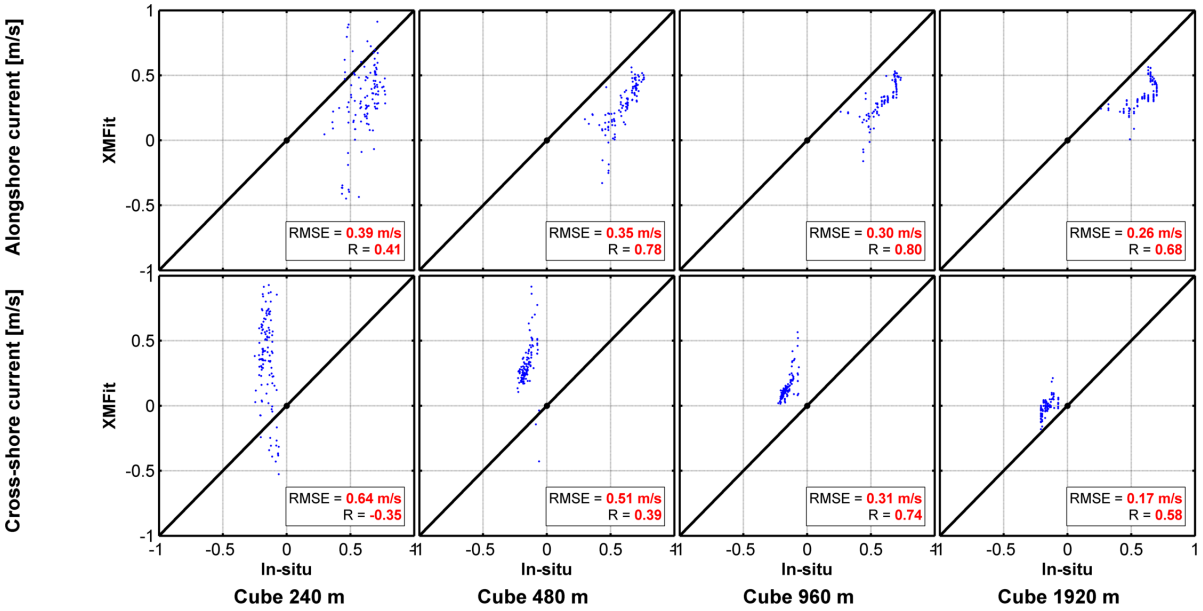

Figure 5.12: Scatter plots for alongshore and cross-shore velocities during flood currents outside the near-shore area

5.3.4. CONCLUSIONS

Figure 5.13 summarizes the findings of the comparison of radar and in-situ drifter current measurements. The validation of ebb currents showed that XMFit is not able to accurately estimate the in-situ current. The left panel of figure 5.13 shows that for all cube sizes, the validation results for either one or both current components is characterized by a high RMSE. The same is observed for flood currents near the release point in the near-shore, that have a high RMSE as well. It is expected that non-linear wave effects in the area overlaid by the computational cube cause this inaccuracy. This is further elaborated in section 6.2.1.

The flood measurements provide a better indication of the general patterns since the drifter trajectories for this deployment are not limited to the surf zone. These measurements will therefore not be influenced by near-shore effects. The XMFit results for a cube size of 240 m are inaccurate in both its cross-shore and alongshore estimates (right panel figure 5.13). The inaccurate results for a cube size of 240 m are in line with the worse results for a cube of 240 m found in the point validation. A coarse spectral resolution and a low number of regression coordinates were found in the spectra, which is a likely reason for the inaccuracy of XMFit when using this cube size. This is discussed more extensively in section 6.2.2. In general, for cube sizes of 480 m, 960 m and 1920 m flood current magnitudes are underestimated by XMFit and have an offset in direction. The offset was found to decrease with increasing cube size. The right panel of figure 5.13 clearly shows that accuracy increases for increasing cube size. The differences between the results for the different cube sizes are linked to the sensitivity to the amount and precision of the spectral data, which is discussed in more detail in section 6.2.2. This also links to the extreme sensitivity of XMFit currents to the filtering parameters (section 6.3). A hyperbolic relation is observed. The values of the RMSE are higher than those found in the point validation. This does not follow the expectations raised after the point validation.

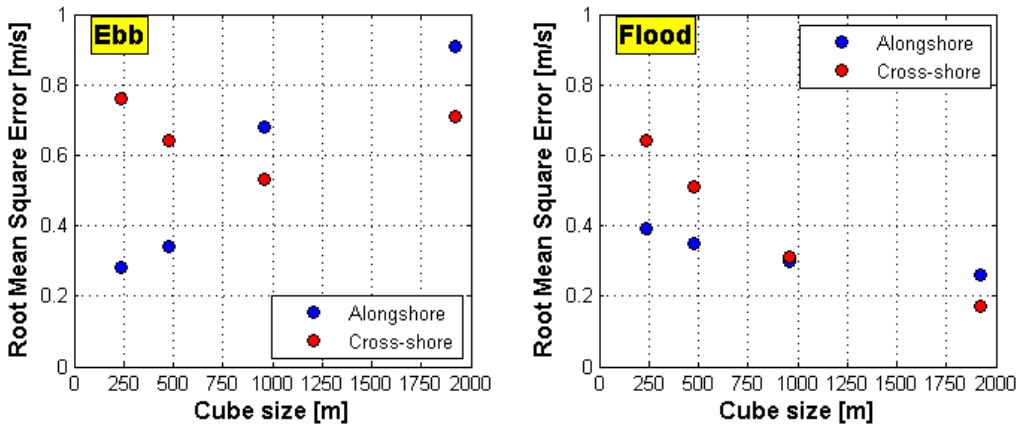

Figure 5.13: Relation between Root Mean Square Error and XMFit cube size for ebb and flood deployments

6

DISCUSSION

This aim of this research is to find a relation between the spatial scale of wave dispersion analysis and the accuracy of the radar current. Since there is an ongoing debate about radar currents being Eulerian or Lagrangian, radar-derived currents are compared to corrected (Eulerian) ADCP and Lagrangian drifter ground truth. This chapter starts with a discussion of the results of the point validation with ADCP current measurements in section 6.1. The Eulerian ADCP ground-truth was corrected for the Stokes drift. It is important to reflect on how this assumption influenced the reported accuracy. This is discussed first. It is followed by a brief interpretation of the relation between XMFit measurement accuracy and *computational cube size*. In section 6.2, the interpretation of the spatial validation with Lagrangian drifter current measurements is described, in which the focus is on understanding the differences between cube sizes and the overestimation of surf-zone currents by XMFit. The point and spatial validation were carried out for different periods in time. The relation between accuracy and spatial scale of wave dispersion (*computational cube size*) is found to be hyperbolic for both cases. However, the RMSE values are considerably higher for the drifter validation period for flood currents. However, based on the results of the point validation we would expect the results of the drifter validation to be more accurate. In order to understand why this occurs, section 6.3 compares ADCP and drifter for the same time period and explains the differences by examining the filtering process.

6.1. POINT VALIDATION

6.1.1. THE IMPACT OF STOKES DRIFT CORRECTION ON EULERIAN ADCP MEASUREMENTS

In this research a modified version of the commonly applied ADCP validation method was developed. The data analysis of the ADCP measurements revealed that the measurement of the shallowest bin was located 1-1.5 m below the water surface for both ADCP. The radar-derived current measurement represents a near-surface current and depends amongst others on this layer of the water column. There is no shear in the velocity profiles and thus a comparison between ADCP and radar current over its effective depth is not feasible.

The Eulerian ADCP measurements of the shallowest bin were interpreted to represent the mean flow in the water column. However, since the location of the shallowest bin is 1-1.5 m below the water surface, the specific near-surface process Stokes drift is fully missed in the Eulerian ADCP measurements. The mean onshore mass displacement represents the dominant near-surface coastal process in shallow water during storm conditions. It was expected that including the Stokes drift in Eulerian ADCP measurements may increase the accuracy for a single point location significantly, since a storm event ($H_s > 2m$) in the considered time period is present. Therefore, in this thesis the pseudo-Lagrangian ADCP current was selected as ground truth. Pseudo-Lagrangian currents were obtained by vectorial summation of the mean surface Stokes drift and the Eulerian ADCP current of the shallowest bin. As a result, pseudo-Lagrangian ADCP ground truth includes both mean bulk flow and specific near-surface processes. This is more close to the physical quantity that a radar measures. Therefore, it is expected that pseudo-Lagrangian currents have a better correlation with radar currents then Eulerian ground truth.

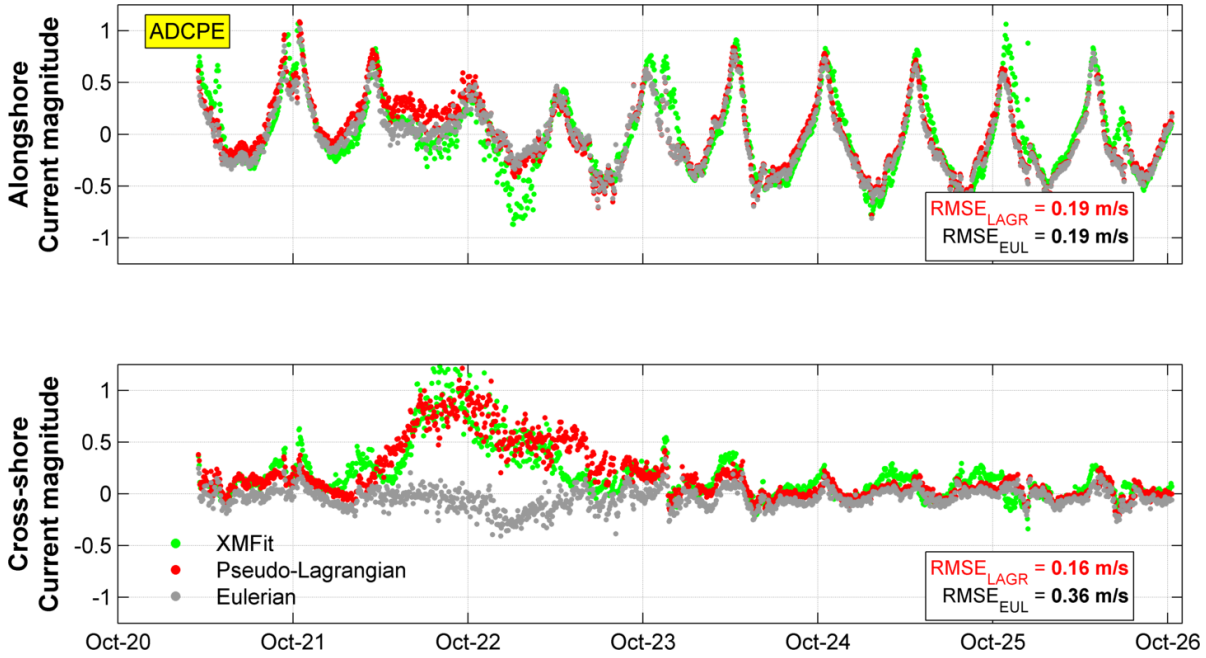

Figure 6.1: Direct comparison of XMFit with Eulerian and pseudo-Lagrangian ground truth for the alongshore and cross-shore components, ADCP E

The impact of Stokes drift is illustrated in figure 6.1 and 6.2. Figure 6.1 shows the current time series for ADCP E, splitted in its alongshore component (upper panel) and cross-shore component (bottom panel). A computational cube of 960 m is used to generate the XMFit time series of the current. Figure 6.2 is constructed identical to figure 6.1 but shows the results for ADCP F.

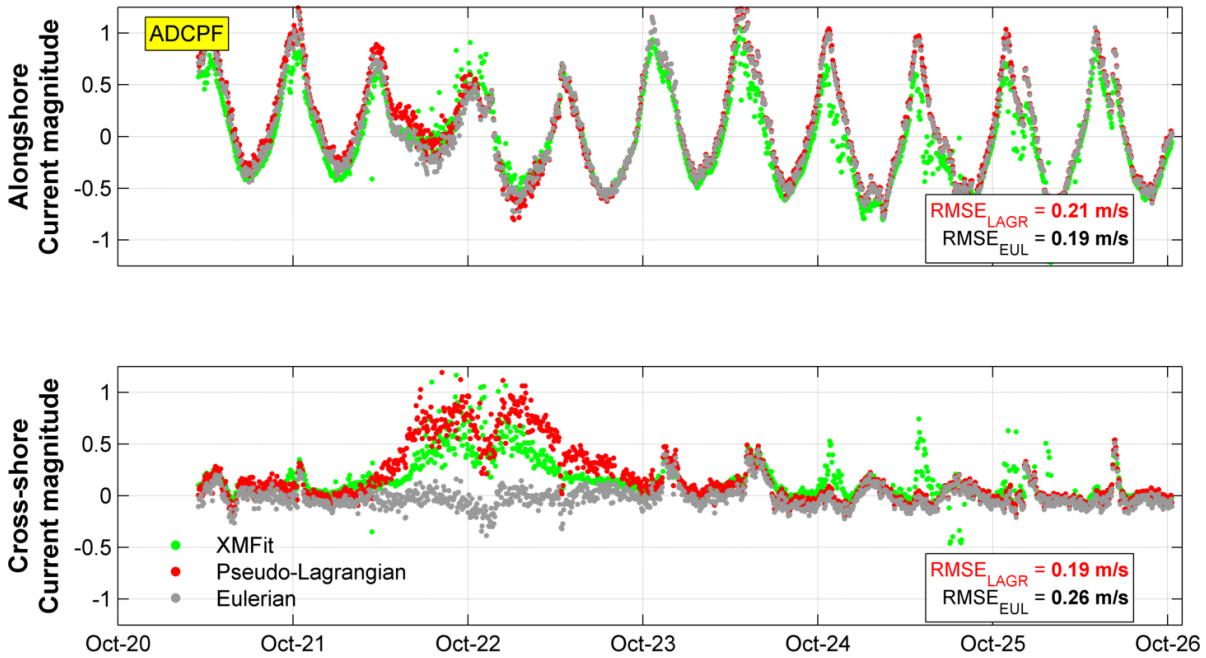

Figure 6.2: Direct comparison of XMFit with Eulerian and pseudo-Lagrangian ground truth for the alongshore and cross-shore components, ADCP F

Both pseudo-Lagrangian and Eulerian ground truth show alignment with XMFit for the alongshore component, except during a part of the storm (October 21^{st} 12.00 h - October 22 nd 0.00 h). The difference of the Stokes drift on the correlation between XMFit and in-situ ground truth is striking when the cross-shore component of the current is considered. XMFit shows a significant onshore directed flow during the storm. However, the purely Eulerian ADCP ground truth shows almost negligible cross-shore flow. This reveals the importance of the Stokes drift velocity component. Waves arrive approximately perpendicular to the shore for a surf-zone grid point: the Stokes drift velocity is onshore directed. The lower panels of figures 6.1 and 6.2 clearly show high agreement in cross-shore flow if XMFit is compared to pseudo-Lagrangian ADCP ground truth. These impressive improvement in the results for the pseudo-Lagrangian ground-truth that including the Stokes drift is a key factor for high accuracy during the storm period.

The impressive improvement in the cross-shore signal shows that pseudo-Lagrangian ADCP ground truth is a better alternative to validate X-band radar currents then purely Eulerian ADCP current measurements. This is confirmed when considering current direction. Figure 6.3 shows the current vector time series for ADCP E, splitted in its magnitude (upper panel) and direction (bottom panel). Figure 6.4 illustrates the situation at ADCP F. Note that the same data is considered as in figures 6.1 and 6.2: only the representation of the vector is different.

The difference between Eulerian and pseudo-Lagrangian ADCP ground truth is most clearly illustrated for the current direction. Especially during the storm, differences between XMFit and Eulerian ADCP data is considerable. Directional estimates of the Eulerian ADCP measurements are scattered, while XMFit is consistently onshore directed (angle between 80 - 180 °). This supports the statement that Stokes drift is present in X-band radar currents. The pseudo-Lagrangian current direction shows good alignment with XMFit in current direction during the storm. Finally, the current magnitude time series at ADCP E (upper panel of figure 6.3) shows that the correlation is significantly improved for ADCP E when comparing XMFit to pseudo-Lagrangian currents. However, the current magnitude comparison for ADCP F (upper plot figure 6.4) shows that the RMSE slightly increased compared to the RMSE found by comparing XMFit to purely Eulerian ground truth. However, since the directions are estimated accurately, the formulation for the magnitude of the Stokes drift velocity is introducing unwanted errors. Therefore, the formulation of the Stokes drift magnitude should be subject of further research.

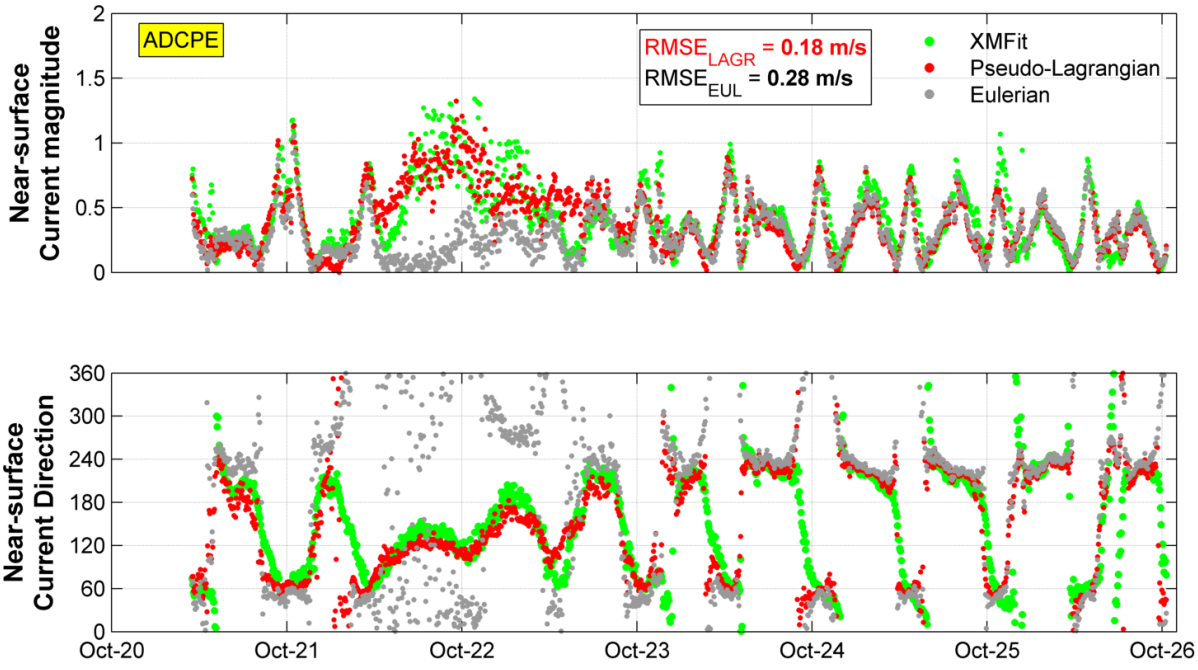

Figure 6.3: Direct comparison of XMFit with Eulerian and pseudo-Lagrangian ground truth, ADCP E

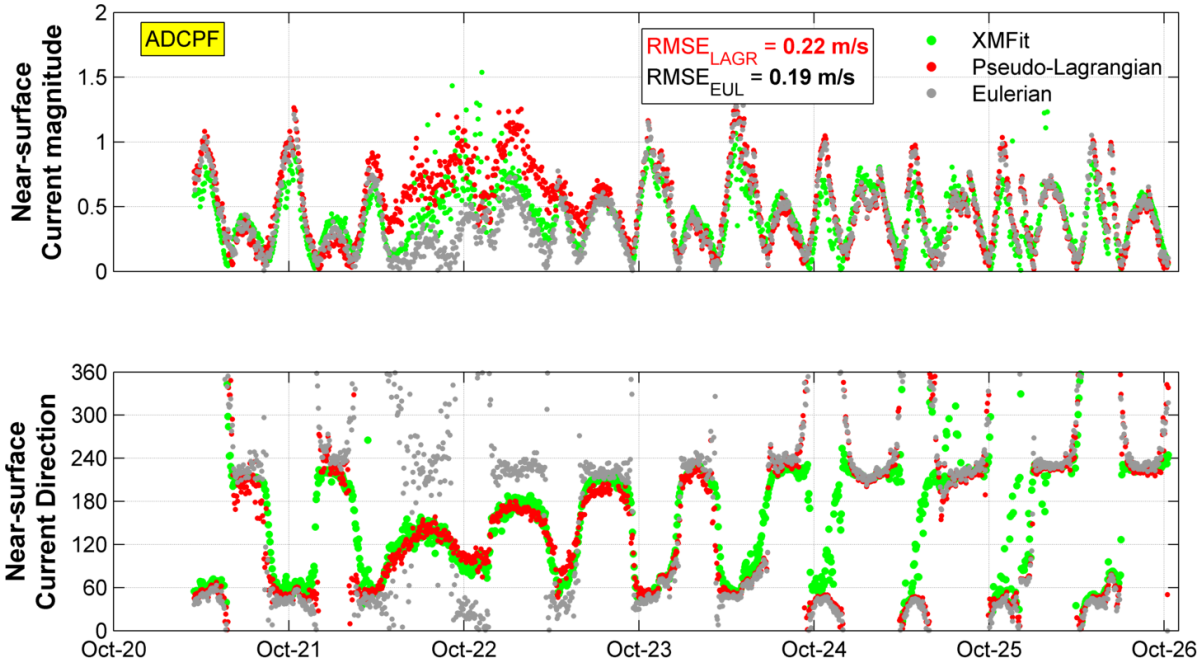

Figure 6.4: Direct comparison of XMFit with Eulerian and pseudo-Lagrangian ground truth, ADCP F

The proof in this section supports the research of Thompson et al. (1991) who demonstrated that X-band radar directly measures a mean surface drift. In this study the mean surface Stokes drift was used to obtain pseudo-Lagrangian ground truth. The available wave data did not allow a more in-depth investigation on the Stokes drift contribution. However, the results for ADCP F shows that XMFit and pseudo-Lagrangian are close but the exact magnitude of the Stokes drift velocity correction still needs improvement. Further research should be performed to find which part of the Stokes drift is important for X-band radar.

Based on the results found in this thesis, it is argued that X-band radar currents are Lagrangian measurements. This study period included storm conditions. It was shown that including Stokes drift has a significant influence on the accuracy during storm conditions. It is remarked that a counterintuitive method of showing the presence of Stokes drift in X-band radar images is used here. Intuitively, the in-situ data represents 'reality' and would never be subject to modification. However it is still a debate what the best validation procedure for radar-derived currents is: the suitability of the ground truth is unknown. Therefore, it is still uncertain how accuracy figures from other research should be interpreted. Their results should be interpreted with care. More attention should be paid to a detailed understanding of the exact role of Stokes drift in X-band radar currents, after which it is possible to set up a standard validation procedure. As long as this knowledge is not available, the pseudo-Lagrangian validation method used in the study is preferred above the classical Eulerian ADCP validation.

6.1.2. INTERPRETING THE RELATIONSHIP

The relationship between accuracy and computational cube size for tidal currents outside storm conditions was found to be hyperbolic. Accuracies found for cube sizes ≥ 480 m are fairly equal and are located on the asymptote of the hyperbolic function. The smallest cube of 240 m has a significantly lower accuracy then cube sizes ≥ 480 m. The main reason for this is the spectral resolution. The spectral resolution is inversely related to the cube size, which means that spectral energy is allocated more precise for bigger cube sizes. An inverse relation describes a hyperbolic function as well. This means that the increase in spectral resolution (decrease proportional to $1/L$) is strongest for small increments added to small cube sizes. The effect of improved spectral resolution diminishes for bigger cube sizes. This is exactly what is observed for results obtained with cube sizes ≥ 480 m: the RMSE for these currents is comparable.

This partly explains why radar currents retrieved by using a cube size of 240 m are inaccurate. The other part of the explanation is the number of spectral components available for non-linear fitting. It is known that accuracy of a fitting algorithm decreases when the number of spectral components decreases. Figure 6.5

shows a plot of the number of spectral components available for non-linear fitting (regression coordinates). This number is obtained by a summation of the number of spectral components for **every frequency level in the filtered image spectrum**. Note that the *y*-axis has a logarithmic scale. The black lines mark the storm period. The figure demonstrates that for normal tidal flow, the difference in the number of spectral components is large between the cube sizes. The difference between the biggest cube and the smallest cube is approximately a factor 10. So it may be concluded that the low number of spectral components also has a significant contribution to the low accuracy of current estimates obtained by using a cube size of 240 m.

It was found that during the storm ($H_s > 2$ m), the correlation in current magnitude between radar and ADCP was lower. This is partly due to rain and fog in radar images and partly due to the applied formulation of the Stokes drift magnitude. However, figure 6.5 indicates that part of the inaccuracy during storm conditions may be attributed to a low number of regression coordinates that is available. The difference with normal tidal currents is a factor 5-10.

Finally, it is remarked that the current direction was found to be extremely sensitive to the cube size. However, this was found to be a general spatial pattern and is therefore described in the next section.

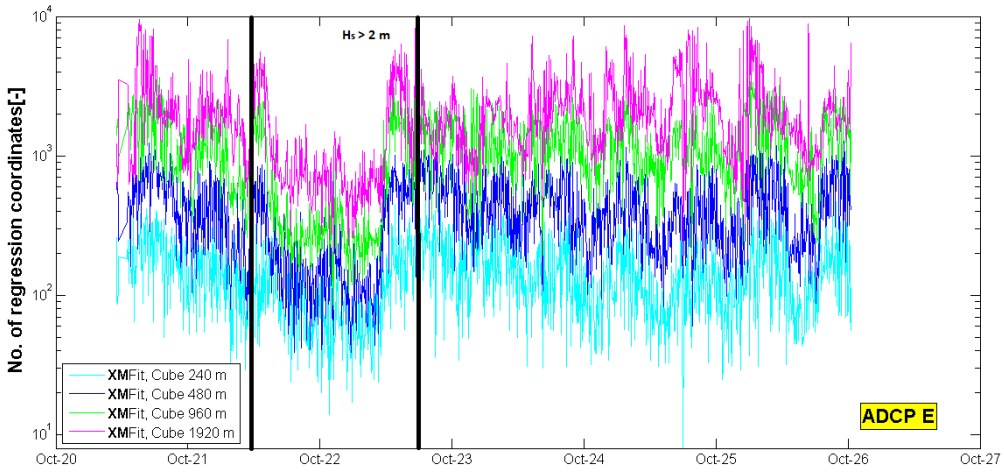

Figure 6.5: Number of regression coordinates available for non-linear fitting at location of ADCP E

6.2. SPATIAL VALIDATION

An impressive increase in accuracy is found by using pseudo-Lagrangian ground-truth instead of the purely Eulerian ADCP measurements. It was concluded that the data in this thesis supported that radar-currents are Lagrangian. Therefore, it may be expected that a comparison of radar currents with purely Lagrangian drifter measurements would yield even better results. The results of the spatial validation did not match these expectations. In this section, the focus is on explaining inaccurate results for grid points in the surf zone and the interpretation of the *cube size* - *accuracy* relation.

6.2.1. NEAR-SHORE CURRENT ESTIMATES

XMFit overestimates current magnitude for grid points in the surf zone (<500 m from coastline) for both the ebb and flood drifter deployment. For the ebb deployment, all grid points are located in this area since the drifters did not left the surf zone. The hypothesis is that non-linear wave effect in the surf zone are responsible for the overestimation of in-situ currents by XMFit.

Depth-inversion is based on linear wave theory. This implies that the requirements for the linear wave theory (chapter 2) should be met to obtain a reliable current estimate. However, wave breaking and wave transformation processes (shoaling) do not satisfy linear wave theory. In addition, uniform properties of d and $\vec{U}$ (uniform wave propagation behavior) are required to have a realistic estimate of hydrodynamics from spectral analysis. However, the surf zone is a complex hydrodynamic area in which small scale complex flow struc-

tures (surface drift, undertow, eddy, rip currents) may be present. In addition, the surf zone has a complex bathymetry (depth gradient, sand bars). Analogous to the reasoning of Bell et al. (2012), it is hypothesized that the image spectrum for a surf zone grid point is a merge of multiple wave dispersion regimes.

In order to identify anomalies from 'normal' image spectra, the concept of an image spectrum of the imaged sea surface should be understood a bit more in detail. A 3D image spectrum is the spectral representation of a series of Cartesian images in time. When the requirements for the validity of depth-inversion are met, its form is described by a dispersion shell (left panel figure 6.6). Longer waves have low frequencies in space and time and are therefore located in lower part of the spectrum (blue). Short waves have high frequencies and are located at a large distance from the origin (red), both in k and ω dimension.

The right panel of figure 6.6 shows an example of a slice of the raw image spectrum. The raw image spectrum is the unfiltered spectral representation of the Fourier transformed computational cube. In this chapter, $\omega-$ slices are considered: a horizontal slice of the image spectrum at a specific frequency level. The frequency slice that is considered in the right panel of figure 6.6 is indicated by a black contour line in the left panel.

The spectral energy density is color-coded. Blue indicates negligible spectral energy. Cyan indicates a noticable but relatively low energy content while green and yellow indicate moderate energy levels. Peak energy levels are shown in red. Typical spectra at the Sand Motor contain three 'groups' of data (refer back to section 2.1.3):

- I: Spectral energy of (linear) waves following the linear dispersion relation. For an optimal spectrum, this data forms a narrow banded circular/elliptic pattern in the second and third quadrant.
- II: Aliased energy that occurs due to temporal under-sampling. Since energy is 'folded' in case of aliasing, its location is approximately opposite to spectral energy indicated by I (first or fourth quadrant). In an optimal situation, all aliased energy is filtered out before application of depth-inversion
- III: Noise that is located randomly in the slice. In an optimal situation, all noise is filtered out.

Finally higher harmonics may be present, which are located between the origin and data of class I. They are not shown in the slice considered here. Again, in an optimal situation this data is filtered out. The red line in the figure indicates the result of depth inversion: the best-fit Doppler-shifted linear dispersion relation. In a spectrum of sufficient quality, the red line is nicely on top of the spectral energy of class I.

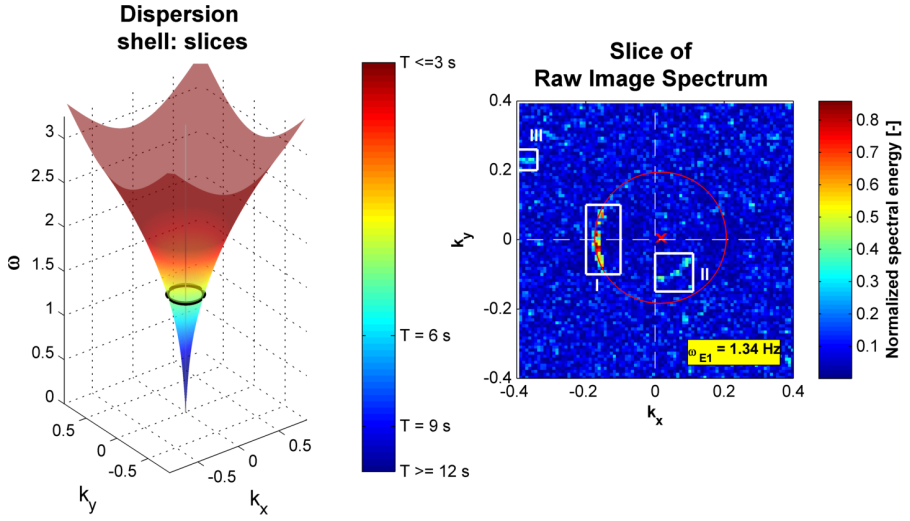

Figure 6.6: Illustration of a frequency slice of the image spectrum

Figure 6.7 strongly supports the hypothesis that non-linear wave effects cause anomalies in the spectra for grid points in the surf zone. A cube size of 960 m is used to extract the image spectrum. The plot of the current vectors comparison shows that the current estimates on 9:30:04 as well as its neighbors in time are inaccurate. The location of the point under consideration is located in very shallow water and in an area with a relatively strong bathymetric gradient (upper right panel). The middle right panel shows the top energy level slice of the raw image spectrum. The energy in this slice has the highest weight in the fit. The frequency (1.26 Hz) corresponds to a wave period of 5 s. Note that the slice of the raw image spectrum does show considerable differences with the normal (useful) spectra observed at the Sand Engine (compare with right panel figure 6.6). Spectral energy is not located on an ellipse describing the contour of a dispersion shell (red) but perpendicular to it. In addition, the spectrum contains a relatively high contribution of background noise.

The lower left panel shows the full 3D image spectrum, while the bottom right panel shows the top energy ω-slice of the spectrum. The filtered image spectrum is directly used to fit the dispersion shell. The 3D image spectrum is shaped completely different from a narrow dispersion surface. The spectral energy is scattered in spectral domain. This results in a fit that is a compromise between scattered data in spectral space. This is illustrated in the slice in the bottom right panel. The Doppler shift is the distance between the black and green crosses. The best fit Doppler shifted dispersion shell (green) is not nicely on top of the spectral data. The fit is a compromise between the spectral components that do not form a elliptical pattern.

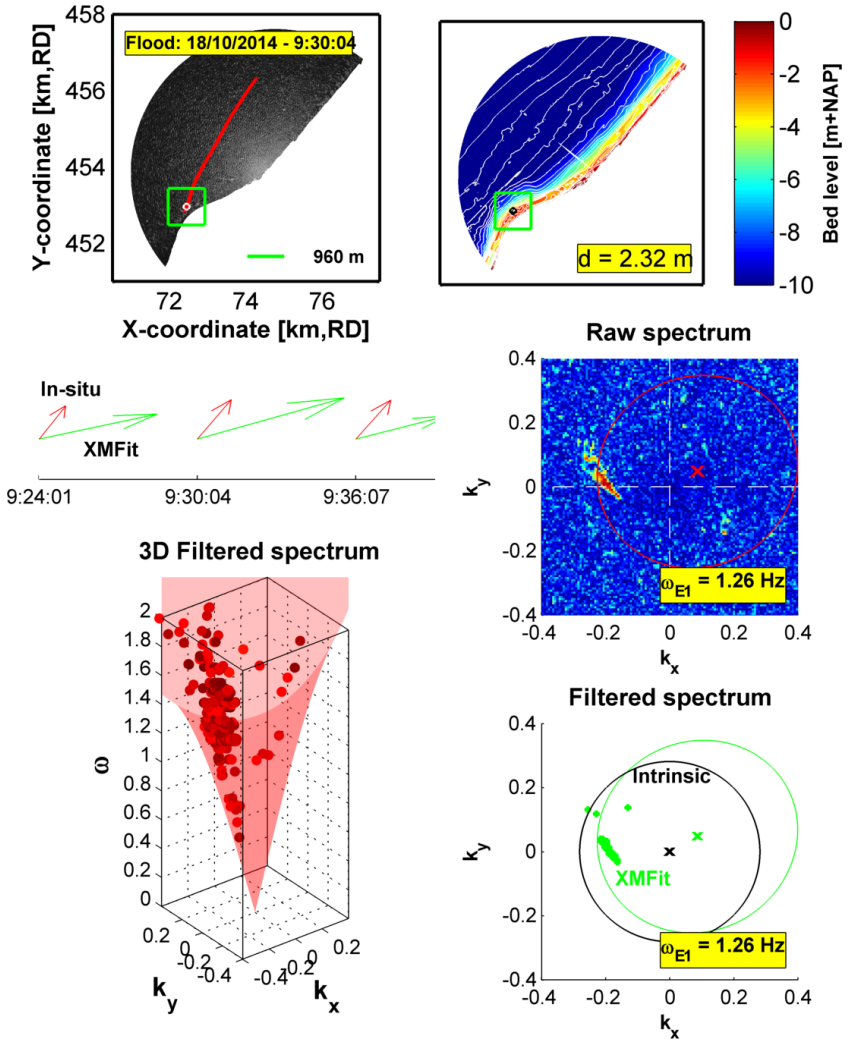

Figure 6.7: Distorted image spectrum for a surf zone grid point, leading to overestimation of current magnitude by XMFit

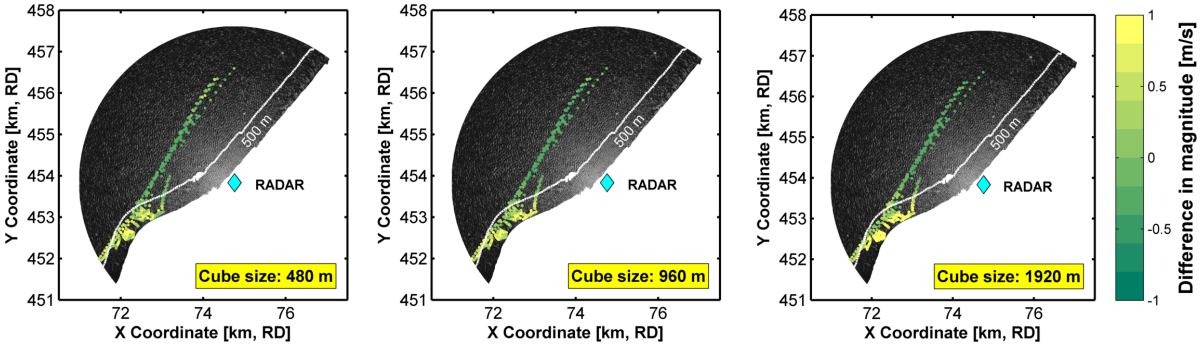

Figure 6.8: Overestimation of in-situ currents by XMFit for grid points between 0-500 m from the shoreline indicate that the currently used method should not be used to estimate currents at those locations

Figure 6.7 illustrates how different wave dispersion regimes and non-linear wave effects may affect current estimates. This is in line with Bell et al. (2012), who argue that highly varying conditions in the computational cube may introduce more then one possible solution for the current and depth. Not only the overestimation of the in-situ current by XMFit is explained by the figure, also the 'spikes' in the XMFit current magnitude for cube sizes > 1460 m are associated with similar anomalies in the image spectra. For increasing cube size, the risk for non-uniform hydrodynamic properties in the cube is higher since uniformly assumed wave behavior is analyzed over a growing spatial area.

The effect of non-linear wave effects on the spectrum was illustrated for a computational cube of 960 m, but is observed for all considered cube sizes (figure 6.8). The inaccurate results are limited to grid points closer than 500 m from the coastline. It is remarked that this separation does not indicate a sharp boundary. It indicates the approximate location of the transition and is only based on two drifter deployment sessions. Additional spatial validation is required to refine the location of the line more accurate. The inaccurate results for grid points in the surf zone emphasize the need for an alternative method of current retrieval. This method should be set up such that high-resolution spectra are obtained from a Fourier transform of very small cube sizes.

6.2.2. INTERPRETING THE RELATIONSHIP

In the previous it was shown why current estimates for grid points in the surf zone are inaccurate. This explains the poor results for the validation of XMFit currents for the ebb drifter deployment. A hyperbolic relation is found for the accuracy of XMFit at grid points outside the surf zone for the flood drifter deployment. First, the focus is on illustrating why current estimates obtained with a cube of 240 m are inaccurate. It is followed by the explanation for the underestimation and offset in current magnitude that was found for cube sizes of 480 m, 960 m and 1920 m.

Cube size of 240 m

The explanation for inaccurate results of XMFit for a cube size of 240 m was already introduced in the discussion on the *cube size - accuracy* relation for the point validation period. The spectral resolution was theoretically linked to the hyperbolic. Here the effect is examined in more detail for a single time stack to directly show the effect on the current estimate. A grid point in the middle of the representative track for the flood deployment period is selected, to exclude a possible influence of non-linear wave effects on the quality of the fit. Figure 6.9 illustrates the differences between the top energy level ω-slice of the image spectrum for cube sizes of 240 m and 960 m. A direct comparison of current vectors (upper right panel) shows that there is a relatively large deviation in the XMFit current estimates for the two different cube sizes. The middle row of panels shows the top energy level ω-slice of the raw image spectrum for both cube sizes. This top energy level corresponds to a peak period of 4.7 s. The raw spectrum for a cube size of 960 m is close to the description of a normal, usable spectrum (reference is made to figure 6.6). Spectral energy is allocated imprecise for a cube of 240 m: the blocks do not allow for a precise overlay by the dispersion relation. Spectral energy and best-fit dispersion shell (red line) matches reasonably well for a cube of 960 m, this in contrast to the 'thick' dispersion surface found for a cube size of 240 m.

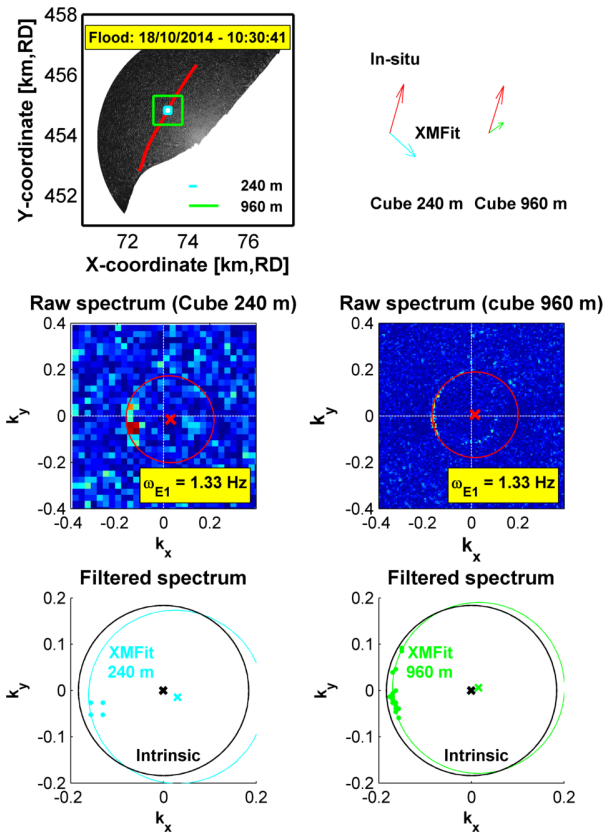

Figure 6.9: Comparison of raw and filtered image spectra for cube sizes of 240 m and 960 m

The bottom figures show the filtered slice of the image spectrum for both cubes. The black line represents the intrinsic dispersion shell (in absence of currents), while the colored line is the best fitting Doppler-shifted dispersion shell. The filtered spectrum for a cube of 240 m shows that noise is properly filtered out for the considered slice. However, the spectral energy (cyan dots) forms a 'thick' dispersion surface that does not allow for proper alignment with the thin Doppler-shifted shell (cyan). For a cube size of 960 m, the dispersion surface described by the spectral data (green dots) is thin, which allows for much better alignment with the Doppler-shifted dispersion shell (green). A better alignment indicates an improved precision of parameters.

Figure 6.9 clearly showed how current estimates are affected by the coarse spectral resolution dk: a thick dispersion surface and a thin dispersion shell do not match with any precision. It was already shown in the discussion of the point validation results that a low number of spectral regression coordinates form the other part of the explanation. The bottom panels of figure 6.9 confirm this. The number of spectral regression components along the representative flood drifter trajectory is shown in figure 6.10. The graph strengthens the claim that a small number of regression coordinates forms a substantial part of the explanation for the inaccuracy of XMFit for small cube sizes.

A combination of a coarse spectral resolution and a low number of regression coordinates was found to be responsible for the inaccurate results of XMFit for a cube size of 240 m. From figures 6.5 and 6.10 it is clear that the number of available regression coordinates rapidly increases with increasing cube size. It is thus expected that this issue plays a less important role for the quality of fit for cube sizes of 480 m, 960 m and 1920 m.

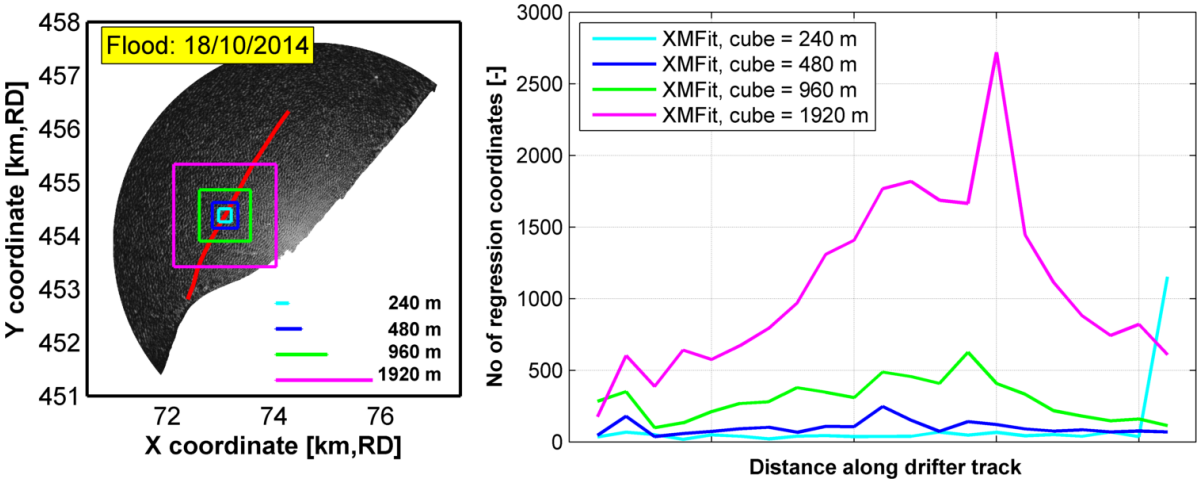

Figure 6.10: Number of spectral regression coordinates along the representative drifter track

Offset in direction

Both the point and spatial validation for flood currents showed how sensitive the current direction is to the cube size. A constant offset in direction was found, which tends to decrease with increasing cube size. At the same time, current magnitudes are slightly underestimated. It is hypothesized that the extreme sensitivity of current direction to computational cube size is mainly driven by the spectral resolution dk.

Figure 6.11 shows the filtered image spectra for a grid point in the center of the domain. The vectors in the lower left panel illustrate that the offset in angle decreases with increasing cube size. The upper right panel shows the spectral energy components of the filtered image spectrum for the highest energy frequency level (T = 4.25 s). The spectral energy for all cube sizes is located at fairly the same position in the third quadrant (highlighted by a red box). However, the fitted Doppler shifted dispersion shells do not show identical shifts with respect to the (no-current) intrinsic dispersion shell (black). The crosses indicate the center of the dispersion shells. The vector between the black and the colored cross represents the Doppler-shift $k\vec{U}_e$. Note that the Doppler shift has different directions for the various cube sizes.

The location of the spectral energy in the red box is magnified in the lower panel. Here the influence of the spectral resolution is clearly visible: spectral energy is 'shifting' to the left due to a more precise allocation of the spectral energy in $k-\omega$ space. This shift is on a sub-pixel scale. However, the upper panel shows that the shift has a significant influence on the observed Doppler shift. This figure thus clearly illustrates that the current is extremely sensitive to the position and amount of spectral energy available for non-linear fitting.

The findings presented in this section confirm the research of Piotrowski and Dugan (2002) in which higher accuracies obtained with increasing cube sizes was explained by the increase in spectral resolution. Gangeskar (2002) researched the most important error sources in X-band radar current estimates and identified the spectral resolution as a key factor as well. In addition Friedman (2014) already indicated that the fitting procedure was extremely sensitive to the data when comparing the results for two solvers of XMFit. He concluded that X-band depth-inversion is extremely sensitive to the spectral data, since two different solvers yield a depth difference of 1 m for spectra that were visually identical. The role of the number of available regression for the fit was already emphasized by Senet et al. (2001). They argue that accuracy increases with an increase in the number of regression coordinates.

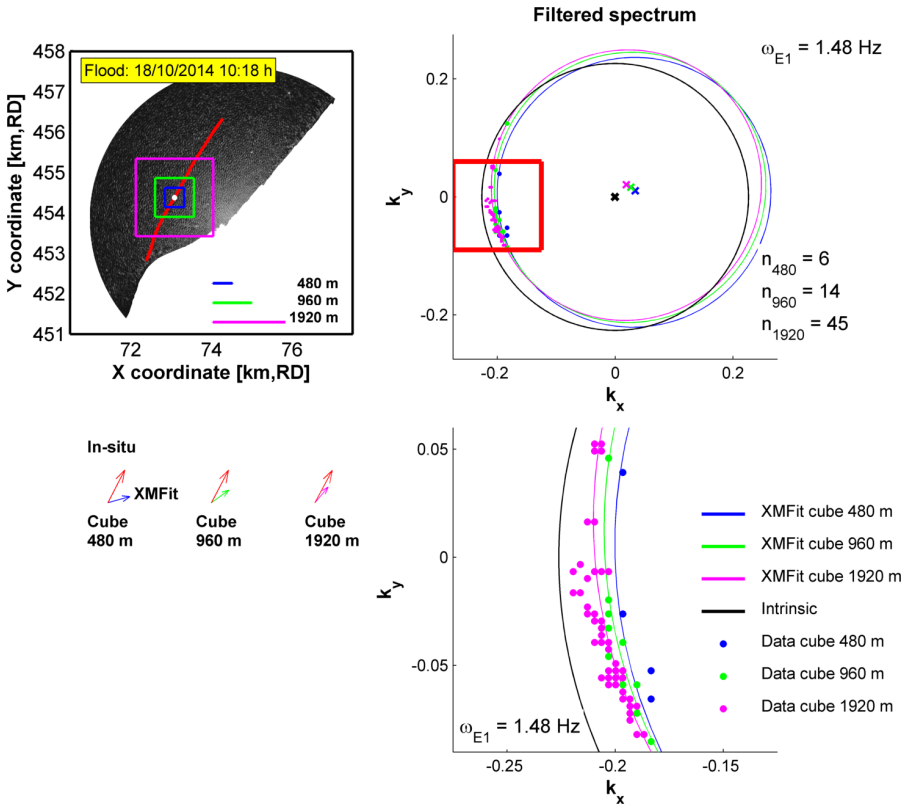

Figure 6.11: Comparison of highest energy ω-slice of a single image spectrum for multiple cube sizes

These findings are very important since the two key drivers for differences in current estimates between cube sizes are identified. In order to enable high resolution mapping using small cube sizes, the focus should be on finding a method that enables of the estimation of high-resolution spectra for small cube sizes which should also contain a sufficient amount of data. This finding also shows that the application of radar-derived currents in coastal engineering projects should be considered carefully. The quality of the image spectrum should be optimal to obtain a reliable current estimate. Small deviations in the image spectrum may cause considerable differences in the current estimates.

6.3. SPECTRAL FILTERING

The point and spatial validation were performed for two different time periods. It was observed that the results of XMFit during the drifter validation period had a significantly lower accuracy than the results for the point validation period. This is contrary to the expectations: it was expected that purely Lagrangian measurements would give more accurate results, especially since a high correlation with pseudo-Lagrangian ADCP currents was found in the point validation. In this section it is demonstrated that these unexpected results may be allocated to improper functioning of the applied spectral filters.

6.3.1. DIFFERENCES BETWEEN VALIDATION PERIODS

It should first be understood why the differences in accuracy between both validation periods arise. Before looking to possible mechanisms, it should be made sure that the differences do **not** arise due to the fact that measurements from another in-situ instrument are used. Therefore, XMFit current estimates at the location of ADCP F are compared to the in-situ ADCP measurements for the **period of the spatial validation of flood currents**. The results, obtained with a computational cube size of 960 m, are shown in figure 6.12.

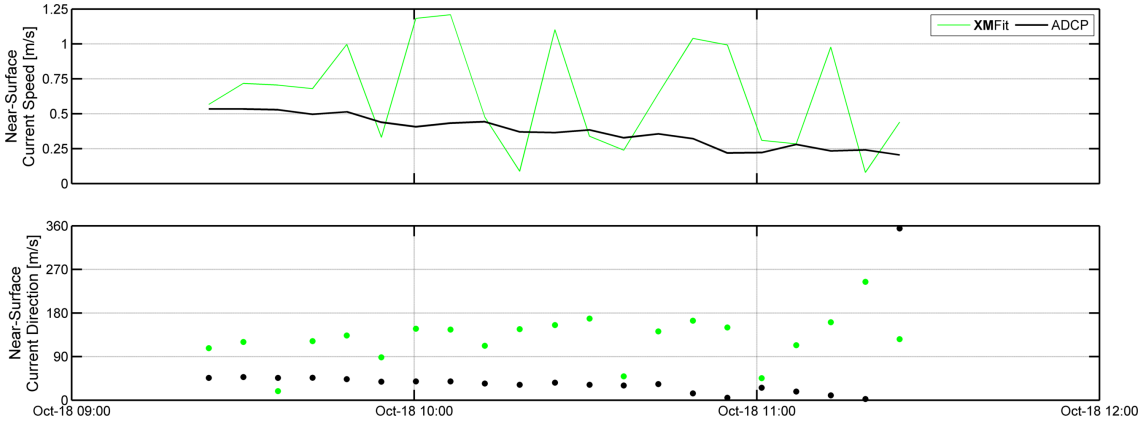

Figure 6.12: Inaccurate current estimates of XMFit (cube size 960 m) at location of ADCP F during the period of spatial validation

The results show that XMFit and ADCP have big differences in magnitude and direction for the spatial validation period. The magnitude is overestimated by XMFit (upper panel), while underestimation was found in the spatial validation along drifter trajectories. The difference in direction (bottom panel figure 6.12) may increase to 100 °. This offset in direction was also observed when spatially validating XMFit along drifter trajectories. However, it was **not** observed in the results for the point validation period. The value of the offset in direction showed to be variable over time, especially for successive grid points near the edge of the radar domain for a cube size of 480 m (refer back to figure 5.8).

To be able to explain the relatively large variation in the offset in time (space), the fit at two of these grid points is investigated for a cube of 480 m (upper left panel). The direct comparison of current vectors of in-situ drifter (red arrow) and XMFit (blue arrow) shows that directions and magnitude of the vector are fairly different for the two successive moments in time.

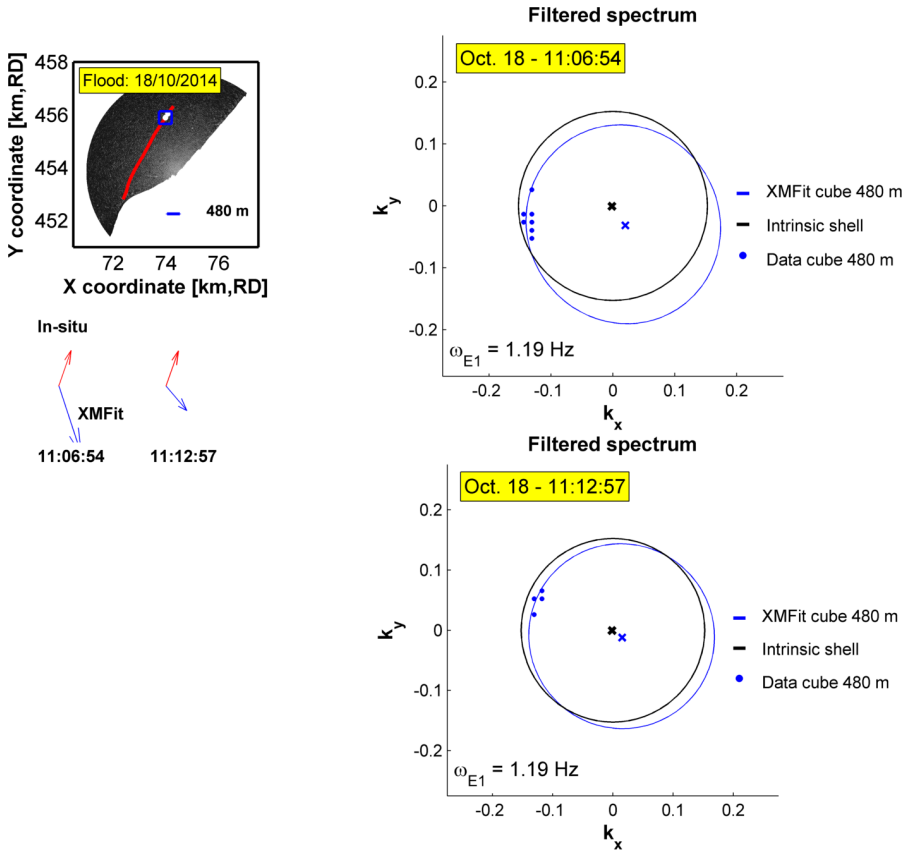

Figure 6.13: Comparison of the top energy ω-slice of the filtered image spectrum for two successive grid points

The two panels at the right show the top energy ω-slice of the **filtered** image spectrum for both grid points. The spectral data for the second grid point is positioned at completely different k_x, k_y coordinates. This results in the Doppler shifted dispersion shell being fit completely different.

The change in position of the spectral data might indicate a sudden change in peak wave direction, which is rather unlikely for a short 6-minute time interval. In addition, the comparison of XMFit and the wave buoy peak wave direction (figure 5.5, section 5.3.2) showed that the wave statistics of XMFit and wave buoy during the drifter deployment aligned well during this period in time. It is therefore concluded that the difference in positioning of the spectral data in the selected ω- slice is due to the spectral filtering process, since these filtering operations directly influence which points are selected for non-linear fitting in XMFit.

Therefore, spectral filtering is examined in more detail. The raw image spectrum is subject to four filters before the non-linear fitting is performed. The filters are ordered in the sequence of applying the filters in XMFit:

- Frequency filtering: filter spectral components outside bounds for minimum and maximum frequency
- Wide dispersion filtering: filter spectral components outside bounds for lower and upper bound for d
- Global Aliasing: filter that separates real spectral energy from aliased energy based on mean wave direction
- Minimum spectral energy cutoff: high pass filter to remove noise and higher harmonics from the image spectrum

The same frequency and wide-dispersion filtering parameters are used in the point- and the spatial validation, so these are not responsible for the differences in accuracies between both periods. A combination of the Global Aliasing and minimum spectral energy cutoff E_{lim} is thus responsible. In the next sections, the sensitivity and effects of the spectral filtering operations on the current estimate is discussed.

6.3.2. FREQUENCY FILTER

The frequency filter determines the lowest and highest ω- value that is taken into account in the fit. These frequency limits are specified as minimum and maximum wave periods. The frequency filter in XMFit allows spectral components of waves with a period in the interval 3-12 s in the frequency spectrum (Friedman (2014)). The sensitivity of the XMFit current estimate to the frequency limits and its effects are is analyzed by means of partial fitting: the fit of the linear dispersion relation to confined parts of the image spectrum. The 3-12 s interval is split into 9 subintervals with a width of 1s. For each of these sub intervals, a fit is performed on the spectral components of exclusively the waves in that specific sub-interval. The partial fitting is illustrated for the bin of 4-5 s waves in figure 6.14. The spectral components that are not in this bin (and therefore excluded from the fit) are shown in gray. The dispersion shell (red) is fitted to the colored spectral data.

A computational cube size of 960 m is used to generate the results. The non-linear regression solver was chosen. This proof of concept is inherent to the solver and can be generalized to all solvers that use the same regression principles. The results of the partial fitting at the location of ADCP E are shown in figure 6.15. The black dots represents the current estimate using the spectral information over the full range of frequencies (3-12 s). The more close the result of a partial fit is to full spectrum fit (black dots), the more sensitive the current estimate is to this spectral components. The figure shows that current estimates are predominantly based on spectral energy associated with waves in the interval of 3-5 s (green dots), since the green dots almost perfectly overlay the black dots. The partial fitting results for the spectral energy of intermediate and long waves with periods > 5 s indicate two important findings. The current estimate is not sensitive to spectral components with periods > 5 s since there is no overlap at all between red and black dots. In addition, the energy of longer waves have a bad influence on the current estimate of XMFit. The partial fitting results show that a fit on the spectral energy of longer waves results in unrealistic high current estimates (second and third panel).

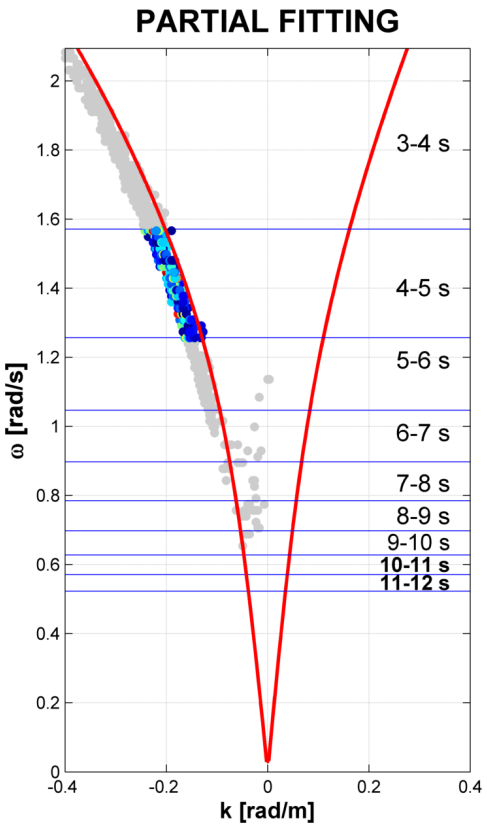

Figure 6.14: Illustration of partial fit on spectral wave components in the interval 5-6 s

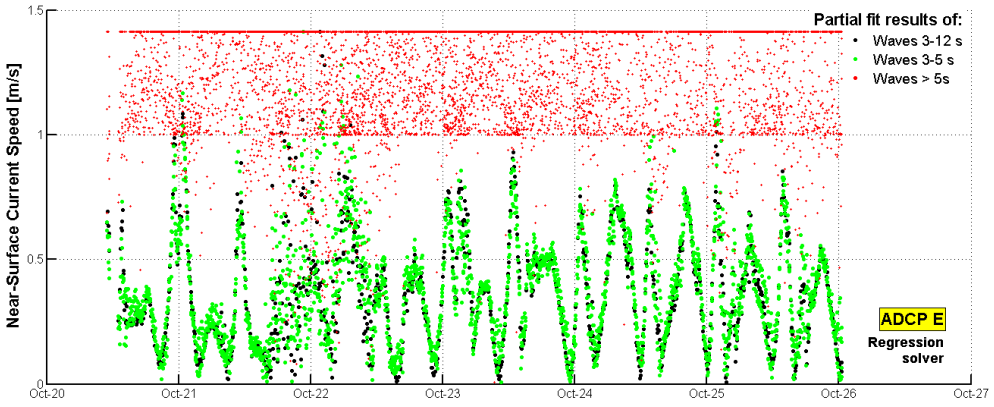

Figure 6.15: XMFit current estimate is heavily weighting on spectral components of waves with periods of 3-5 seconds

The results in figure 6.15 showed that for the non-linear regression fitting method, the current exclusively depends on short waves with periods of 3-5 s. Piotrowski and Dugan (2002) argue that this is due to a combination of two factors: the Doppler shift is most prominent in the high frequency components of the spectrum and short waves are exclusively affected by near-surface currents. Yuan et al. (2012) developed a theoretical formula that links the change in shell shape to the wave number and showed that short waves "do seriously affect the current". He remarked that the spectral energy of short wave components is low. The radar data in this thesis showed that the image spectra were dominated by short wave components regarding the number of regression coordinates. Thus, a high number of short waves components in the spectrum explains the dominance of this waves in the fit. The negative influence of long wave energy was also found by Yuan et al. (2012). He showed theoretically and experimentally that low wave number energy negatively influences the current estimate.

The results are touching an important issue regarding depth-inversion, which shows once more to be a balance between short- and long wave energy. In this section it was shown that current estimates require short waves. However, Bell and Osler (2011) showed that a good depth estimate requires a certain wave length, which increases with increasing depth. Thus for deeper areas the requirements for good depth- and current estimates may be opposite. It may be relevant since it is likely that XMFit functions more properly when depth- and currents are estimated subsequently instead of simultaneous.

The results in this section show that fitting the dispersion relation to short wave components (3-5 s) yields approximately the same current series as a fit to the spectral components of 3-12 s. It is concluded that the current estimate is not sensitive to value for the lower limit of the wave frequency (highest wave period T), as long as this value is > 5 s. Therefore, the frequency filter values are not adjusted in the optimization of the spectral filtering process, especially since during storm conditions (point validation period) wave periods of around 12 s physically occur.

6.3.3. SENSITIVITY AND OPTIMIZATION

The current estimate was found to be insensitive to the frequency filtering limits, as long as spectral components corresponding to waves of 3-5 s remain included in the fit. The three remaining filtering operations (wide dispersion filtering, Global Aliasing, minimal spectral energy cutoff) are discussed here. Similar to the frequency filter, it is tested how sensitive the current estimate of XMFit is to the spectral filtering operations. The parameters determining the behavior of the spectral filters are as follows:

- Upper d_{lim}, upper depth limit for wide dispersion filter, which determines the part of the spectrum that is cutoff at the side of the origin (figure 6.16). Selecting a higher value for the upper d_{lim} implies that a smaller part is cutoff. The lower depth limit is kept constant.

- *MWD* Global Aliasing Mean wave direction. The orthogonal line to the spectral energy cuts off the image spectrum in two parts to seperate real and aliased spectral energy. The Global Aliasing Mean wave direction is extracted from a big computational cube in the center of the domain (reference is made to section 3.2).

- E_{lim}, minimum spectral energy cutoff, adaptively selected by XMFit in the range of 0.4 - 0.6. Functions as high pass filter: only spectral components with normalized spectral energy > E_{lim} do pass the filter.

The outcomes of this sensitivity analysis are presented for October 18^{th} 10.00 h UTC at the location of ADCP F. This particular time and location was chosen since XMFit and ADCP currents do not align at this moment in time. The sensitivity analysis is performed as follows: two of the filtering parameters are kept constant and the third parameter is varied. The current magnitude as function of that parameter is plotted in the upper panel. The bottom panel for each parameter shows the current direction as function of the parameter that is varied. The results of the sensitivity analysis for the considered time stack are shown in the right panels of figure 6.17.

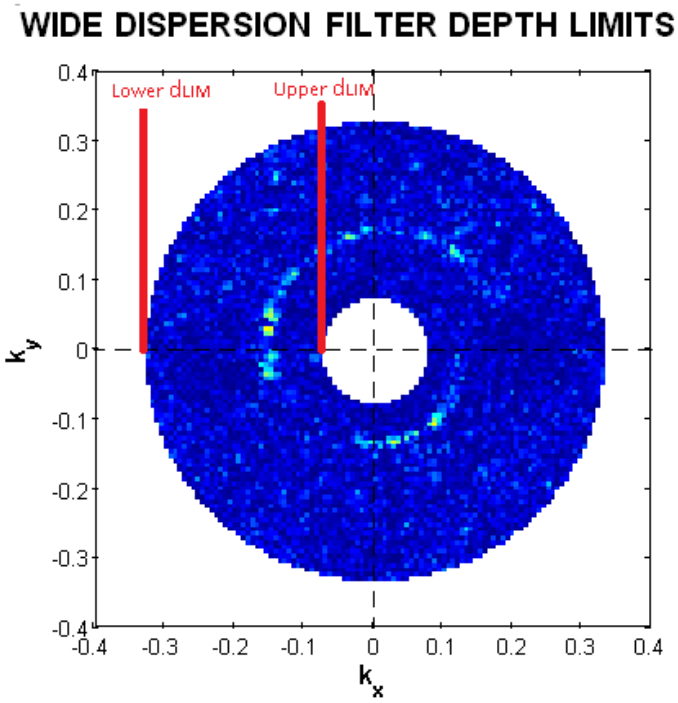

Figure 6.16: Upper and lower depth limit determine the width of the filtered image spectrum

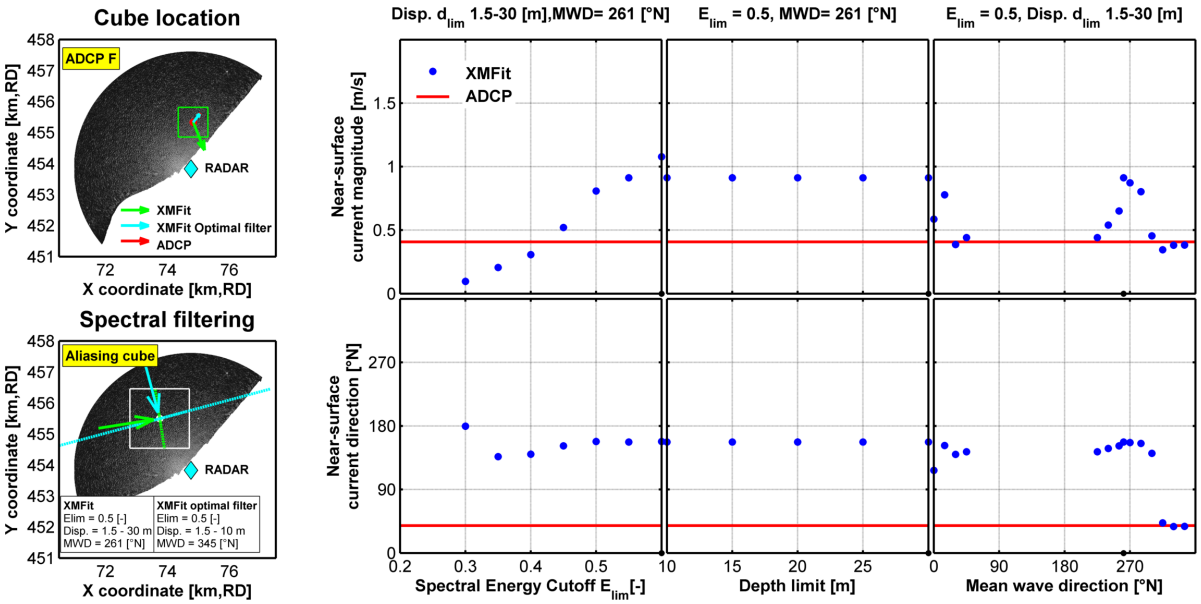

Figure 6.17: Sensitivity of XMFit current estimates to spectral filter parameters (October 18, 10.00 h UTC)

Spectral energy cutoffs lower then 0.3 are not tested since selecting lower values implies that risk that noise is not filtered out drastically increases. The mean wave direction (coming from) is varied from 0 - 45 $^{\circ}N$ and from 225 - 360 $^{\circ}N$, since waves can only physically arrive from that direction. Wave directions between 45 - 225 $^{\circ}N$ would mean that waves are approaching from the land. The upper depth limit for the wide dispersion filter was varied between 10 - 30 m since the maximum depth at the ADCP location is 9.8 m and depths in the radar range do not exceed 30 m.

The figures illustrate that a variation in the upper depth limit of the wide dispersion filter has negligible influence on the current magnitude and direction. The current direction is not sensitive to the spectral energy cutoff E_{lim}, but the current magnitude is. However, the main problem that was found is the large offset in current direction during the spatial validation period. This problem is caused by the Global Aliasing mean wave direction *MWD*. The current direction is estimated almost perfectly by XMFit for MWD values > 310 $^{\circ}N$, for which also the current magnitude has high accuracy values. For other values of this parameter, the XMFit current direction has a large offset.

A 'brute forcing' approach is used to determine the optimum set of filtering parameters that lead to the most accurate current estimate of XMFit for this moment in time. XMFit current estimates are produced for all possible combinations of the filter parameters within their range of variation. Subsequently, the set of filtering parameters for which the XMFit **current direction** is most close to the ADCP **current direction** is selected. This set of parameters is hereafter referred to as XMFit optimal filter. Best agreement in current direction is chosen since it is tried to identify and solve the offset in current direction. The spectral filtering parameter values for XMFit in normal mode and XMFit optimal filter are shown in the bottom left panel of figure 6.17. Observe that, in agreement with the sensitivity analysis, the Global Aliasing Mean wave direction has a value > 310 $^{\circ}N$. The difference in this filtering parameter is approximately 90 degrees with respect to the normal situation. This implies that spectral coordinates of the upper half of the spectrum are being fit in depth inversion for the optimal filter parameter set. In the upper left panel of figure 6.17 shows that the current vector estimated with the optimal filter set is almost perfectly atop of the ADCP current vector.

The previous shows that the large offset in XMFit current direction may be solved by selecting a Global Aliasing Mean wave direction > 310 $^{\circ}N$. The reason for this is that the Global Aliasing Mean wave direction is extracted from the image spectrum of the Aliasing Cube while the spectral energy for depth-inversion is extracted from a Fourier transform of the local computational cube. These are two different locations. Due to refraction of the imaged ocean waves, spectral energy in the computational cube is located at other k_x, k_y coordinates than in the aliasing cube.

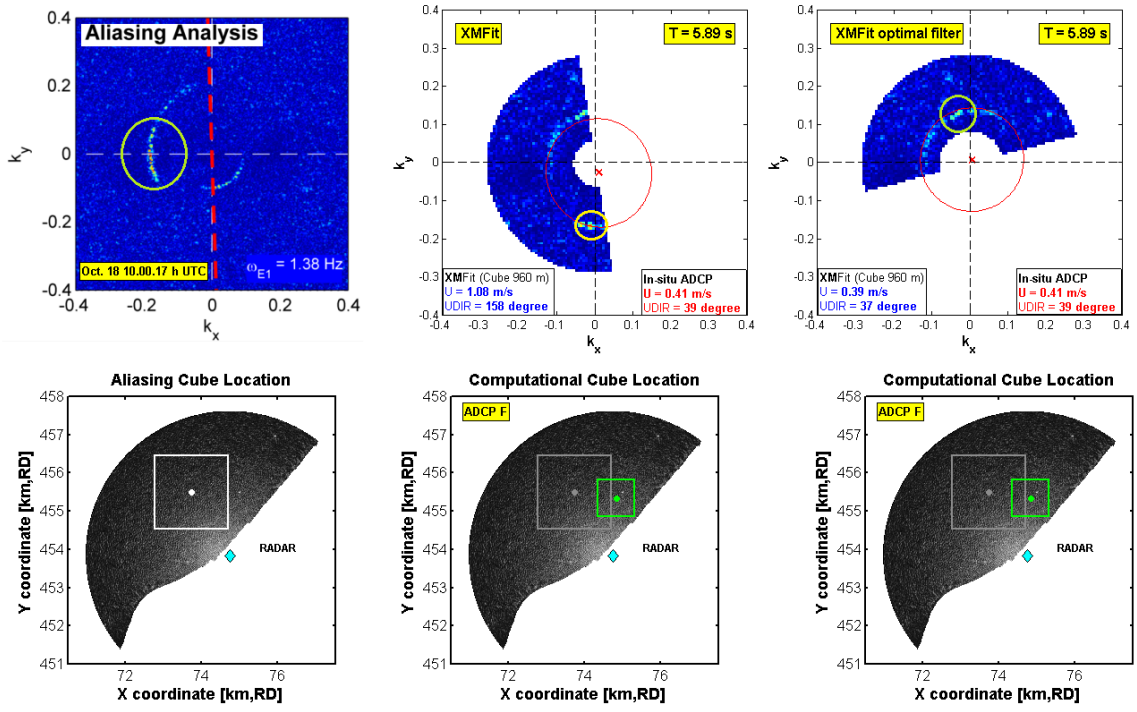

Figure 6.18: The optimal wave filter cuts off the lower half of the image spectrum and does not include the detrimental aliased energy.

The spectral components with the highest energy in the Aliasing cube are predominantly located around 260 - 280 $^{\circ}N$, indicated by a green circle in the upper left panel. As a result, the orthogonal line (red line) is approximately aligned with the y-axis. This orthogonal line, obtained at the Aliasing cube location, is used to filter the spectrum **at the location of the grid point** (second panel figure 6.18). However, the application of this leads to incorrect selection of spectral energy, since for this spectral cutoff aliased data is still in the spectrum (yellow circle). Note that the aliased spectral components have equal or slightly higher energy content in this ω-slice of the spectrum. This is the case for multiple slices of the 3D spectrum, so that the aliased data has the highest weight in the fitting procedure. The current is therefore far off from the real ADCP values.

The optimal filter parameter set performs so much better since the aliased spectral components are fully cutoff in this case (upper right panel). The fit is now on the spectral components that follow the linear dispersion relation (green). This data was partly removed by applying the Global Aliasing Mean wave direction to filter the image spectrum. Since the fit for the optimal filter settings is exactly on the spectral components that follow the linear dispersion relation, the current magnitude and direction come very close to the in-situ ADCP values. Note that the best-fit Doppler shifted linear dispersion relation (red line) is not perfect on the data for this frequency, since we saw in the previous section that 3-5 seconds waves are most heavily weighted in the fit.

The proof of concept for the single time stack shows promising results. Therefore the brute forcing method to find optimal filter parameters is applied to every time stack for the spatial validation of flood currents. The current estimates of XMFit with optimal filter parameters is compared to both ADCP and drifter in-situ measurements. The results are shown in figure 6.19.

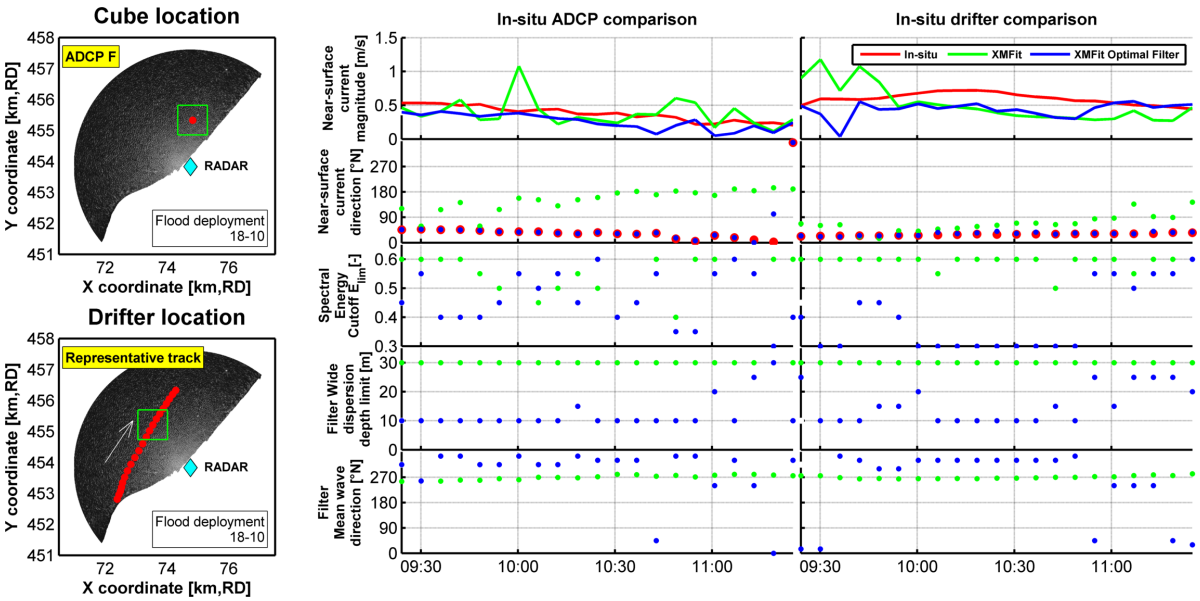

Figure 6.19: The brute forcing approach to find optimal filter parameters resolves the offset in current direction

The two left panels show the grid points for the comparison. In the right set of graphs, the left column of graphs presents the comparison with in-situ ADCP data. The right column of graphs shows time series for comparison with in-situ drifter measurements along the representative track. In each column, the upper two plots shows the comparison between in-situ and XMFit currents regarding magnitude and direction. The bottom three panels show the filtering parameters used to obtain the current estimate of XMFit. The current direction is estimated almost perfectly by running XMFit with optimal filter settings, while there was a big difference observed with the 'normal' settings. The current magnitude with optimal filter settings is has approximately the same deviation from in-situ as XMFit in normal mode. The optimal filter settings show that the spectral energy cutoff E_{lim} is variable over time: no clear pattern is visible. A wide dispersion upper depth limit of 10 is preferred above a cutoff of 30 m. In addition, the optimum filter Mean wave direction shows up to be in the range 315 - 360 $^{\circ}N$, instead of 270 $^{\circ}N$ found by using XMFit in normal mode.

The results regarding the sensitivity and optimization of the filtering parameters showed that the current estimate of XMFit is most sensitive to the Global Aliasing Mean wave direction parameter. The optimum value of this parameter is found between 315 - 360 $^{\circ}N$ instead of 270 $^{\circ}N$ for XMFit in normal mode. The XMFit optimal filter current estimates are very accurate compared to in-situ data, especially regarding current direction. The reason that the optimal filter value of the Global Aliasing Mean Wave direction provides so much better results is that the spectral cutoff is not allowing aliased data in anymore and fits only on the correct spectral energy. This was linked to the change of location of the highest energy spectral components in the ω-slice between different spatial locations. Most likely this is due to wave refraction between the Global Aliasing cube location and the computational cube location.

The results presented in this section urge the need to adjust the filtering procedure in XMFit. The focus should be on the Global Aliasing Mean Wave direction. Quick improvements may be achieved by fixing the Global Aliasing mean wave direction to a fixed value of $315^{\circ}N$, since the orthogonal line then represents a wave crest approaching perpendicular to the shore line. The image spectrum is then cutoff in such a way that only wave components from the sea are included in the fit. However, a long-term solution is to develop a filtering procedure that takes refraction into account: however, since the radar oversees a complex hydrodynamic area, this may become a rather complex exercise. Fixing the Global Aliasing mean wave direction to a fixed value of $315^{\circ}N$ is a simple and effective method to increase the accuracy of the XMFit algorithm considerably.

7

CONCLUSION

The aim of this thesis is to find the relation between spatial scale of wave dispersion analysis (*computational cube size*) and X-band radar current measurement accuracy at the Sand Engine. The following conclusions support the successful achievement of this objective.

It is emphasized that all conclusions presented in this chapter are limited to three periods of relatively short duration for the Sand Engine study site. In addition, the conclusions are exclusively valid for the estimation of current $\vec{U}$ with known depth d.

The answer to the research question - *How do accuracy and spatial scale relate for a single point and a fixed temporal scale?* - is found by performing a point validation for spatial scales of 240 m, 480 m, 960 m and 1920 m at locations of two deployed ADCP instruments. The results for the point validation (chapter 4) for normal tidal flow conditions showed that the relation between computational cube size and radar measurement accuracy is hyperbolic for both ebb and flood currents. The current estimates obtained with cube sizes of 480 m, 960 m and 1920 m have a RMSE of approximately 0.2 m/s and are located on the asymptote of the hyperbolic. In-situ currents are overestimated by using XMFit with a cube size of 240 m and have a RMSE in the order of 0.3-0.4 m/s. A lower accuracy is observed during the storm ($H_s > 2$ m), which was shown to stem from an inaccurate estimate of the cross-shore component.

Radar current measurements were compared to temporally and spatially averaged Lagrangian drifter current measurements to answer the question *How does this relation differ for radar currents along drifter trajectories in the radar domain?* The spatial validation was performed for two different periods than the period considered in the point validation. The study period for validation with drifter measurements was based on the spatial extent of the drifter measurements. The results described in chapter 5 show that XMFit largely overestimates in-situ currents (difference > 1 m/s) for grid points in the first 500 m from the coastline (surf zone). This is associated with non-linear wave effects that cause anomalies from the shape of a usable spectrum (chapter 6).

For grid points outside the surf zone, it was found that the relation between cube size and measurement accuracy is hyperbolic. The hyperbolic relation between computational cube size and radar current measurement accuracy was explained in chapter 6 by the hyperbolic (inverse) relation between cube size and spectral resolution. A time-variable offset between XMFit and ADCP current direction is observed. The offset tends to decrease with increasing cube size, which is explained by the extreme sensitivity of current direction to the allocation of spectral energy in k_x, k_y-space. The data is allocated more precisely for bigger cube sizes since the spectral resolution is higher. XMFit current estimates obtained with a cube size of 240 m results are inaccurate along drifter tracks, in agreement with the results of the point validation. This was linked to poor spectral resolution and a small number of spectral components available for non-linear fitting of the linear dispersion shell.

In general, accuracy values found along the drifter trajectories are lower than a direct comparison of radar and ADCP currents. This was unexpected since the results for the point validation supported that X-band

radar current measurements are Lagrangian. XMFit current estimates were compared to pseudo-Lagrangian ADCP currents, obtained by correcting Eulerian ADCP measurements for the surface Stokes drift. The analysis in chapter 6 has proven that a significant mismatch in cross-shore direction is found by comparing radar currents to purely Eulerian ADCP measurements during storm conditions.

The fact that XMFit current estimates for the spatial validation are poorer then expected is linked to the moment in time. This was proved by low correspondence between XMFit current estimates and ADCP in-situ measurements for this period. For the point validation time period it was observed that correlation was high. The reduced performance of XMFit for the spatial validation period is explained by the fact that XMFit takes the undesirable aliased spectral energy components into account for depth-inversion (chapter 6). In case of proper spectral filtering, the aliased spectral energy components should be filtered out. A sensitivity analysis to the four spectral filters has shown that XMFit current estimates for this period in time are most sensitive to the Global Aliasing filter. A brute forcing approach, in which an optimal filter parameter set is found by trying all possible combinations, showed that the optimal filter parameter for the Global Aliasing is far off from the value that XMFit normally gives. The optimal value is explained by the fact that spectral components with highest energy levels are located at other positions in the image spectrum.

The differences in accuracy between both validation periods emphasizes that the results are specifically valid for the time periods considered in the point- and spatial validation work. For the point validation period, the filter accidentally works fine, however for slightly other wave conditions in the spatial validation period, the current estimates may be heavily influenced by an improper functioning filter. Therefore, generalizing the results from this thesis to other locations and time periods is still difficult. Therefore, additional temporal and spatial validation is required under various environmental conditions.

This research revealed that accurate radar current measurements are predominantly based on a (correctly filtered) image spectrum with high spectral resolution. Therefore, optimizing the filtering and developing new methods to obtain accurate radar measurements with small cube sizes should be the points of focus of additional work with the XMFit algorithm. Full confidence in the XMFit current retrieval method should be obtained for simple cases with low complexity before studying complex hydrodynamics.

8

RECOMMENDATIONS

The work presented in this thesis examined the relation between spatial scale of wave dispersion analysis and accuracy of radar current measurements. Validation of radar currents was performed by comparing radar currents to ADCP measurements of a 6-day period and two periods of approximately 3 hours of drifter measurements. Radar currents were obtained by analyzing wave dispersion on several spatial scales. In this chapter, the limitations of this study are described and opportunities to improve XMFit current estimates even further are recommended.

It is emphasized first that a higher level of understanding about the fundamentals of radar currents is required. Striking examples were knowledge is lacking are the debate about Stokes drift in radar images, the uncertainty in the valid depth of radar current measurements and the spatial quality of radar derived current fields. Validation studies in general examine the performance of radar current measurements only for a short period, often associated with ideal conditions. The first step towards improved understanding of radar current fundamentals is a continuous spatial validation for an extensive period in time. Then a better understanding of the performance of X-band radar under various environmental conditions is obtained. In this work, a complex hydrodynamic area is considered. However, to obtain detailed understanding on radar currents it is strongly recommended to validate radar currents in an area with simple hydrodynamics.

This study was limited to the relation between the spatial scale of wave dispersion analysis and the accuracy. However, previous research showed that the temporal scale of the analysis is a key factor for the accuracy as well, since the temporal scale directly relates to the frequency resolution of the image spectrum and the number of spectral components in the fit. Therefore is recommended to investigate the effect of the temporal scale on the accuracy by keeping the spatial scale of wave analysis constant and vary the temporal scale. This additional research should then be concluded with the relation between both scales of wave dispersion analysis and the accuracy of radar current measurements.

In this thesis, it was assumed that radar current measurements are Lagrangian. Missing ADCP measurements for the near-surface layer of the ocean forced to develop a method in which information of Lagrangian Stokes drift for this layer is included. Therefore, the Eulerian measurements of two deployed ADCP at two single locations are corrected for the surface Stokes drift. Impressive improvements in the results was obtained due to this correction. Therefore it was concluded that the current data supports that radar current measurements are Lagrangian. However, the alignment in current magnitude during the storm is still needs improvement. This is required because the Stokes drift formulation applied in this work is valid for a single ocean wave. However, in this thesis mean values for the variables were substituted, resulting in only a rough estimation of the actual occurring Stokes drift. It is recommended to do more research on which part of the Stokes drift is exactly included in the raw X-band radar current. Herein the focus should be on storm conditions in shallow areas, for which the effect of Stokes drift is most pronounced. The most suitable approach is to apply the formulation to individual spectral wave components in order to calculate the Stokes drift for a single spectral component. Hereby it is extremely valuable to use measured directional wave spectra at the location of the in-situ instrument. This additional work on Stokes drift should aim to obtain theoretical and more physical evidence for radar currents being Lagrangian, which may ultimately lead to a validation procedure in which

standardized in-situ measurements are prescribed as ground-truth.

Another limitation of this study is the drifter data. Those measurements are obtained with another purpose than radar validation. Therefore, drifters were not repetitively deployed in the same area but move freely trough the radar domain. The dynamic grid approach was developed, in which radar and in-situ current are compared on similar spatial and temporal scales along a drifter track. However, this strongly limits the area where radar current measurements are validated. Only grid points along a few drifter tracks are examined, which have limited spatial coverage. It is therefore recommended to do a large-scale spatial validation of radar currents. This experiment should include the simultaneous deployment of multiple ADCP and drifter instrument on the same moment in time. The ADCP should be placed in multiple cross-shore arrays so that full coverage of the radar-domain is obtained. Drifters should be repetitively deployed in several predefined fixed squares that cover the full radar domain according to the method of Ohlmann et al. (2007). This large scale experiment may provide information on the spatial quality of radar current fields.

The spatial validation revealed that XMFit does return inaccurate estimates of the in-situ current for grid points in the surf zone (first 500 m from the coastline). The consistent overestimation was linked to anomalies in image spectra due to non-linear wave effects and non-uniform wave dispersion properties over a large computational area. It is therefore recommended to develop an adjusted method to be able to accurately derive in-situ currents for a large part of the surf zone. The focus should be on obtaining high resolution image spectra for small cube sizes, since the hydrodynamics have a higher chance of being uniform in smaller areas. Furthermore, this method should include non-linear wave effects that are responsible for anomalies in the image spectra. It is remarked that from the location where waves start to break to the shore, depth-inversion should not be applied at all since it is based on the linear wave theory, which is not valid for this area.

This thesis work has proven that the accuracy of radar current measurements is extremely sensitive to the spectral information. Optimization of spectral information used in the depth-inversion algorithm is the key to even more accurate current estimates by XMFit. The results for the spatial validation showed that a properly functioning filter to remove aliased spectral energy is essential. With brute forcing, a set of optimal parameters is found that resolves the offset in current direction. However, this method is inefficient regarding computational effort. Therefore it is recommended to adjust the filter of aliased energy. The focus for the development of the aliased energy filter should be on the implementation of a mechanism that is able to recognize the difference in spectral position of wave energy between the aliasing location and grid point location. This could possibly be implemented by applying a simple formulation for wave refraction.

Next to the optimization of spectral information by filtering, it is highly desirable to investigate the effect of the shift of spectral energy in $k-\omega$-space with respect to its theoretical position. This shift was recently found by Tenthof van Noorden (2015). The cause of part of the shift (1 pixel in k_x and k_y-direction) was discovered: an unequal amount of positive and negative solutions for the FFT in MATLAB. A quick test along the representative flood drifter trajectory shows that this 1-pixel energy shift has a major influence on the results:

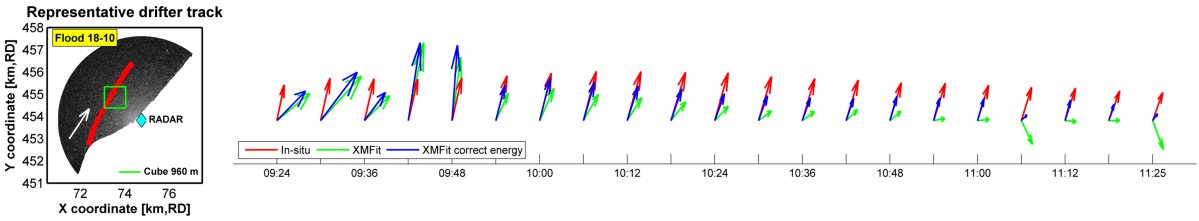

Figure 8.1: Offset in XMFit current direction is almost zero when spectral energy is on the correct location

The increase in accuracy after correcting for the 1-pixel shift in spectral energy is impressive. The offset in current direction is completely resolved and current estimates are almost equal to the in-situ drifter measurements. The results after correction for the 1-pixel energy shift show that it is of paramount importance to analyze the accuracy of radar current measurements for other current time series as well. The combination of an improved aliasing filter and additional testing on the effect of the correction for spectral energy shift may finally lead to radar current estimates that have accuracies close to the level of direct application in coastal engineering projects.

BIBLIOGRAPHY

S. Appleyard, R. Linford, and P. Yarwood. *Marine Electronic Navigation*. Routledge, New York, United States, 2 edition, 1997.

F. Ardhuin, L. Marie, N. Rascle, P. Forget, and A. Roland. Observation and estimation of lagrangian, stokes, and eulerian currents induced by wind and waves at the sea surface. *Journal of Physical Oceanography*, 39: 2820–2838, 2009.

P. Bell and J. Osler. Mapping bathymetry using x-band marine radar data recorded from a moving vessel. *Ocean Dynamics*, 61:2141–2156, 2011.

P. Bell, J. Lawrence, and J. Norris. Determining currents from marine radar data in an extreme current environment at a tidal energy test site, 2012.

J. Borge, G. Rodriguez, K. Hessner, and P. Gonzales. Inversion of marine radar images for surface wave analysis. *Journal of Atmospheric and Oceanic Technology*, 21:1291–1300, 2004.

P. Broche, J. de Maistre, and P. Forget. Mesure par radar decametrique coherent des courants superficiels engendres par le vent. *Oceanologica Acta*, 6(1):43–53, 1983.

R. Chapman and H. Graber. Validation of hf radar measurements. *Oceanography*, 10(2):76–79, 1997.

J. Friedman. Development of an x-band radar depth inversion model at the sand motor. Master's thesis, TU Delft, the Netherlands, 2014.

R. Gangeskar. Ocean current estimated from x-band radar sea surface images. *IEEE Transactions on Geo-Science and Remote Sensing*, 40(4):783–792, 2002.

H. Graber, B. Haus, R. Chapman, and L. Shay. Hf radar comparisons with moored estimates of current speed and direction: expected differences and implications. *Journal of Geophysical Research*, 102(C8):18749–18766, 1997.

K. Hessner and P. Bell. High resolution current bathymetry determined by nautical x-band radar in shallow waters. *OCEANS 2009-EUROPE*, pages 1–5, 2009.

K. Hessner and J. Nieto Borge. High resolution current and bathymetry determined by nautical x-band radar. *International Geoscience and Remote Sensing Symposium*, 2012.

L. H. Holthuijsen. *Waves in Oceanic and Coastal Waters*. Cambridge University Press, New York, United States of America, 2 edition, 2009.

K. Laws. *Measurements of Near Surface Ocean Currents using HF Radar*. PhD thesis, University of California, Santa Cruz, June 2001.

B. Lipa, C. Whelan, B. Rector, and B. Nyden. Hf radar bistatic measurement of surface current velocities: Drifter comparisons and radar consistency checks. *Remote Sensing*, 1:1190–1211, 2009.

L. Liu, Y. Dai, and J. Gao. Simulation analysis and model of current retrieval based on marine radar sea clutter images. *Mathematical Problems in Engineering*, pages 1–14, 2014.

B. Lund, H. Graber, J. Campana, and E. Terrill. Near-surface current shear measured by marine x-band radar, 2012.

B. Lund, J. Campana, H. Graber, and E. Terill. Marine x-band radar based near-surface current profiling. (to appear), 2015.

J.-Y. Maa and H. Ha. X-band radar wave observation system, 2005. Project report: Marine X-band radar for Wave Observations.

C. Ohlmann, P. White, L. Washburn, E. Terrill, B. Emery, and M. Otero. Inerpretation of coastal hf radar-derived surface currents with high resolution drifter data. *Journal of Atmospheric and Oceanic Technology*, 24:666–680, 2007.

J. Paduan and H. Graber. Introduction to high-frequency radar: Reality and myth. *Oceanography*, 10:36–39, 1997.

C. Piotrowski and J. Dugan. Accuracy of bathymetry and current retrievals from airborne optical time-series imaging of shoaling waves. *IEEE Transactions on GeoScience and Remote Sensing*, 40(12):1–11, 2002.

A. Robinson and L. Wyatt. A two year comparison between hf radar and adcp current measurements in liverpool bay. *Journal of Operational Oceanography*, 4(1):33–45, 2011.

J. Rohrs, A. Sperrevik, C. K.H., G. Brostrom, and O. Breivik. Comparison of hf radar measurements with eularian and lagrangian surface currents. *Ocean Dynamics*, 65:679–690, 2015.

J. Seemann, F. Ziemer, and C. Senet. A method for computing calibrated ocean wave spectra from measurements with a nautical x-band radar. *Oceans 97. MTS/IEEE Conference Proceedings*, 2:1148–1154, 1997.

C. Senet, J. Seemann, and F. Ziemer. An iterative technique to determine the near surface current velocity from time series of sea surface images, 1997.

C. Senet, J. Seemann, and F. Ziemer. The near-surface current velocity determined from image sequences of the sea surface. *IEEE Transactions on GeoScience and Remote Sensing*, 39(3):492–505, 2001.

F. Serafino, C. Lugni, J. Nieto Borge, and F. Soldovieri. A simple strategy to mitigate the aliasing effect in x-band marine radar data: Numerical results for a 2d case. *Sensors(Basel)*, 11(1):1009–1027, 2011.

R. Stewart and J. Joy. Hf radio measurements of surface currents. *Deep-Sea Research*, 21:1039–1049, 1974.

M. Stive, M. de Schipper, A. Luijendijk, R. Ranasinghe, J. van Thiel de Vries, S. Aarninkhof, C. van Gelder-Maas, S. de Vries, M. Henriquez, and S. Marx. The sand engine: A solution for vulnerable deltas in the 21st century? *Coastal Dynamics*, pages 1537–1546, 2013.

C. Swinkels, H. Peters, and J. van Heesen. Analysis of current patterns in coastal areas using x-band radar images. *Coastal Engineering*, pages 1–10, 2012.

C. Tenthof van Noorden. The accuracy and error sources of radar-derived bathymetry by the xmfit algorithm. Master's thesis, TU Delft, the Netherlands, 2015.

D. Thompson, B. Gotwols, and W. Keller. A comparison of ku-band doppler measurements at 20 incidence with predictions from a time-dependent scattering model. *Journal of Geophysical Research*, 96(C3):4947–4955, 1991.

G. Valenzuala. Theories for the interaction of electromagnetic oceanic waves - a review. *Boundary-layer meteorology*, 13:61–85, 2012.

A. van Gils. Validation of x-band radar derived hydrodynamic phenomena. Master's thesis, TU Delft, the Netherlands, 2014.

K. Ward, R. Tough, and S. Watts. *Sea clutter: Scattering, the K-distribution and Radar Performance*. The institution of Engineering and Technology, London, United Kingdom, 1 edition, 2006.

M. Wengrove, M. Henriquez, M. de Schipper, R. Holman, and M. Stive. Monitoring morphology of the sand engine leeside using argus' cbathy. *Coastal Engineering*, pages 1893–1904, 2013.

I. Young, W. Rosenthal, and F. Ziemer. A three-dimensional analysis of marine radar images for the determination of ocean wave directionality and surface currents. *Journal of Geophysical Research*, 90:1049–1059, 1985.

G. Yuan, R. Jia, Y. Dai, and Y. Li. Low wave number radar image energy influence on determining current. *Advanced Materials Research*, 433-440:6054–6059, 2012.

W. Zeelenberg. Tidal flow separation at the sand motor: an experimental study. Master's thesis, TU Delft, the Netherlands, 2015.